FGF signaling regulates development through combinatorial transduction pathways and by modulating cellular adhesion

Ayan Ray, Pierre Mazot[1], J. Richard Brewer[2], Catarina Catela[3], and Philippe Soriano*

Department of Cell, Developmental, and Regenerative Biology
Icahn School of Medicine at Mount Sinai
New York, NY 10029

*Corresponding author: philippe.soriano@mssm.edu

Present address: [1]INSERM Transfert, Paris, France
[2]Department of Immunobiology, Yale University, New Haven, CT 06520
[3]Department of Neurobiology, University of Chicago, Chicago, IL 60637

Keywords: Midface; mandible; neural crest; cell signaling

Summary

FGFs are key developmental regulators which typically direct cell proliferation, survival, and migration following the engagement of tyrosine kinase receptors. We find that coordinate loss of *Fgfr1* and *Fgfr2* in cranial neural crest cells results in facial clefting and mandibular defects with high levels of apoptosis, and that suppressing cell death alleviates the mutant phenotype. To identify critical downstream signaling pathways that regulate these processes, we generated allelic series of knock-in point mutations in each gene that disrupt binding of signaling effectors to the receptors, alone or in combination, as well as a kinase dead allele of *Fgfr2* which broadly phenocopies the null mutant. While signaling mutations in either receptor, even when combined, failed to recapitulate the null mutant phenotypes, they revealed discrete roles for various pathways in regulating specific aspects of craniofacial development. We furthermore found that these signaling mutations together abrogate multiple established FGF-induced signal transduction pathways, while other FGF functions such as cell-matrix and cell-cell adhesion remain unaffected. Our studies establish combinatorial roles of both *Fgfr1* and *Fgfr2* in development and identify novel kinase-dependent cell adhesion properties for FGF receptors, beyond their well-established roles in intracellular signaling.

Introduction

The development of the face involves the coordination of multiple morphogenetic processes including the formation of the frontonasal, maxillary and mandibular processes, and their convergence at the midline. The pharyngeal arches (PA) appear on each side of the future head and neck and grow ventrally, and are composed largely of mesenchyme derived from cranial Neural Crest Cells (cNCCs), which surrounds a mesodermal core and is covered by surface ectoderm. The primitive mouth, or stomodeum, is flanked rostrally by the frontonasal prominence (FNP), laterally by the maxillary (Mx) processes, and caudally by the mandibular (Man) processes. Subsequently, the FNP widens, grows and bulges around the nasal placodes. By E10.5, rapid growth of the maxillary mesenchyme pushes the nasal pits medially. Closure of the midface initiates with the convergence of the medial (MNP) and lateral (LNP) nasal processes. Rapid growth of the Mx and LNP then pushes the MNP to converge.

NCCs differentiate into multiple cell types, including, cartilage, bone, neuronal, glial and smooth muscle cells (Bronner and LeDouarin, 2012). In the head, cNCCs collectively migrate through various mechanisms (Szabo and Mayor, 2018) and give rise to the majority of the bone and cartilage in the head and the face (Chai et.al. 2000; Couly et al., 1993). Paracrine signaling between the facial ectoderm and the underlying cNCC- derived mesenchyme is particularly

important for craniofacial morphogenesis, implicating a number of signaling pathways. FGF8 has been shown to play an important role in regulating mandibular development (Shigetani et al., 2000; Trumpp et al., 1999) and midface integration (Griffin et al., 2013). In mammals, 22 FGFs have been identified by sequence homology, with 18 acting as secreted ligands for 4 FGF receptors (FGFR1-4) (Brewer et al., 2016; Ornitz and Itoh, 2015). All *Fgfr* genes have been disrupted in mice demonstrating both specific and redundant functions *in vivo*. *Fgfr1* null mutants fail to gastrulate and exhibit a defect in epithelial to mesenchyme transition required for mesoderm formation (Ciruna and Rossant, 2001; Ciruna et al., 1997; Deng et al., 1994; Yamaguchi et al., 1994). Recent studies of *Fgfr1* and *Fgfr2* mutants however have documented an earlier genetic background-dependent role for *Fgfr1* in primitive endoderm and trophectoderm development (Brewer et al., 2015; Hoch and Soriano, 2006; Kurowski et al., 2019), and a combined role for *Fgfr1* and *Fgfr2* in both of these lineages (Kang et al., 2017; Kurowski et al., 2019; Molotkov et al., 2017). Null mutants for *Fgfr2* exhibit embryonic lethality at E10.5 associated with placenta deficiency and exhibit multiple additional defects including the absence of limb bud development (Molotkov et al., 2017; Xu et al., 1998b; Yu et al., 2003). Additional evidence further supports a role for *Fgfr1* and *Fgfr2* in craniofacial development, as conditional mutagenesis of *Fgfr1* in cNCCs or of *Fgfr2* in the epithelium leads to facial or palatal clefting (Brewer et al., 2015; Hosokawa et al., 2009; Rice et al., 2004; Wang et al., 2013) while deletion of both receptors in cNCCs prevents midface closure (Park et al., 2008). However, the signaling mechanisms by which FGFs regulate craniofacial development have not been elucidated.

Upon ligand binding, FGFRs dimerize which leads to transactivation of the kinase domain, subsequent phosphorylation of intracellular tyrosines, and binding of signaling effectors that in turn orchestrate activation of downstream signaling pathways (Brewer et al., 2016; Lemmon and Schlessinger, 2010). Different thresholds in dimer strength and stability also may come into play, as well as signaling dynamics engaged by each downstream signaling pathway (Li and Elowitz, 2019; Vasudevan et al., 2015; Zinkle and Mohammadi, 2018). The signaling pathways that operate downstream of FGFR1 have been particularly well studied (reviewed in (Brewer et al., 2016)). One of the most important signaling pathways induced by FGF signaling is ERK1/2, which is mainly thought to be activated by constitutive binding of adaptor proteins FRS2 and FRS3 to the juxtamembrane portion of FGFR1, leading to subsequent recruitment of GRB2 and SHP2 and activation of the MAPK pathway. However, GRB2 can also associate with the adaptor protein GAB1, which conversely promotes activation of PI3K/AKT (Kouhara et al., 1997; Ong et al., 2000; Ong et al., 2001; Xu et al., 1998a). In addition, CRKII or CRK-L binding to FGFR1 at Y463 also drives activation of ERK1/2, as well as JNK (Larsson et al., 1999; Moon et al., 2006; Seo et al.,

2009). PLCγ binds FGFR1 at Y766, and regulates both receptor intracellular trafficking and PKC activation (Mohammadi et al., 1992; Mohammadi et al., 1991; Sorokin et al., 1994). Finally, GRB14 binding requires phosphorylation of FGFR1 Y766 and Y776 and negatively regulates PLCγ recruitment (Browaeys-Poly et al., 2010; Reilly et al., 2000). Signaling interactions with FGFR2 have been less well studied, but FRS2 and PLCγ have been confirmed to bind to FGFR2 at the juxtamembrane domain and Y769, respectively (Ceridono et al., 2005; Eswarakumar et al., 2006). CRK-L, but not CRK, binds to FGFR2 presumably at Y466 (Moon et al., 2006; Seo et al., 2009). Together, these studies indicate that FGF signaling converges on ERK1/2, as well as other downstream pathways. FGF signaling through these effectors regulates canonical RTK outputs, such as such as cell proliferation, survival, and migration (Brewer et al., 2016; Lemmon and Schlessinger, 2010). Beyond these canonical RTK signaling outputs however, FGF signaling is also known to regulate other cellular processes, through less well established mechanisms, such as cell-matrix (Meyer et al., 2012) or cell-cell adhesion (Kurowski et al., 2019; Rasouli et al., 2018; Sun and Stathopoulos, 2018). It remains unclear if all activities engaged by the FGF receptors are dependent on activation by FGFs, on signaling through the kinase domain, or if the receptors can engage cell adhesion receptors through interactions of their extracellular domains or by acting as scaffolds in specific cell surface compartments.

Although characterization of effector binding to RTKs provides critical insights on their signaling specificity, assessing their relative significance requires *in vivo* validation. Numerous lines of evidence point to ERK1/2 downstream of FRS proteins as a major FGF signaling output (Corson et al., 2003; Eswarakumar et al., 2006; Gotoh et al., 2004; Hadari et al., 2001; Lanner and Rossant, 2010; Vasudevan et al., 2015). An allele of *Fgfr1* deficient for FRS2 and FRS3 binding by deletion of the juxtamembrane part of the receptor did not recapitulate the *Fgfr1* null phenotype, however, suggesting that multiple developmental contexts do not require FRS dependent FGF signaling (Hoch and Soriano, 2006). PLCγ has been proposed to play a role as a negative regulator of FGF signaling (Partanen et al., 1998). To further study FGFR1 signaling pathways, we generated an allelic series of knock-in point mutation at the *Fgfr1* locus that disrupt binding of multiple signaling effectors, alone or in combination (Brewer et al., 2015). Analysis of these signaling mutant alleles suggested that FGFR1 requires combinatorial signaling during development. Strikingly, the most severe *Fgfr1* signaling mutants did not recapitulate the *Fgfr1* null phenotype, despite almost eliminating ERK1/2 signaling, suggesting that additional signaling pathways remain to be identified. *In vivo* functions of FGFR2 signaling effectors are still largely unknown, however evidence to date indicates that signaling through FRS2 is not required by FGFR2 during development (Eswarakumar et al., 2006; Sims-Lucas et al., 2009).

To understand how FGF signaling regulates craniofacial development, we analyzed *Fgfr1; Fgfr2* double conditional cNCC mutants. We found that loss of FGF signaling dramatically affects midface as well as mandibular development. To identify the downstream signaling pathways that are involved, we generated an allelic series of knock-in point mutations at the *Fgfr2* locus that disrupt binding of FRS2, CRK-L, PLCγ and GRB14, alone or in combination. To our surprise, analysis of the *Fgfr2* allelic series demonstrated that none of these signaling effectors are critically required downstream of FGFR2 during development. We furthermore intercrossed *Fgfr1* and *Fgfr2* mutants carrying the same signaling mutations to each other or to null mutants. These studies revealed that while various signaling pathways impair discrete aspects of craniofacial development, in the most severe combination they still did not recapitulate the double null phenotype. Analysis of intracellular pathways demonstrated that classical FGF-induced signal transduction pathways were abrogated in our mutants, while non-canonical cell-matrix and cell-cell adhesion functions of the FGF pathway remained unaffected even in the most severe signaling mutants and depended on kinase activation. Our results thus ultimately point to an unknown kinase-dependent output of FGFRs that regulates aspects of the cytoskeleton and cell adhesion and is important in embryonic development. Our studies further establish combinatorial roles of both *Fgfr1* and *Fgfr2* in craniofacial development and provide support for the notion that RTKs have adopted multiple functions in cells, beyond their well-established roles in intracellular cell signaling.

Results

Disruption of *Fgfr1* and *Fgfr2* in NCCs leads to defective craniofacial morphogenesis

We had previously generated $Fgfr1^{GFP}$ and $Fgfr2^{mCherry}$ reporter mice (Molotkov et al., 2017) that allowed us to identify spatial domains and overlap of *Fgfr1* and *Fgfr2* expression in E10.5 embryonic heads. *Fgfr1* expression was observed primarily in the mesenchyme (Figure 1A, yellow arrow). In contrast, strong *Fgfr2* expression was seen in the epithelia except for a small domain surrounding the nasal pit (Figure 1A, yellow asterisk). Weaker widespread *Fgfr2* expression was also observed within the mesenchyme (Figure 1A, red arrow), indicating that both *Fgfr1* and *Fgfr2* are co-expressed in multiple regions (Figure 1A and Supplementary Figure S1A).

To interrogate FGFR1/2 functions, and to establish a baseline to study cell signaling mutations, we initially investigated how loss of both receptors in NCCs influence craniofacial development. To this end, conditional null alleles of *Fgfr1* and *Fgfr2* were combined with the *Wnt1Cre* driver that is active in NCCs as they delaminate from the neural tube (Danielian et al., 1998), and *Wnt1Cre* conditional mutants are referred to as *cKO.* Similar results were obtained

with the *Wnt1Cre2* driver (Lewis et al., 2013). Throughout this work, all *Fgfr1*, *Fgfr2* and *Cre* driver alleles were analyzed on a 129S4 co-isogenic background, to avoid phenotypic variations that might be attributable to second-site modifiers. No overt defects were observed in *Fgfr1*$^{cKO/+}$; *Fgfr2*$^{cKO/+}$ double heterozygous or in *Fgfr2*$^{cKO/cKO}$ conditional mutants (Figure 1B and Supplementary Figure S1B). In contrast, conditional ablation of *Fgfr1* (*Fgfr1*$^{cKO/cKO}$) led to a fully penetrant facial cleft (Figure 1B) indicating a critical role for *Fgfr1* rather than *Fgfr2* in cNCC development.

Although *Fgfr2*$^{cKO/cKO}$ mutants did not display any overt phenotype, loss of *Fgfr2* significantly enhanced the phenotype of *Fgfr1*$^{cKO/cKO}$ conditional mutants (Figure 1B and Supplementary Figure S1B). Both *Fgfr1*$^{cKO/cKO}$ and *Fgfr1*$^{cKO/cKO}$; *Fgfr2*$^{cKO/+}$ embryos exhibited defects in mandible development where proximal structures including angular and coronoid processes were hypomorphic (Supplementary Figure S1C). Conditional deletion of both *Fgfr1* and *Fgfr2* (*Fgfr1*$^{cKO/cKO}$; *Fgfr2*$^{cKO/cKO}$) led to severe agenesis of most NCC derived craniofacial structures including the frontal and nasal bones, nasal cartilage, maxilla, and mandible (Figure 1B and Supplementary Figure 1C). All *Fgfr1*$^{cKO/cKO}$; *Fgfr2*$^{cKO/cKO}$ conditional mutants died perinatally. However, mesoderm-derived structures such as the parietal, interparietal and supraoccipital bones remained unaffected (Supplementary Figure S1B). Overall, we observed reduced or no ossification of all neural crest derived craniofacial skeletal structures in the double mutants at E18.5.

Next, we analyzed E9.5 and E10.5 *Fgfr1*$^{cKO/cKO}$; *Fgfr2*$^{cKO/cKO}$; *ROSA26*$^{mT/mG}$ double mutants, where NCCs were GFP labeled, to investigate when noticeable defects emerge. Although GFP^{+} NCCs were distributed throughout their migration streams at E9.5, the PA1 and PA2 arches appeared hypoplastic in double mutants (Figure 1C, yellow arrows). By E10.5, *Fgfr1*$^{cKO/cKO}$; *Fgfr2*$^{cKO/cKO}$; *ROSA26*$^{mT/mG}$ double mutants were morphologically identifiable with wider midline separation and hypoplastic MNP, LNP, maxillary and mandibular prominences (Figure 1C, yellow asterisk). A similar wide midline separation was also observed in *Fgfr1*$^{cKO/cKO}$; *Fgfr2*$^{cKO/+}$; *ROSA26*$^{mT/mG}$ mutants (Figure 1C, yellow asterisk). We analyzed molecular changes during morphogenesis at E10.5 using whole mount *in situ* hybridization. We examined expression of facial prominence markers, *Alx3, Msx1,* and *Six3*, along with midline morphogenesis markers, *Shh* and *Nkx2.1*. In *Fgfr1*$^{cKO/cKO}$; *Fgfr2*$^{cKO/cKO}$ mutants, we observed the absence of *Alx3* and *Six3* expression in the MNP (Figure 1D). *Msx1* expression was significantly reduced (Figure 1F), suggesting a reduction in number of NCC cells in the double mutants. Along the midline, while *Shh* expression remained unaffected, *Nkx2.1* expression was lost indicating a midline morphogenesis defect (Figure 1D). We also examined the expression of *Fgf8* which is expressed

in the ectoderm. Interestingly, *Fgf8* was expressed in the *Fgfr1*$^{cKO/cKO}$*; Fgfr2*$^{cKO/cKO}$ mutants and was comparable to the *Fgfr1*$^{cKO/+}$*; Fgfr2*$^{cKO/+}$ controls (Figure 1D). These results indicate that the morphological defects observed upon loss of FGF receptors are not due to patterning defects, as the domains of *Fgf8* and *Shh* expression at E10.5 remain unaffected, and instead suggest changes in the number of NCCs.

By E12.5, acute defects in midline integration were apparent, with a fully penetrant facial cleft (Figure 1E, yellow asterisk) and a severe mandibular defect (Figure 1E, yellow arrow). By E15.5, histological examination showed defective organogenesis in multiple organs, including the palate, tongue, and skeleton (Supplementary Figure S1D). Conditional double mutants also showed severe defects in trigeminal ganglion development. Whole mount staining with a neurofilament marker revealed that in *Fgfr1*$^{cKO/cKO}$*; Fgfr2*$^{cKO/cKO}$ mutants, the mandibular branch of trigeminal nerve failed to reach the anterior mandibular arch, while the maxillary branch showed fewer neural fibers compared to the *Fgfr1*$^{cKO/+}$*; Fgfr2*$^{cKO/+}$ control (Figure 1F). Interestingly, *Fgfr1*$^{cKO/cKO}$*; Fgfr2*$^{cKO/+}$ mutants, which exhibited a mild mandibular phenotype, did not show a trigeminal nerve defect (Figure 1F).

The anterior part of the craniofacial skeleton, including the maxilla and mandible, nasal cartilage, Meckel's cartilage, frontal bone and anterior cranial base (ethmoid and sphenoid bones), are derived from NCCs. Analysis of alcian blue/ alizarin red stained skeletal preparations at E14.5 revealed that in contrast to the *Fgfr1*$^{cKO/+}$*; Fgfr2*$^{cKO/+}$ controls, *Fgfr1*$^{cKO/cKO}$*; Fgfr2*$^{cKO/cKO}$ mutants developed an anteriorly truncated skull due to loss of nasal cartilage (Figure 1G). Meckel's cartilage, a transient cartilage template that directs the formation of bony mandible, was also severely affected and was completely missing in *Fgfr1*$^{cKO/cKO}$*; Fgfr2*$^{cKO/cKO}$ mutants (Figure 1G). The size of Meckel's cartilage was significantly reduced in *Fgfr1*$^{cKO/cKO}$*; Fgfr2*$^{cKO/+}$ conditional mutants (Figure 1G, yellow arrow). We also observed absence of alizarin red staining in *Fgfr1*$^{cKO/cKO}$*; Fgfr2*$^{cKO/cKO}$ mutant heads at this stage suggesting these defects are accompanied by reduced ossification. Defects in ossification were also observed in *Fgfr1*$^{cKO/cKO}$*; Fgfr2*$^{cKO/+}$ mutants which displayed an intermediate phenotype, specifically reduced alizarin red staining in the mandible and a complete absence of ossification in the maxilla (Figure 1G, red arrow). Taken together, these results suggest that FGF signaling plays an important role in skeletal differentiation of cNCCs.

Skeletal differentiation is a multi-step process starting with formation of cartilage progenitors which undergo maturation and eventually terminally differentiate into bone. To investigate the role of FGF receptors during skeletal differentiation of NCCs in the head we analyzed the expression of chondrogenic (*Col2a1*) and osteogenic markers (*Col10a1* and

RUNX2), first at an early stage at E14.5 (Supplementary Figure 1E) when cartilage progenitors are formed, and then at E17.5 (Supplementary Figure 1E) during which terminal differentiation is largely complete. Our analysis revealed that at E14.5 in *Fgfr1*$^{cKO/+}$*; Fgfr2*$^{cKO/+}$ control, anterior cranial base primordia express *Col2a1*, in a broader domain than *Fgfr1*$^{cKO/cKO}$*; Fgfr2*$^{cKO/cKO}$ mutants (Supplementary Figure 1E). This suggests that the skeletal differentiation program is initiated and cartilage progenitors are formed in *Fgfr1*$^{cKO/cKO}$*; Fgfr2*$^{cKO/cKO}$ mutants, but is probably delayed or attenuated. By E17.5, we observed similar levels of *Col2a1* expression in both controls and *Fgfr1*$^{cKO/cKO}$*; Fgfr2*$^{cKO/cKO}$ double mutants. However, expression of *Col10a1*, a terminal differentiation marker, was undetectable at this stage in the *Fgfr1*$^{cKO/cKO}$*; Fgfr2*$^{cKO/cKO}$ mutants while it was still expressed in broad domains in *Fgfr1*$^{cKO/+}$*; Fgfr2*$^{cKO/+}$ controls (Supplementary Figure 1E), suggesting that the terminal differentiation process during endochondral ossification is blocked. We also looked at expression of *Runx2*, a mature cartilage and bone differentiation marker. In our analysis, we found that *Runx2* was expressed at similar levels in both controls and *Fgfr1*$^{cKO/cKO}$*; Fgfr2*$^{cKO/cKO}$ mutants at E17.5 (Supplementary Figure 1E). The extent of ossification was assessed by micro-CT at E18.5, which showed reduced ossification of NCC derived structures in the anterior skull as well as the mandible (Figure 1H). Overall, we conclude that FGF receptors play an important role during terminal differentiation of skeletal structures that primarily affects the anterior NCC-derived structures, including the anterior chondrocranium, the Meckel's cartilage, the nasal cartilage and bone. The observation that FGF signaling is important for skeletal differentiation is consistent with previous studies of differentiation of long bones (Karuppaiah et al., 2016).

Increased apoptosis is observed in mutant facial primordia

We observed reduced fluorescence from GFP^{+} cells in the mid-face in *Fgfr1*$^{cKO/cKO}$*; Fgfr2*$^{cKO/cKO}$; *ROSA26*$^{mT/mG}$ mutants at E9.5, which became more noticeable by E10.5 (Figure 2A), suggesting reduced numbers of NCCs in the midface. To further investigate this observation, we determined the percentage of GFP^{+} cNCCs at E10.5 using flow sorting of single cell suspensions from the five facial prominences for all genotypes. Compared to controls, *Fgfr1*$^{cKO/cKO}$*; Fgfr2*$^{cKO/cKO}$; *ROSA26*$^{mT/mG}$ double mutants showed a 50% reduction in the number of GFP^{+} cells (Figure 2B). We did not observe a significant reduction in either *Fgfr1*$^{cKO/+}$*; Fgfr2*$^{cKO/cKO}$; *ROSA26*$^{mT/mG}$ or *Fgfr1*$^{cKO/cKO}$*; Fgfr2*$^{cKO/+}$; *ROSA26*$^{mT/mG}$ mutants, suggesting that the skeletal defects observed at E14.5 or E17.5 result from both reduction in NCC numbers as well as *Fgfr1*; *Fgfr2* dependent differentiation of NCCs into skeletal lineages. A reduction in numbers of NC lineage cells in the midface might occur due to reduced proliferation, increased cell death, or both. Therefore, we first

investigated the extent of cell proliferation by EdU incorporation at E10.5 in mutant facial primordia (Figure 2C-D). Compared to controls, we observed a similar extent of EdU incorporation in the *Fgfr1*$^{cKO/cKO}$*; Fgfr2*$^{cKO/cKO}$; *ROSA26*$^{mT/mG}$ mutant NCC derived craniofacial mesenchyme (Figure 2C-D), suggesting that the extent of cell proliferation between control and *Fgfr1*$^{cKO/cKO}$*; Fgfr2*$^{cKO/cKO}$; *ROSA26*$^{mT/mG}$ mutants remains unaffected. Next, we investigated cell death in *Fgfr1*$^{cKO/cKO}$*; Fgfr2*$^{cKO/cKO}$; *ROSA26*$^{mT/mG}$ conditional homozygous double mutants. TUNEL staining revealed a striking increase in apoptosis in the craniofacial mesenchyme at E10.5 in *Fgfr1*$^{cKO/cKO}$*; Fgfr2*$^{cKO/cKO}$ mutants, most notably in the LNP relative to the MNP (Figure 2E-F). These observations suggested that cell-survival/ regulation of apoptosis downstream of FGF receptor signaling plays a crucial role during craniofacial development.

Although we found a clear increase in cell death in double mutants, we asked to what extent this observation could explain the overall morphological defects. The BH3-only protein BIM can bind to and repress the function of several pro-survival BCL-2 family members and therefore plays a critical role in initiating apoptotic pathway in multiple cell types (Chipuk and Green, 2008; Czabotar et al., 2014; Youle and Strasser, 2008). A recent report showed that mutations in the pro-survival genes *Mcl-1* and *Bcl-x* leads to severe holoprosencephaly, which can be corrected by further loss of *Bim,* indicating that cell survival and cell death are finely balanced during development (Grabow et al., 2018). To investigate the role of cell survival and determine if a reduction of *Bim* levels can rescue craniofacial defects in *Fgfr1*$^{cKO/cKO}$*; Fgfr2*$^{cKO/cKO}$ mutants, we first compared *Fgfr1*$^{cKO/cKO}$*; Fgfr2*$^{cKO/+}$*; Bim*$^{+/-}$ mutants with control *Fgfr1*$^{cKO/cKO}$*; Fgfr2*$^{cKO/+}$ embryos at E17.5. *Fgfr1*$^{cKO/cKO}$*; Fgfr2*$^{cKO/+}$*; Bim*$^{+/-}$ mutants were obtained at expected ratios and exhibited a 55% reduction in midline separation in *Fgfr1*$^{cKO/cKO}$*; Fgfr2*$^{cKO/+}$*; Bim*$^{+/-}$ mutants compared to *Fgfr1*$^{cKO/cKO}$*; Fgfr2*$^{cKO/+}$ controls (Figure 2G), thus showing a partial rescue of craniofacial defects. We also observed a partial rescue of medial skeletal structures in *Fgfr1*$^{cKO/cKO}$*; Fgfr2*$^{cKO/+}$*; Bim*$^{+/-}$ embryos, where defects in anterior nasal cartilage and palatine process of the premaxilla were partially alleviated, as well as other medial structures including the primary and secondary palate, pterygoid process and basisphenoid bone. The reduction in *Bim* levels significantly rescued defects observed in *Fgfr1*$^{cKO/cKO}$*; Fgfr2*$^{cKO/cKO}$*; Bim*$^{+/+}$ embryos, particularly at the level of the nasal mesenchyme and the midface (Figure 2H). Other morphometric parameters such as skull length and intercanthal distances also showed a partial rescue.

We next examined if reduced *Bim* levels can alleviate cell survival defect at E10.5. We used the TUNEL assay to assess apoptosis in embryonic heads at E10.5 on sections of *Fgfr1*$^{cKO/cKO}$*; Fgfr2*$^{cKO/cKO}$*; Bim*$^{+/-}$ and *Fgfr1*$^{cKO/cKO}$*; Fgfr2*$^{cKO/+}$*; Bim*$^{+/-}$ embryos. Compared to wild type levels of BIM, both *Fgfr1*$^{cKO/cKO}$*; Fgfr2*$^{cKO/cKO}$*; Bim*$^{+/-}$ and *Fgfr1*$^{cKO/cKO}$*; Fgfr2*$^{cKO/+}$*; Bim*$^{+/-}$ embryos

showed reduced cell death (Supplementary Figure S1F). We observed an overall 25% reduction of cell death in *Fgfr1*$^{cKO/cKO}$*; Fgfr2*$^{cKO/+}$*; Bim*$^{+/-}$ embryos, as opposed to a 17% reduction in *Fgfr1*$^{cKO/cKO}$*; Fgfr2*$^{cKO/cKO}$*; Bim*$^{+/-}$ embryos. Interestingly, *Bim* heterozygosity resulted in a greater morphological rescue in *Fgfr1*$^{cKO/cKO}$*; Fgfr2*$^{cKO/cKO}$*; Bim*$^{+/-}$ mutants than in *Fgfr1*$^{cKO/cKO}$*; Fgfr2*$^{cKO/+}$*; Bim*$^{+/-}$ mutants, which already had less cell death. Taken together, these results underscore the importance of cell death in the etiology of the *Fgfr1*$^{cKO/cKO}$*; Fgfr2*$^{cKO/cKO}$ conditional double mutant phenotype.

Generation of an allelic series of *Fgfr2* signaling mutations

To interrogate FGFR2 signaling mechanisms *in vivo*, we generated an allelic series of knock-in point mutations at the *Fgfr2* locus by gene targeting in ES cells (Figures 3). We introduced mutations in critical residues, preventing binding of signaling effectors to FGFR2 (Figure 3A-C) and verified targeting by PCR and Southern blots (Figure 3D). The *Fgfr2*^{F} mutation (amino acid substitutions L424A and R426A), *Fgfr2*^{C} mutation (amino acid substitution Y463F), and *Fgfr2*^{PG} (amino acid substitutions Y769F and Y779F) mutation were designed to disrupt binding of FRS2, CRK-L and PLCγ/GRB14, respectively. We also generated compound *Fgfr2*^{CPG} and *Fgfr2*^{FCPG} signaling mutants by combining multiple signaling mutations. We provided biochemical validation of effector binding disruption for all signaling mutations. To validate the disruption of effector binding, 3T3 cells were transfected with triple Flag-tagged cDNAs of FGFR2c isoforms for each signaling mutants. We confirmed disruption of FRS2, CRK-L and PLCγ binding in *Fgfr2*^{PG}, *Fgfr2*^{CPG}, *Fgfr2*^{F} and *Fgfr2*^{FCPG} mutations, respectively, via co-immunoprecipitation and western blot analysis (Figure 3B).

Fgfr2 signaling mutant alleles were evaluated for their ability to partially or completely recapitulate the *Fgfr2*$^{-/-}$ E10.5 phenotype associated with placenta and limb deficiencies (Molotkov et al., 2017; Xu et al., 1998b; Yu et al., 2003). Surprisingly, all signaling allele mutants were at least partially viable and fertile as homozygotes (Table 1). We observed a decreased growth rate for *Fgfr2*$^{F/F}$, *Fgfr2*$^{PG/PG}$, and *Fgfr2*$^{FCPG/FCPG}$ mutant mice compared to controls (Supplementary Figure S2A). Interestingly, the growth retardation observed for *Fgfr2*$^{PG/PG}$ mutants was rescued by the concomitant disruption of CRK-L binding site in *Fgfr2*$^{CPG/CPG}$ mutants, suggesting opposite roles for these effectors in mediating FGFR2 signaling. Skeletal preparations at birth revealed a kinked tail phenotype for *Fgfr2*$^{PG/PG}$ (7/9) and *Fgfr2*$^{CPG/CPG}$ (6/12) neonates, the most extreme cases resulting in a curly tail phenotype (Supplementary Figure S2B).

To further identify *in vivo* phenotypes associated with our signaling mutations, we crossed *Fgfr2* signaling mutant mice with the null allele. *Fgfr2*$^{C/-}$, *Fgfr2*$^{PG/-}$ and *Fgfr2*$^{CPG/-}$ mice were viable,

with growth retardation apparent in *Fgfr2*$^{PG/-}$ mutant mice (not shown). In contrast, hemizygous *Fgfr2*$^{F/-}$ and *Fgfr2*$^{FCPG/-}$ mutant mice were recovered in expected Mendelian ratios at E18.5, but died at birth (Table 2). None of the *Fgfr2*$^{F/-}$ and *Fgfr2*$^{FCPG/-}$ neonates were able to suckle, as evidenced by the absence of an abdominal milk spot. This may be a consequence of cranial nerve defects, since *Fgfr2*$^{F/-}$ and *Fgfr2*$^{FCPG/-}$ E10.5 mutant embryos exhibited decreased trigeminal nerve projections into facial prominences compared to control littermate (Supplementary Figure S2C).

Both *Fgfr2*$^{F/F}$ and *Fgfr2*$^{FCPG/FCPG}$ mice develop periocular lesions in the eye as early as postnatal day P15 that worsened over time. Similar phenotypes have been associated with defects in lacrimal glands, which provide protection to the non-keratinized epithelial surface of the eye (Inaba et al., 2018). Upon further investigation, we indeed observed a defect in lacrimal gland development in both *Fgfr2*$^{F/F}$ and *Fgfr2*$^{FCPG/FCPG}$ mice (Supplementary Figure S2D). In mice, lacrimal gland development starts at E13.5 by an epithelial invagination into the surrounding mesenchyme, and progresses by branching morphogenesis to become a fully functional organ by P7. FGF10-FGFR2 signaling plays a critical role during this process where it regulates proliferation in epithelial cells (Garg et al., 2017; Steinberg et al., 2005). Both *Fgfr2*$^{F/F}$ and *Fgfr2*$^{FCPG/FCPG}$ mutants showed loose clusters of acinar cells, which populate the distal end of the ducts, and occupied a much smaller area at P7. A significant reduction in the size of the lacrimal gland was also brought about by reduced number of branches and smaller lengths of the tubes in the *Fgfr2*$^{F/F}$ and *Fgfr2*$^{FCPG/FCPG}$ signaling mutants (Supplementary Figure S2E and S2F).

The observation that all *Fgfr2* signaling mutants were viable and the fact that the *Fgfr2*$^{FCPG/FCPG}$ mutants do not recapitulate the *Fgfr2*$^{-/-}$ phenotype raised the possibility that a critical downstream adaptor might still interact with the FGFR2^{FCPG} receptor. We data-mined a recent proteomic screen identifying FGFR2b dependent phosphorylation events (Francavilla et al., 2013) and identified IRS2 (insulin receptor substrate) as a possible new putative FGFR2 candidate binding partner. IRS2 belongs to the same superfamily of adaptor protein as FRS2 and shares a similar protein architecture, with membrane targeting and PTB (phosphotyrosine binding) domains, as well as a C-terminal tail containing multiple tyrosine phosphorylation sites (Supplementary Figure S2G). We found that IRS2 binds weakly to both WT and FGFR2^{FCPG} receptors in primary MEFs, independent of FGF stimulation (Supplementary Figure S2G and S2H). However, we failed to observe a genetic interaction between *Irs2*$^{-/-}$ and *Fgfr2*$^{FCPG/FCPG}$ mutant mice at E10.5, E13.5 or at birth (data not shown), indicating that IRS2 is a not a critical missing effector of FGFR2 signaling *in vivo*.

Coordinate roles of signaling pathways in development

Our results indicate that signaling mutations in *Fgfr2* do not lead to overt craniofacial defects. Likewise, a previous study focusing on *Fgfr1* harboring a similar allelic series found that *Fgfr1*$^{F/cKO}$ and *Fgfr1*$^{FCPG/cKO}$ mutants showed only a low incidence of cleft palate (Brewer et al., 2015). Because *Fgfr1* and *Fgfr2* have a significant degree of co-expression in NCC-derived mesenchymal cells (Figure 1A), we reasoned that discrete functions of signaling pathways that operate downstream of one receptor could be masked by the presence of the other, wild-type receptor. To test this hypothesis, we examined compound conditional hemizygous *Fgfr1*^{F}, *Fgfr1*^{FCPG} and *Fgfr2*^{F} mutations over the *Fgfr1*$^{-}$ and *Fgfr2*$^{-}$ null alleles in the context of craniofacial development. We were unable to perform a conditional mutation for the *Fgfr2*^{FCPG} allele due to the serial retention of multiple lox sites during the generation of this allele (Figure 3C).

To characterize discrete phenotypes resulting from signaling mutations in *Fgfr1* (*Fgfr1*^{F} or *Fgfr1*^{FCPG} alleles), we crossed *Fgfr1*$^{F/cKO}$*; Fgfr2*$^{cKO/+}$ or *Fgfr1*$^{FCPG/cKO}$*; Fgfr2*$^{cKO/+}$ males to *Fgfr1*$^{cKO/cKO}$*; Fgfr2*$^{cKO/cKO}$ females. We examined *Fgfr1*$^{F/cKO}$*; Fgfr2*$^{cKO/cKO}$ or *Fgfr1*$^{FCPG/cKO}$*; Fgfr2*$^{cKO/cKO}$ (Figure 4A) embryos at E16.5 for skeletal defects. Compared to *Fgfr1*$^{cKO/+}$*; Fgfr2*$^{cKO/cKO}$ controls, *Fgfr1*$^{F/cKO}$*; Fgfr2*$^{cKO/cKO}$ and *Fgfr1*$^{FCPG/cKO}$*; Fgfr2*$^{cKO/cKO}$ conditional mutants developed severe agenesis of the midface structures, but the phenotype was not as severe as in *Fgfr1*$^{cKO/cKO}$*; Fgfr2*$^{cKO/cKO}$ mutants. Notably, the nasal cartilage and the mandible were more severely affected in *Fgfr1*$^{FCPG/cKO}$*; Fgfr2*$^{cKO/cKO}$ conditional mutants compared to *Fgfr1*$^{F/cKO}$*; Fgfr2*$^{cKO/cKO}$ conditional mutants (Figure 4A, red arrow). A similar analysis was performed for *Fgfr2*^{F} allele to examine its phenotype (Figure 4A). We examined *Fgfr1*$^{cKO/cKO}$*; Fgfr2*$^{F/cKO}$ embryos and found that they developed more severe midline fusion and mandible defects than *Fgfr1*$^{F/cKO}$*; Fgfr2*$^{cKO/+}$ controls. Anterior skeletal structures such as the nasal cartilage, premaxilla and maxilla, and sphenoid bones were either severely reduced or absent. A striking reduction of the mandible was observed along with a complete loss of Meckel's cartilage (Figure 4A). For a more detailed phenotypic analysis, we performed micro-CT analysis for *Fgfr1*$^{F/cKO}$*; Fgfr2*$^{cKO/cKO}$, *Fgfr1*$^{FCPG/cKO}$*; Fgfr2*$^{cKO/cKO}$ and *Fgfr1*$^{cKO/cKO}$*; Fgfr2*$^{F/cKO}$ conditional mutants (Supplementary Figure S3A). Several structures were found to be differentially affected in *Fgfr1*$^{F/cKO}$*; Fgfr2*$^{cKO/cKO}$ versus *Fgfr1*$^{FCPG/cKO}$*; Fgfr2*$^{cKO/cKO}$ (summarized in Table 3). In all these cases non-neural crest derived structures such as the parietal, interparietal and supraoccipital bones remained unaffected.

Similar to *Fgfr1*$^{cKO/cKO}$*; Fgfr2*$^{cKO/cKO}$ mutants, morphological defects in *Fgfr1*$^{F/cKO}$*; Fgfr2*$^{cKO/cKO}$ and *Fgfr1*$^{FCPG/cKO}$*; Fgfr2*$^{cKO/cKO}$ embryos arose as early as E10.5. *Fgfr1*$^{FCPG/cKO}$*; Fgfr2*$^{cKO/cKO}$ embryos and, to a lesser extent, *Fgfr1*$^{F/cKO}$*; Fgfr2*$^{cKO/cKO}$ embryos developed hypoplastic nasal prominences (Supplementary Figure S3B and S3C, yellow arrow) and

mandibular prominences (Supplementary Figure S3B and S3C, red arrow) along with a midfacial cleft (Supplementary Figure S3B and S3C, yellow asterisk) compared to the littermate controls. When we examined cell death, we observed LNP specific TUNEL positive foci in both *Fgfr1*$^{FCPG/cKO}$*; Fgfr2*$^{cKO/cKO}$ and *Fgfr1*$^{F/cKO}$*; Fgfr2*$^{cKO/cKO}$ (Supplementary Figure S3D and S3E), as we had observed in *Fgfr1*$^{cKO/cKO}$*; Fgfr2*$^{cKO/cKO}$ double conditional mutants.

We next examined the role of specific signaling pathways that may be engaged coordinately by both receptors upon ligand activation. *Fgfr1*$^{C/C}$*; Fgfr2*$^{C/C}$ and *Fgfr1*$^{CPG/CPG}$*; Fgfr2*$^{CPG/CPG}$ double mutants were recovered in normal numbers, were fertile, and did not exhibit a craniofacial phenotype. We therefore focused our attention on the *F* and *FCPG* mutations. At E10.5, *Fgfr1*$^{F/-}$; *Fgfr2*$^{F/-}$ compound mutants showed growth retardation compared to *Fgfr1*$^{F/+}$; *Fgfr2*$^{F/+}$ mutant embryos. The phenotype was more severe in *Fgfr1*$^{F/-}$*; Fgfr2*$^{-/-}$ embryos (Supplementary Figure S3F). We observed phenotypic variability in these mutants even though the study was conducted on the same co-isogenic 129S4 genetic background. Axis truncation along with a defect in somite patterning was previously observed in *Fgfr1*$^{FCPG/FCPG}$ mutants (Brewer et al., 2015). *Fgfr1*$^{FCPG/-}$ mutant mice also showed growth retardation and axial patterning defects (data not shown). A similar, but more severe phenotype was observed for *Fgfr1*$^{FCPG/-}$; *Fgfr2*$^{-/-}$ mutants compared to *Fgfr1*$^{F/-}$; *Fgfr2*$^{-/-}$ (Supplementary Figure S3G). In both compound mutants, developmental delays were more acute and severe disruption of posterior structures was observed. *Fgfr1*$^{FCPG/-}$*; Fgfr2*$^{-/-}$ mutants had more severe defects in somite formation and patterning compared to *Fgfr1*$^{F/-}$*; Fgfr2*$^{-/-}$ mutants (data not shown). Both *Fgfr1*$^{F/-}$*; Fgfr2*$^{-/-}$ and *Fgfr1*$^{FCPG/-}$*; Fgfr2*$^{FCPG/-}$ were obtained at very low frequency and craniofacial defects were difficult to characterize as structures were either growth retarded or did not develop.

We did not recover *Fgfr1*$^{F/F}$; *Fgfr2*$^{F/F}$ mutant embryos at E10.5. Interestingly, we did not observe craniofacial defects in *Fgfr1*$^{F/F}$ embryos at E10.5. However, compound *Fgfr1*$^{F/F}$*; Fgfr2*$^{+/F}$ mutants displayed severe hypoplastic nasal prominence defects but mandibular development was not affected (Supplementary Figure S3F). A similar approach was taken to analyze *Fgfr1*^{FCPG} and *Fgfr2*^{FCPG} compound signaling mutants. Earlier we reported *Fgfr1*$^{FCPG/FCPG}$ mutant mice showed embryonic lethality at E10.5 with severe posterior truncations (Brewer et al., 2015). We observed similar defects in *Fgfr1*$^{FCPG/FCPG}$*; Fgfr2*$^{+/+}$ and *Fgfr1*$^{FCPG/FCPG}$*; Fgfr2*$^{+/FCPG}$ compound mutations. Morphological analysis of embryonic heads at E10.5 showed that *Fgfr1*$^{FCPG/FCPG}$*; Fgfr2*$^{+/FCPG}$ mutants developed hypoplastic nasal and mandibular prominences (Supplementary Figure S3G). *Fgfr1*$^{FCPG/FCPG}$*; Fgfr2*$^{FCPG/FCPG}$ mutants survived until E7.5 but were retarded compared to control littermates. They nonetheless still formed mesoderm, as evidenced by *Eomes* staining (Figure 4C), in contrast to double *Fgfr1*$^{-/-}$*; Fgfr2*$^{-/-}$ mutants which fail at implantation

(Kurowski et al., 2019). These results indicate that signaling mutations in both *Fgfr1* and *Fgfr2* genetically interact during development, but that the combination of the most severe signaling mutations fail to recapitulate the double null mutant phenotype.

Signaling mutations disrupt multiple intracellular pathways

FGF signaling activates numerous signaling pathways upon ligand stimulation (Brewer et al., 2016). We performed a preliminary time course for pathway activation using primary *Fgfr2*$^{+/+}$ cells at E10.5. In these cells, FGF1 led to robust ERK1/2 activation, however, the amplitude of the response was lowered by half with FGF-8b (Supplementary Figure S4A). We therefore used FGF1 for further analysis since this ligand gave the more robust response. To evaluate intracellular pathway activation downstream of wild-type FGFR2 and the FGFR2^{F}, FGFR2^{CPG} and FGFR2^{FCPG} signaling mutant receptors, we generated immortalized E10.5 FNP cell lines from the respective mouse strains also carrying a mutation in *Ink4A/Arf* to facilitate rapid immortalization of these cells. Similar to a previous study with palatal mesenchymal cells (Fantauzzo and Soriano 2017), we found that expression of facial mesenchyme markers was similar between primary and immortalized FNP cells (iFNPs; Supplementary Figure S4B). We isolated iFNPs for respective genotypes (*wt*-iFNP, *F*-iFNP, *CPG*-iFNP and *FCPG*-iFNP). These cells express undetectable levels of *Fgfr3* and *Fgfr4*, and express predominantly *Fgfr1* and, to a lesser extent, *Fgfr2* (data not shown). To interrogate signaling functions that operate specifically downstream of FGFR2, we then eliminated FGFR1 expression in each cell line by CRISPR/Cas9 mutagenesis, leaving FGFR2 as the only receptor expressed (Supplementary Figure S4C).

Using cells derived from each signaling mutant, we set forth to interrogate activation of six pivotal pathways, ERK1/2, PI3K/AKT, PLCγ, p38, STAT and JNK, known to be engaged by FGF signaling (Brewer et al., 2016). Upon stimulation with FGF1, we observed robust ERK1/2 activation in *wt*-iFNPs. ERK1/2 activation was diminished by around half for either *Fgfr2*$^{F/F}$ or *Fgfr2*$^{CPG/CPG}$ iFNPs and was only eliminated in *Fgfr2*$^{FCPG/FCPG}$ mutant cells compared to wt-iFNPs (Figure 5). Our data suggests therefore that both FRS2 and CRKL/PLCγ binding is necessary for ERK1/2 activation, similar to previous observations with *Fgfr1* (Brewer et al., 2015). PI3K/AKT signaling peaked following 5 minutes of FGF1 treatment in *wt*-iFNP cells. A similar response was also observed in *F*-iFNP cells. In *CPG*-iFNPs, a slight reduction was observed compared to either *wt*-iFNP or *F*-iFNP cells. AKT activation was reduced to a background level only in iFNP cells derived from *Fgfr2*$^{FCPG/FCPG}$ mutants (Figure 5). Therefore, CRKL and PLCγ binding appear to have more of an effect on AKT activation downstream of FGFR2 than interaction with FRS2. However, again loss of FRS2, CRKL and PLCγ binding together was necessary to abrogate

PI3K/AKT activation. We observed a robust PLCγ activation upon FGF1 treatment in *wt*-iFNP cells (Figure 5). We observed that PLCγ activation was only slightly reduced in *F*-iFNP cells. However, in *FCPG* and *CPG* mutants FGFR2 dependent PLCγ activation was reduced to background levels (Figure 5). Therefore, our results indicate that a subset of this pathway activation is FGFR2-FRS2 dependent, while for the most part interaction with Tyr769 plays a critical role. P38 activation downstream of FGF signaling is known to play an important role in vasculature development and STAT3 is involved in chondrocyte proliferation. Interestingly, a longer and sustained activation of p38 and pSTAT was observed in FGF1 treated *wt*-iFNP cells over a period of 60 mins. However, *F*-iFNPs, *CPG*-iFNPs and *FCPG*-iFNPs all failed to show activation of both P38 and pSTAT suggesting P38 and pSTAT activation require FRS2, CRKL and PLCγ for an appropriate response (Figure 5). Last, FGF receptors can signal through CRK or CRK-L to recruit Cas and activate the C3G-RAP1 pathway and JNK serine threonine kinases, independently of Ras. We observed robust JNK activation in *wt*-iFNP cells suggesting FGFR2 can also activate JNK upon FGF1 stimulation. We also saw dampened activation of the pathway in both *F*-iFNP and *CPG*-iFNP cells while JNK activation was lost in *FCPG*-iFNP cells (Figure 5). Our analysis suggests that CRK-L binding play important roles in JNK activation, but that engagement of FRS2 is also required in this pathway.

In a previous report (Brewer et al., 2015), we analyzed FGFR1 signaling output upon FGF1 stimulation. We found that FNP cells from *Fgfr1*$^{FCPG/FCPG}$ mutants resulted in a near total reduction of ERK1/2 response. However, the signaling output of FGFR1^{FCPG} was not investigated in a *Fgfr2 null* background. We used CRISPR/Cas9 to create *Fgfr2* null iFNP cells from *Fgfr1*$^{FCPG/FCPG}$*; Ink*$^{-/-}$ embryos. Upon FGF1 stimulation, we observed low pERK activation in *Fgfr1*$^{FCPG/FCPG}$ iFNP cells which peaks at 2 mins. In *Fgfr2*$^{CRISPR\text{-}KO}$*; Fgfr1*^{FCPG} iFNP cells, the overall amplitude of ERK1/2 activation was lower than in *Fgfr1*$^{FCPG/FCPG}$ iFNP, approximating the background level of activation (Supplementary Figure S4D). pAKT activation was undetectable in both *Fgfr2*$^{CRISPR\text{-}KO}$*; Fgfr1*^{FCPG} and *Fgfr2*$^{+/+}$*; Fgfr1*^{FCPG} iFNP cells (Supplementary Figure S4D and E). These results indicate that the most severe signaling mutations combinations in *Fgfr1* and *Fgfr2* effectively abrogate classic signal transduction pathways for both receptors.

A kinase dead mutation in *Fgfr2* exhibits *Fgfr2* null and additional phenotypes

The lack of a more severe phenotype in *Fgfr2* signaling mutants prompted the question of whether FGFR2 predominantly exerts its functions in a kinase dependent fashion. To address this question, we generated a kinase dead (KD) mutation at the *Fgfr2* locus in which Lys517 in the ATP binding site was converted to an alanine (Bellot et al., 1991; Hanks et al., 1988) (Figure 3A,

3C and 3D). A correctly sized FGFR2^{KD} protein of ~130Kd was found to be expressed in *Fgfr2*$^{KD/KD}$ protein lysates (Figure 3E). Although no morphological defects besides a partially penetrant kinked tail phenotype were observed at birth, fewer than expected (24/78) *Fgfr2*$^{KD/+}$ heterozygotes were recovered when *Fgfr2*$^{KD/+}$ heterozygous males were crossed to wild type females. *Fgfr2*$^{KD/+}$ heterozygous embryos were recovered in normal Mendelian ratios at E10.5 (27/60) and showed no obvious morphological defects in LNP and MNP, maxillary or mandibular prominences. During later developmental stages up to P0, *Fgfr2*$^{KD/+}$ heterozygotes also appeared normal with no limb or craniofacial abnormalities. Interestingly, *Fgfr2*$^{KD/+}$ heterozygotes exhibited a semi-dominant phenotype by postnatal day 15 (P15), when characteristic peri-ocular defects started to appear. This defect was significantly more severe than that observed in *Fgfr2*$^{F/F}$ and *Fgfr2*$^{FCPG/FCPG}$ homozygous signaling mutants. By P21, this phenotype was aggravated (Supplementary Figure S2D) and was characterized by reduced branching in the lacrimal glands along with fewer loosely held acinar cell clusters (Supplementary Figure S2E and S2F).

Upon intercrossing of *Fgfr2*$^{KD/+}$ heterozygotes, we did not recover *Fgfr2*$^{KD/KD}$ homozygotes at birth (Table 1). Since *Fgfr2*$^{-/-}$ homozygous mutants are embryonic lethal at E10.5, we undertook analysis at this stage. 6/36 (17%) *Fgfr2*$^{KD/KD}$ embryos resulting from *Fgfr2*$^{KD/+}$ heterozygote intercrosses were recovered at E10.5. Morphological examination of *Fgfr2*$^{KD/KD}$ embryos showed a characteristic absence of limb buds, a defect in the allantois which was loosely or incompletely held by the chorion to the ectoplacental cone, and a dilated pericardium (Figure 6A). These defects phenocopy those observed in *Fgfr2*$^{-/-}$ homozygous mutants at this stage. Upon further examination of *Fgfr2*$^{KD/KD}$ embryos however, we observed additional phenotypes including severe posterior truncations and a defect in forebrain development, that resulted in a rounder head compared to *Fgfr2*$^{KD/+}$ heterozygote littermates (Figure 6A). Craniofacial defects affected the FNP, as well as maxillary and mandibular prominences (Figure 6A).

To further evaluate differences in severity between the *Fgfr2*^{KD} and *Fgfr2*$^{-}$ alleles, we performed an allelic complementation study by intercrossing *Fgfr2*$^{KD/+}$ and *Fgfr2*$^{+/-}$ heterozygotes. At E10.5, 18/79 (23%) *Fgfr2*$^{KD/-}$ embryos were recovered, but six of these did not show a heartbeat. In parallel, we intercrossed *Fgfr2*$^{+/-}$ heterozygotes, resulting in a similar recovery (8/36; 22%) of *Fgfr2*$^{-/-}$ mutant embryos at E10.5. Taken together, these results demonstrate that both *Fgfr2*^{KD} and *Fgfr2*$^{-}$ alleles exhibit lethality at similar stages. Morphologically, *Fgfr2*$^{KD/-}$ embryos showed an absence of limb buds and defects in the chorio-allantoic junction along with a dilated pericardium, similar to *Fgfr2*$^{-/-}$ embryos (Figure 6A). We also observed posterior truncations defects in *Fgfr2*$^{KD/-}$ mutants, similar to *Fgfr2*$^{KD/KD}$ mutant embryos. In contrast, defects in the forebrain, medial and

lateral nasal prominences, and maxillary and mandibular prominences of *Fgfr2*$^{KD/-}$ mutants appeared less severe than in *Fgfr2*$^{KD/KD}$ mutants.

We used mRNA *in situ* hybridization to characterize the expression of *Msx1* (Figure 6B) and *Nkx2.1* (Figure 6C) in the facial prominences of *Fgfr2*$^{-/-}$, *Fgfr2*$^{KD/-}$, and *Fgfr2*$^{KD/KD}$ mutants at E10.5. We observed robust expression of *Msx1* mRNA in *Fgfr2*$^{-/-}$ and *Fgfr2*$^{KD/-}$ mutants, but it was reduced significantly in *Fgfr2*$^{KD/KD}$ homozygous mutants. *Nkx2.1* mRNA was expressed in the floor plate along facial midline in *Fgfr2*$^{-/-}$ mutants, however, it was severely affected in both *Fgfr2*$^{KD/KD}$ and *Fgfr2*$^{KD/-}$ mutants, most probably due to a semi-dominant effect of *Fgfr2*^{KD} allele. We investigated *Meox1* mRNA expression (Figure 6D) to assess axial truncation defects in *Fgfr2*$^{KD/KD}$ and *Fgfr2*$^{KD/-}$ mutants. Compared to *Fgfr2*$^{-/-}$ mutants, both *Fgfr2*$^{KD/KD}$ and *Fgfr2*$^{KD/-}$ mutants showed reduction in *Meox1* expression and reduced somite numbers. Axial defects were more severe in *Fgfr2*$^{KD/KD}$ homozygous mutants (Figure 6A). Taken together, these results indicate that the *Fgfr2*^{KD} mutation affects the same processes as the *Fgfr2*$^{-}$ allele, indicating that overall FGFR2 exerts its action in a kinase dependent way. The *Fgfr2*^{KD} mutation also exhibited additional semi-dominant effects during embryonic and postnatal development.

Cell matrix and cell adhesion properties are retained in *FCPG* relative to null mutants

Since signaling mutant cells showed near complete inactivation of classic RTK signaling activities, but the corresponding mutant mice failed to recapitulate the null mutant phenotype, we reasoned that some function engaged by FGF signaling must still be retained in the most severe *FCPG* mutants. Previous lines of evidence have implicated FGF signaling in the control of cell migration and adhesion. To further investigate the role of FGF signaling in directing cell movement, we subjected starved primary FNP cells to a transwell migration assay (Figure 7A). We observed that both PDGF (a known chemoattractant) as well as FGF treatment stimulated migration of control cells to an extent comparable to serum. *Fgfr1*$^{FCPG/cKO}$*; Fgfr2*$^{cKO/cKO}$ cells migrated upon PDGF stimulation similar to serum, however these cells showed severe migration defects upon FGF1 stimulation indicating that this process depends on active FGFR1-induced signal transduction. *Fgfr1*$^{cKO/cKO}$*; Fgfr2*$^{cKO/cKO}$ double-null mutant FNP cells also did not migrate efficiently upon FGF1 stimulation, as expected due to lack of FGF receptors. However, these cells migrated in serum and PDGF stimulated conditions, albeit to an extent lesser than control cells.

We next examined *Fgfr1*; *Fgfr2* dependent cell migration on extracellular matrix, using a scratch/ wound assay. Primary FNP cells harvested from E11.5 facial mesenchyme of either control (*Fgfr1*$^{cKO/+}$*; Fgfr2*$^{cKO/+}$), *Fgfr1*$^{FCPG/+}$*; Fgfr2*$^{cKO/+}$, or *Fgfr1*$^{cKO/cKO}$*; Fgfr2*$^{cKO/cKO}$ embryos were observed upon FGF and PDGF stimulation. Spreading of control cells over the wound during a

twelve-hour period was comparable upon FGF, PDGF, and serum stimulated conditions. Interestingly, *Fgfr1*$^{FCPG/cKO}$*; Fgfr2*$^{cKO/cKO}$ cells also showed comparable spreading capacities to control cells in all three stimulation conditions. However, *Fgfr1*$^{cKO/cKO}$*; Fgfr2*$^{cKO/cKO}$ double mutant cells failed to spread within this time frame into the wound area in response to FGF, while responses to PDGF and serum were normal (Figure 7B).

Defects in migration arise from impaired focal adhesion formation during cell spreading and cell-matrix interaction. However, it is unclear what role FGF signaling play during this process. A forward scatter plot of freshly harvested FNP cells remained unchanged across all genotypes (Supplementary Figure S5A), indicating that cell spreading defects could not be attributed to differences in cell size. We then looked at Paxillin localization by immunofluorescence as cells spread in *Fgfr1*$^{cKO/+}$*; Fgfr2*$^{cKO/+}$*; ROSA26*$^{mT/mG}$, *Fgfr1*$^{FCPG/cKO}$*; Fgfr2*$^{cKO/cKO}$*; ROSA26*$^{mT/mG}$, and *Fgfr1*$^{cKO/cKO}$*; Fgfr2*$^{cKO/cKO}$*; ROSA26*$^{mT/mG}$ double null mutant FNP cells upon treatment with FGF, PDGF, or serum over a three-hour period. We observed that both GFP^{+} *Fgfr1*$^{cKO/+}$*; Fgfr2*$^{cKO/+}$*; ROSA26*$^{mT/mG}$ control cells and *Fgfr1*$^{FCPG/cKO}$*; Fgfr2*$^{cKO/cKO}$*; ROSA26*$^{mT/mG}$ mutant cells formed numerous Paxillin enriched focal adhesions during PDGF and FGF stimulated cell-spreading, that resembled serum enriched conditions. Double null mutant cells however failed to form any Paxillin^{+} foci upon FGF treatment and subsequent cell spreading, but still responded normally to PDGF and serum (Figure 7C and Supplementary Figure S5B). Western blot analysis showed that FAK, a key regulator involved in maturation of focal contacts, was expressed at similar levels across all genotypes; however, we observed reduced pFAK levels in freshly harvested *Fgfr1*$^{cKO/cKO}$*; Fgfr2*$^{cKO/cKO}$ double mutant cells compared to *Fgfr1*$^{cKO/+}$*; Fgfr2*$^{cKO/+}$ control cells (Supplementary Figure S5C and S5D). Interestingly, double null mutant cells also showed reduced levels of Paxillin (Supplementary Figure S5C and S5D). In contrast, *Fgfr1*$^{FCPG/cKO}$*; Fgfr2*$^{cKO/cKO}$ mutant FNP cells expressed pFAK at levels comparable to *Fgfr1*$^{cKO/+}$*; Fgfr2*$^{cKO/+}$ control cells (Supplementary Figure S5C and S5D). We next investigated if FGF was also necessary for activation of pFAK in *Fgfr1*$^{FCPG/cKO}$*; Fgfr2*$^{cKO/cKO}$ mutant cells. To this end, we treated *Fgfr1*$^{cKO/+}$*; Fgfr2*$^{cKO/+}$ control, *Fgfr1*$^{FCPG/cKO}$*; Fgfr2*$^{cKO/cKO}$, and *Fgfr1*$^{cKO/cKO}$*; Fgfr2*$^{cKO/cKO}$ double mutant FNP cells with serum or FGF1 before analyzing FAK activation. pFAK levels were increased to similar levels in *Fgfr1*$^{FCPG/cKO}$*; Fgfr2*$^{cKO/cKO}$ cells as in *Fgfr1*$^{cKO/+}$*; Fgfr2*$^{cKO/+}$ control cells, upon serum or FGF stimulation (Supplementary Figure S5E). *Fgfr1*$^{cKO/cKO}$*; Fgfr2*$^{cKO/cKO}$ double null mutant cells failed to show a significant response upon FGF1 stimulation, likely due to absence of FGF receptors (Supplementary Figure S5E). These results parallel the immunofluorescence observations and indicate that cell spreading and stabilization of cell-matrix interaction are actively

governed by FGF signaling to its receptors. Interestingly, FGFR2^{FCPG} still retained this residual function and responded to FGF ligand stimulation by forming focal adhesions.

Next, we analyzed cell spreading properties in *Fgfr2*$^{FCPG/FCPG}$ -iFNP cells (*Fgfr1*$^{CRISPR-KO}$ *Fgfr2*$^{FCPG/FCPG}$) in which *Fgfr1* was inactivated. Addition of either serum, PDGF or FGF resulted in robust cell spreading and formation of Paxillin^{+} focal adhesion in *Fgfr1*$^{CRISPR-KO}$ *Fgfr2*$^{FCPG/FCPG}$ and *Fgfr1*$^{CRISPR-KO}$ *Fgfr2*$^{+/+}$ -iFNP cells (Figure 7C and Supplementary Figure S5F). *Fgfr1*$^{CRISPR-KO}$ *Fgfr2*$^{-/-}$ -iFNP cells failed to show a similar response (Figure 7C and Supplementary Figure S5F), similar to what we observed in *Fgfr1*$^{FCPG/cKO}$*; Fgfr2*$^{cKO/cKO}$ mutant primary FNP cells upon FGF1 treatment. These observations indicate that although FGFR1^{FCPG} and FGFR2^{FCPG} lose most FGF1 dependent intracellular kinase signaling outputs, they still retain functions pertaining to cell-matrix interactions. Taken together, our results suggest that FGFR1/2 regulate several cell biological processes in NCCs pertaining to cell-matrix adhesion and migration.

We were also curious to know if *Fgfr1*^{FCPG} cells could form stable cell-cell contacts comparable to control cells. We cultured freshly harvested primary GFP^{+} FNP cells from *Fgfr1*$^{cKO/+}$*; Fgfr2*$^{cKO/+}$*; ROSA26*$^{mT/mG}$ control embryos and *Fgfr1*$^{FCPG/cKO}$*; Fgfr2*$^{cKO/cKO}$*; ROSA26*$^{mT/mG}$ embryos and compared their behavior to *Fgfr1*$^{cKO/cKO}$*; Fgfr2*$^{cKO/cKO}$*; ROSA26*$^{mT/mG}$ double null mutant cells. Both *Fgfr1*$^{cKO/+}$*; Fgfr2*$^{cKO/+}$*; ROSA26*$^{mT/mG}$ control cells and *Fgfr1*$^{FCPG/cKO}$*; Fgfr2*$^{cKO/cKO}$*; ROSA26*$^{mT/mG}$ cells formed extensive cell-cell contacts in culture (Figure 7D and Supplementary Figure 5G). We observed that both control and *Fgfr1*$^{FCPG/cKO}$*; Fgfr2*$^{cKO/cKO}$*; ROSA26*$^{mT/mG}$ mutant cells formed extensive adherens junctions, marked by localized β-catenin along cell boundaries (Figure 7E). In contrast, double null mutant cells formed far fewer cell-cell contacts with no localized β-catenin accumulation, suggesting that the contacts are either unstable or that they do not mature (Figure 7E, red arrows). Last, we examined NCC cell-cell contacts *in vivo*, in the LNP. GFP^{+} cells in the mesenchyme maintained extensive cell-cell contacts within the LNP in both control and *Fgfr1*$^{FCPG/cKO}$*; Fgfr2*$^{cKO/cKO}$*; ROSA26*$^{mT/mG}$ at E11.5. Strikingly, GFP^{+} cNCCs in the double null mutant LNP were mostly isolated and interspersed (Figure 7F). Across all genotypes, cell contacts in the MNP remained unaffected (Figure 7F). Taken together, these results indicate that the most severe signaling mutations in *Fgfr1* and *Fgfr2* still retain cell-matrix and cell-cell interactions, while abrogating classic signal transduction pathways.

Discussion

Previous work has implicated FGF signaling as a critical regulator of craniofacial development. FGF8 conditional null or hypomorphic mutants exhibit defects in midface integration and mandible development (Griffin et al., 2013; Trumpp et al., 1999). *Fgfr1* conditional

mutagenesis in cNCCs leads to facial clefting (Brewer et al., 2015; Wang et al., 2013), and constitutive *Fgfr2b* or conditional *Fgfr2* mutants in the palate epithelium display a cleft palate (Hosokawa et al., 2009; Rice et al., 2004). Previous work from our laboratory and others has investigated the signaling pathways by which FGFs operate *in vivo* (Brewer et al., 2015; Eswarakumar et al., 2006; Hoch and Soriano, 2006). Although signaling through ERK1/2 has been widely thought to be a predominant pathway through which FGFs operate (Brewer et al., 2016; Lanner and Rossant, 2010), our analysis of an allelic series of signaling mutations in *Fgfr1* failed to recapitulate the null mutant phenotype, despite abrogating ERK1/2 signaling (Brewer et al., 2015). In this work, we sought to address questions raised by these findings, focusing on the relative roles for FGFR1 and FGFR2 in craniofacial development and the signaling mechanisms by which these receptors operate, and to investigate if there are non-canonical functions of FGF signaling beyond known engaged pathways that may reconcile the gap in our phenotypic analyses.

The fact that *Fgfr1c* mutants recapitulate many aspects of the *Fgfr1*$^{-/-}$ phenotype (Partanen et al., 1998), and that *Fgfr2b* mutants are reminiscent of *Fgfr2*$^{-/-}$ embryos (De Moerlooze et al., 2000), has led to the view that FGFR1 and FGFR2 predominantly function in mesenchymal or epithelial contexts, respectively. In this work, we documented extensive co-expression of the two receptors in the cNCC derived mesenchyme and in the overlying epithelia, using fluorescent *Fgfr1* and *Fgfr2* reporter alleles. We showed that both receptors function coordinately within the neural-crest derived mesenchyme as combined loss of *Fgfr1* and *Fgfr2* together in the neural crest leads to significantly more severe midface and mandibular defects than loss of each receptor alone. Midline fusion defects, increased cell death and defects in migration of the trigeminal ganglion to the mandibular branch arose at E10.5 upon loss of both receptors in the neural crest lineage. By E15.5 severe defects in the craniofacial skeleton were observed. The phenotype that we described is considerably more severe than has been previously noticed (Park et al., 2008), possibly the result of the 129S4 co-isogenic background used throughout this study, as we found a near total lack of mandible development.

Despite the known activity of FGFs as mitogens in many cell types, we did not detect a significant change in cell proliferation in *Fgfr1*$^{cKO/cKO}$*; Fgfr2*$^{cKO/cKO}$ double null mutant embryos. We observed however high levels of apoptosis in conditional double null mutants, suggesting that this process might be involved in establishing the overall mutant phenotype. Increased cell death has also been observed previously in the branchial arches of hypomorphic or conditional *Fgf8* mutants (Griffin et al., 2013; Trumpp et al., 1999). Cell death was highest in the LNP, which normally together with the maxillary prominence expand considerably and push cells towards the midline

in development. To functionally test the role of cell death, we crossed a null mutant allele for *Bim*, which antagonizes anti-apoptotic members of the BCL2 family, into the double conditional null background. This resulted in decreased cell death accompanied by a partial rescue of frontal structures, highlighting a critical role for FGF-mediated cell survival during craniofacial development. How FGF signaling might regulate cell survival remains to be determined, but BIM is a known target of phosphorylation by several MAP kinases, particularly ERK1/2 which phosphorylates BIM and targets it for ubiquitination and proteasomal degradation (Clybouw et al., 2012). JNK and PI3K/AKT activation are also known to stabilize BIM levels in cells (Lei and Davis, 2003). Cell survival through BIM may therefore be regulated by FGF since several of these signaling pathways are engaged by FGFR1 and FGFR2.

FGF signaling has been known to be important for craniofacial development, but the mechanisms by which it operates in this context had not been identified for both receptors. To determine the functionally relevant pathways that operate *in vivo*, we generated an allelic series of signaling mutations at the *Fgfr2* locus, identical to an allelic series previously designed for *Fgfr1* (Brewer et al., 2015), that prevent the binding of individual effectors. We thus disrupted binding of FRS2, a prominent pathway leading to the engagement of ERK1/2, as well as binding of CRK/CRKL, and PLCγ/GRB14, alone or in combination. Surprisingly, despite effectively preventing the binding of these signaling effectors to the receptor, we found that each of these *Fgfr2* signaling mutations gave rise to viable mice. Furthermore, we explored the effect of signaling mutations in the context of craniofacial development. We had previously observed mild craniofacial defects leading to a partially penetrant cleft palate for $Fgfr1^{F/cKO}$ and $Fgfr1^{FCPG/cKO}$ conditional NCC mutants (Brewer et al., 2015). Because *Fgfr1* and *Fgfr2* synergize in craniofacial development, we analyzed phenotypes of the signaling mutation of one receptor over the null mutation of the other receptor. Indeed, both $Fgfr1^{F}$ and $Fgfr2^{F}$ mutations placed over the null background of the other receptor showed defects in mandibular development, as well as midface closure. For *Fgfr1*, we were further able to show that specific structures, namely the frontal cartilage, as well the mandible, maxilla and squamosal bones, were more severely impacted in $Fgfr1^{FCPG}$ than in $Fgfr1^{F}$ mutants. Interestingly, $Fgfr1^{F/F}; Fgfr2^{+/F}$ embryos exhibited broad defects in midline closure, but not in mandible development, also underscoring the coordinate role of both receptors in craniofacial development. These results identify specific roles or thresholds for individual signaling pathways in discrete developmental contexts.

FGF signaling is widely thought to proceed through ERK1/2 as a downstream effector, but it is also known to engage numerous other pathways (Brewer et al., 2016). In the context of early development, the connections between FGF and ERK1/2 signaling have been particularly well

noted (Brewer et al., 2016; Lanner and Rossant, 2010). Supporting the notion that not all FGF responses are dependent on the ERK1/2 pathway, however, an RNAseq study in primary mouse embryonic palatal mesenchyme cells showed that only half of FGF regulated transcripts were sensitive to exposure to a MEK inhibitor (Vasudevan et al., 2015). ERK1/2 is thought to be primarily engaged through FRS2, but *Fgfr2*$^{F/F}$ mice were viable and our analysis of *Fgfr2*$^{F/F}$ cell signaling in a *Fgfr1* null background revealed that this mutation only resulted in about 50% reduction of ERK1/2 signaling. For *Fgfr2*, the ERK1/2 signaling pathway was only abrogated in *Fgfr2*$^{FCPG/FCPG}$ signaling alleles, similarly to *Fgfr1* (Brewer et al., 2015). Taken together, these results indicate that for both receptors, ERK1/2 engagement relies on the coordinate engagement of FRS2, CRK, and PLCγ signaling. We furthermore showed that in the absence of any other FGFR, the *Fgfr2*^{FCPG} mutation abrogates not just FGF-induced ERK1/2 signaling, but also FGF-induced PI3K/AKT, PLCγ, p38, JNK, and STAT signaling. Last, the fact that *Fgfr1*$^{FCPG/FCPG}$; *Fgfr2*$^{FCPG/FCPG}$ mutants fail to recapitulate the peri-implantation lethal double null mutant phenotype, despite abrogating expected FGF signaling activity, suggests that functions beyond those classically expected from a receptor tyrosine kinase are still active in these mutants. While our studies have been restricted to cells of neural crest origin, it will be of interest to investigate if these signaling requirements are also conserved in other contexts, for instance within epithelia.

The phenotypic gap between *Fgfr2*$^{FCPG/FCPG}$ and *Fgfr2*$^{-/-}$ mutant phenotype could either be due to heretofore unrecognized kinase-dependent signaling activity or to a kinase-independent function. To distinguish between these possibilities, we generated an inactivating *Fgfr2*^{KD} allele by introducing a mutation in the ATP binding site of the kinase domain (Bellot et al., 1991; Hanks et al., 1988). Although such kinase dead mutations have been introduced in cells or organisms ectopically, to our knowledge this is the first such knock-in allele generated in an RTK gene. This *Fgfr2* mutation resulted in lethality at E10.5, with defects in limb outgrowth and chorio-allantoic junction, highly reminiscent of the *Fgfr2*$^{-/-}$ mutant phenotype. The fact that this mutation recapitulates hallmark *Fgfr2*$^{-/-}$ mutant phenotypes supports the model that FGFR2 broadly operates in a kinase dependent fashion. Moreover, since the *Fgfr2b* constitutive mutation leads to similar limb phenotypes but no placental insufficiency (De Moerlooze et al., 2000), and phenotypes in both tissues are observed in *Fgfr2*$^{-/-}$ or *Fgfr2*$^{KD/KD}$ mutants, FGFR2 activity must be kinase-dependent in both mesenchymal and epithelial contexts. Efforts to generate a similar mutation at the *Fgfr1* locus were unsuccessful, perhaps because FGFR1 is thought to be essential for exit from pluripotency (Molotkov et al., 2017).

Interestingly, we observed semi-dominant effects in *Fgfr2*$^{KD/+}$ heterozygous mutants, primarily during postnatal development in the lacrimal gland, and more severe phenotypes in

Fgfr2$^{KD/KD}$ mutants relative to the null, affecting craniofacial and mesoderm development. FGFRs have been shown to be able to form heterodimers in culture (Bellot et al., 1991; Ueno et al., 1992). Although these have never been demonstrated *in vivo* in the absence of any over-expression, it is possible that the *Fgfr2*^{KD} allele not only inactivates *Fgfr2* but also suppresses *Fgfr1* activity through FGFR2^{KD}: FGFR1 heterodimers, wherever they are co-expressed. This would explain why *Fgfr2*^{KD} mutants still generally resemble *Fgfr2*$^{-/-}$ mutants which are lethal at a similar stage, rather than *Fgfr1*$^{-/-}$ mutants which fail at implantation on the 129S4 genetic background (Brewer et al., 2015; Kurowski et al., 2019; Molotkov et al., 2017). Previous studies have shown that other RTKs such as PDGF receptors can also function as heterodimers, giving rise to robust signaling both in terms of amplitude and duration during craniofacial development (Fantauzzo and Soriano, 2016). In cNCCs however, FGFR1: FGFR2 heterodimers would consist of FGFR1^{c} and FGFR2^{c} isoforms which would bind the same ligands, unlike the case of the PDGFRs which bind different ligands. Also, we would still expect homodimers of both receptors to be important because loss of one receptor enhances the phenotype in a conditional null background for the other. Last, while cell signaling might occur through heterodimers, this mechanism cannot fully account for the discrepancy between FCPG and null allele phenotypes for either receptor as *Fgfr1*$^{FCPG/FCPG}$*; Fgfr2*$^{FCPG/FCPG}$ double mutants develop until E7.5 with a significant degree of mesoderm formation whereas *Fgfr1; Fgfr2* double null mutants on the same genetic background die at implantation (Kurowski et al., 2019; Molotkov et al., 2017). These considerations notwithstanding, the endogenous formation and functional relevance of FGFR heterodimers remains to be tested but is a tantalizing possibility. Alternatively, it is possible that the FGFR2^{KD} receptor accumulates at the plasma membrane, soaking up ligand and thus acting as a dominant negative by titrating away ligands and/or effectors. This possibility is less probable as both alleles were knocked-in at the *Fgfr2* locus and are thus expressed at the same levels, unless the FGFR2^{KD} receptor accumulates to a much higher level than the FGFR2^{FCPG} receptor.

The inability of *Fgfr1*^{FCPG} or *Fgfr2*^{FCPG} mutations to recapitulate the *Fgfr1*$^{-/-}$ or *Fgfr2*$^{-/-}$ phenotypes, respectively, while broadly eliminating classic RTK signaling outputs for ERK1/2, PI3K, PLCγ, and additionally for FGFR2, p38, JNK and STAT1, is at first puzzling and raises multiple questions. For FGFR2, the similarity between the *Fgfr2*$^{KD/KD}$ and *Fgfr2*$^{-/-}$ mutant phenotypes indicates that an unknown signaling output which is engaged upon kinase activation has not been tested. The near complete abrogation of multiple signal transduction outputs in the most severe *Fgfr1* and *Fgfr2* signaling alleles indicates that we have interrogated relevant cell signaling pathways and raises the possibility that FGFRs possess non-canonical functions that are not impacted by our signaling mutations. Importantly, while the FCPG mutations disrupt the

ability of intracellular effectors to engage classical RTK activity, they do not abrogate the kinase activity of the receptors suggesting that both the FGFR1^{FCPG} and FGFR2^{FCPG} receptors may be able to phosphorylate targets regulating non-canonical activities.

A wide body of literature has correlated FGFRs with various aspects of cell adhesion through interactions of the extracellular domain, which remains untouched in any of our signaling mutations, with cell adhesion receptors. FGFR1 and FGFR2 interaction with FGF ligands is known to involve a third player, heparan sulfate proteoglycans (HSPGs)(Rapraeger et al., 1991; Yayon et al., 1991). Here, heparan sulfate is linked covalently to cell surface transmembrane type proteins such as Syndecans or GPI-anchored type proteins such as Glypicans (Ornitz and Itoh, 2015). Several of these HSPGs like ANOSMIN have been shown to play a role in neural crest development (Endo et al., 2012). In turn these proteins can interact with integrins, regulating cell-matrix adhesion (Geiger and Yamada, 2011; McQuade et al., 2006; Moser et al., 2009). Consistent with a role for FGFRs in regulating integrin signaling, we observed that *Fgfr1*$^{FCPG/cKO}$*; Fgfr2*$^{cKO/cKO}$ FNPs and *Fgfr1*$^{CRISPR\text{-}KO}$; *Fgfr2*$^{FCPG/FCPG}$ iFNPs were still able to form focal adhesions during cell spreading on fibronectin, in contrast to *Fgfr1; Fgfr2* double mutant FNPs. Likewise, *Fgfr1*$^{FCPG/cKO}$*; Fgfr2*$^{cKO/cKO}$ FNPs were able to migrate in scratch assays in response to FGF, unlike *Fgfr1; Fgfr2* double mutant FNPs. We furthermore showed that these phenotypes correlated with the ability for FGFs to induce FAK and Paxillin phosphorylation through wild type, FGFR1^{FCPG} or FGFR2^{FCPG} receptors. The fact that cell-matrix adhesion was FGF dependent, as seen by changes in focal adhesion formation as well as FAK or Paxillin phosphorylation, suggests that FGF binding to the receptor induces a signaling cascade that may further facilitate the activity of cell adhesion receptors. This may be furthermore enhanced by the cell adhesion complexes being brought into proximity through interaction with FGFR extracellular domains. This kinase dependent activation could occur either by direct phosphorylation of a focal adhesion component by the FGFRs, or through an intermediary such as SRC family kinases which have known roles in integrin signaling (Chen et al., 2018; Klinghoffer et al., 1999). Engagement of SRC family kinases could occur indirectly, or directly as they can bind to the FGFRs (Brewer et al., 2016; Dudka et al., 2010; Schuller et al., 2008) at a site that we have not disrupted in any of our alleles. Additionally, it is possible that defects in FGF-dependent adhesion could result in the induction of anoikis (Frisch and Francis, 1994), a process that has been previously shown to be regulated by *Bim* (Mailleux et al., 2007), potentially linking our observed adhesion defects and increase in cell death in the LNP. Last, the fact that focal adhesion assembly and phosphorylation defects have also been observed in *Fgfr1*$^{-/-}$*; Fgfr2*$^{-/-}$ keratinocytes (Meyer et al., 2012), although signaling

pathways were not investigated in that study, suggests that engagement of FGF signaling has a broad function in regulating cell adhesion in both mesenchymal and epithelial contexts.

In addition, both FGFR1 and FGFR2 are known to interact through the acid box in their extracellular domain with various cell adhesion molecules such as cadherins (Kon et al., 2019), which regulate critical events such as polarity, cell-cycle, EMT, cell-cell contacts and migration and differentiation of cNCCs (Scarpa et al., 2015). The intracellular domain of cadherins is tightly associated with the cytoskeleton through catenin adaptors, and localized RhoA and Rac1 activity at the incipient contacts stabilize these interactions and act as signaling nodes (Perez et al., 2008; Vasioukhin et al., 2000; Wheelock and Johnson, 2003). Since several cadherins might be involved during maturation of cell-cell contacts, accumulation of β- catenin has been used to investigate stable cell-cell contacts during neural crest migration (Nakagawa and Takeichi, 1995). Consistent with a role for FGFRs in mediating cell-cell adhesion through cadherins, we observed that both *Fgfr1*$^{FCPG/cKO}$ *Fgfr2*$^{cKO/cKO}$ FNPs and *Fgfr1*$^{CRISPR\text{-}KO}$ *Fgfr2*$^{FCPG/FCPG}$ iFNPs were able to make strong cell contacts between themselves, as shown by β-catenin accumulation at the junctions, in contrast to double null mutant cells. We observed poor cell-cell adhesion not only among primary FNP cells in culture, but also *in vivo*, where *Fgfr1*$^{-/-}$; *Fgfr2*$^{-/-}$ mutant cells showed very limited aggregation in the LNP. FGFR1/2 interaction with cadherins may thus have a dual role, one in promoting cell motility through FGF-induced ERK1/2 signaling (Kon et al., 2019), and an opposite one in cell adhesion, as ERK1/2 signaling is abrogated in *Fgfr1*^{FCPG} and *Fgfr2*^{FCPG} mutants. During epithelial to mesenchymal transition, including neural crest cell delamination, FGF signaling regulates cadherin switching (Ciruna and Rossant, 2001; Nieto et al., 2016; Sun et al., 1999). FGF signaling also regulates E-cadherin localization, and in the absence of *Fgfr1*, E-cadherin polarization is affected in the mural trophectoderm in mouse (Kurowski et al., 2019) and in zebrafish cardiomyocytes (Rasouli et al., 2018). Taken together, our results indicate that FGFRs regulate processes such as cell adhesion, and possibly more, beyond their classic signaling cascades (Figure 7G). Additional genetic, biochemical and cell biological studies may identify further non-canonical roles for these receptors beyond their traditional activities in signal transduction.

Acknowledgments. We thank Jia Li and Chantel Dixon for technical assistance; Elaine Fuchs for helpful insights into cell adhesion mechanisms; Jerry Chipuk for conversations about cell death; Colin Dinsmore for extensive discussions; and our laboratory colleagues, Stu Aaronson, Rob Krauss, and Sergei Sokol for critical comments on the manuscript. We thank the NYU School of Dentistry Micro-CT Core and the Mt. Sinai Flow Cytometry and Microscopy facilities for assistance and advice. This work was supported in part by the Tisch Cancer Institute at Mount Sinai (P30 CA196521 Cancer Center Support Grant for access to Mt. Sinai cores) and by grant RO1 DE022778 from NIH/NIDCR to P.S.

Figure Legends

Figure 1: Defects in craniofacial morphogenesis and organogenesis in *Fgfr1*$^{cKO/cKO}$; *Fgfr2*$^{cKO/cKO}$ double mutants.

(A) Spatial domain of FGFR1 and FGFR2 expression in facial prominences at E10.5. GFP and mCherry immunohistochemistry was used to detect expression from *Fgfr1-GFP* and *Fgfr2-mCherry* reporter alleles. GFP expression was primarily restricted to the mesenchyme (yellow arrow). Although mCherry expression was restricted to the epithelium, many cells in the mesenchyme also express mCherry (red arrow). mCherry expression is downregulated in the epithelium lining the nasal pit (yellow asterix).

(B) Alcian blue/ alizarin red staining of mouse skull at E18.5 from various genotypes. Conditional mutation of *Fgfr2* (*Fgfr2*$^{cKO/cKO}$) or *Fgfr1-Fgfr2* conditional heterozygotes (*Fgfr1*$^{cKO/+}$; *Fgfr2*$^{cKO/+}$) did not show defects. A facial cleft was observed in *Fgfr1*$^{cKO/cKO}$ embryo. The phenotype was exacerbated in *Fgfr1*$^{cKO/cKO}$; *Fgfr2*$^{cKO/+}$ mutants. *Fgfr1*$^{cKO/cKO}$; *Fgfr2*$^{cKO/cKO}$ double mutants exhibited the most severe defect, with agenesis of proximal skull structures, as well as severe reduction of the mandible.

(C) Conditional *Fgfr1-Fgfr2* mutant embryos crossed to *ROSA26*$^{mT/mG}$ reporter analyzed in whole mount. cNCC in the head express GFP (green). At E9.5 (top panel), *Fgfr1/2* conditional double mutants (*Fgfr1*$^{cKO/cKO}$; *Fgfr2*$^{cKO/cKO}$; *ROSA26*$^{mT/mG}$) had a hypoplastic pharyngeal arch, PA1 and PA2 (yellow arrow), marked by reduced fluorescence of GFP^{+} NCCs compared to *Fgfr1-Fgfr2* conditional heterozygotes. *Fgfr1*$^{cKO/+}$; *Fgfr2*$^{cKO/cKO}$ and *Fgfr1*$^{cKO/cKO}$; *Fgfr2*$^{cKO/+}$ mutants appeared normal at this stage. Frontal view at E10.5 (lower panels). A wide midline separation was observed in both *Fgfr1/2* conditional double (*Fgfr1*$^{cKO/cKO}$; *Fgfr2*$^{cKO/cKO}$; *ROSA26*$^{mT/mG}$) and *Fgfr1*$^{cKO/cKO}$; *Fgfr2*$^{cKO/+}$; *ROSA26*$^{mT/mG}$ mutants (yellow asterisk) compared to controls and *Fgfr1*$^{cKO/+}$; *Fgfr2*$^{cKO/cKO}$; *ROSA26*$^{mT/mG}$ mutants.

(D) Whole mount mRNA *in situ* hybridization was used to compare expression of *Alx3, Msx1, Six3, Nkx2.1, Fgf8* and *Shh* at E10.5 in the facial primordia for *Fgfr1*$^{cKO/+}$; *Fgfr2*$^{cKO/+}$ control and *Fgfr1*$^{cKO/cKO}$; *Fgfr2*$^{cKO/cKO}$ mutants. Compared to the controls, *Fgfr1/2* conditional double mutants showed no expression of *Alx3*, *Six3* and *Nkx2.1.* Reduced *Msx1* expression was observed. The expression of *Fgf8* and *Shh* remain unaffected in the *Fgfr1*$^{cKO/cKO}$; *Fgfr2*$^{cKO/cKO}$ mutants.

(E) Craniofacial morphogenesis at E12.5 in sagittal and frontal views of DAPI-stained *Fgfr1*$^{cKO/cKO}$; *Fgfr2*$^{cKO/cKO}$ and *Fgfr1*$^{cKO/+}$; *Fgfr2*$^{cKO/+}$ control embryos. A prominent defect in the mandibular process (yellow arrow) and a facial cleft (yellow asterisk) was observed in the *Fgfr1*$^{cKO/cKO}$; *Fgfr2*$^{cKO/cKO}$ mutants.

(F) Whole mount immunostaining for neurofilament marker 3A10 at E10.5 revealed defects in the trigeminal ganglion in *Fgfr1*$^{cKO/cKO}$*; Fgfr2*$^{cKO/cKO}$ mutants. Trigeminal nerve failed to reach the anterior region of the mandibular arch (red arrow) in *Fgfr1*$^{cKO/cKO}$*; Fgfr2*$^{cKO/cKO}$ mutants.

(G) Alcian blue/ alizarin red staining of mouse skulls at E14.5. Alizarin red staining mark ossified region in mandible and maxilla in control (*Fgfr1*$^{cKO/+}$*; Fgfr2*$^{cKO/+}$*)* skull. Yellow arrowhead marks the Meckel's cartilage. In *Fgfr1*$^{cKO/cKO}$*; Fgfr2*$^{cKO/+}$ mutants, we observed reduced ossification (red arrowhead) in the mandible with a significantly smaller Meckel's cartilage (yellow arrowhead). Meckel's cartilage was lost in *Fgfr1/2* conditional double mutant with no observable ossification.

(H) Micro-CT analysis of ossified structures in the head at E18.5. Compared to the control, we observed an overall reduction or a complete loss of ossification of neural crest derived facial bones in *Fgfr1/2* conditional double mutant. Frontal and nasal bones, pre-maxilla and maxilla were severely affected. Mesoderm derived bones including parietal and interparietal bones remained unaffected (yellow asterisk). *Fgfr1*$^{cKO/cKO}$*; Fgfr2*$^{cKO/+}$ mutants showed an overall reduction in the size of the mandible, with the proximal structures most severely affected.

Figure 2: Craniofacial morphogenesis defects in double mutants associated with reduced number of neural crest cells and localized cell death.

(A) GFP^{+} (green) neural crest cell lineage cell-distribution at E10.5 in *Fgfr1*$^{cKO/+}$*; Fgfr2*$^{cKO/+}$; *ROSA26*$^{mT/mG}$ controls compared to *Fgfr1*$^{cKO/+}$*; Fgfr2*$^{cKO/cKO}$; *ROSA26*$^{mT/mG}$, *Fgfr1*$^{cKO/cKO}$*; Fgfr2*$^{cKO/+}$; *ROSA26*$^{mT/mG}$ and *Fgfr1*$^{cKO/cKO}$*; Fgfr2*$^{cKO/cKO}$; *ROSA26*$^{mT/mG}$ mutants. Reduced levels of GFP+ cells in the PA1 PA2 and migratory stream were observed in *Fgfr1*$^{cKO/cKO}$*; Fgfr2*$^{cKO/cKO}$; *ROSA26*$^{mT/mG}$ mutants (yellow arrow).

(B) Flow sorting was used to quantify the percentage of GFP+ cells in the nasal prominences, maxillary and mandibular prominences at E10.5 embryo across various genotypes. The number of GFP^{+} cells in *Fgfr1*$^{cKO/cKO}$*; Fgfr2*$^{cKO/cKO}$; *ROSA26*$^{mT/mG}$ double mutants was reduced by half compared to controls. The proportion of GFP+ cells remain unchanged in *Fgfr1*$^{cKO/cKO}$*; Fgfr2*$^{cKO/+}$; *ROSA26*$^{mT/mG}$ mutants although they exhibited observable phenotypic defects.

(C) No change in the proliferation index of GFP^{+} neural crest lineage cells was observed at E10.5 in the MNP and LNP across various genotypes, by EdU incorporation.

(D) Quantification of percentage of EdU^{+} cells normalized to GFP+ neural crest lineage cells, in control versus double mutant cells.

(E) Apoptosis was examined at E10.5 by TUNEL staining on sections from facial prominences, MNP and LNP. Increased TUNEL positive cells were observed *Fgfr1/2* double mutants in the LNP

compared to controls. The MNP had fewer TUNEL positive cells than the LNP in all the mutants examined.

(F) Quantitation of TUNEL positive foci across different mutant genotypes show a 40-fold increase in cell death in *Fgfr1/2* double mutants in the LNP at E10.5.

(G) Inferior view (mandibles removed) of alcian blue alizarin red stained mouse skull at E17.5 from $Fgfr1^{cKO/cKO}; Fgfr2^{cKO/+}; Bim^{+/+}$ and $Fgfr1^{cKO/cKO}; Fgfr2^{cKO/+}; Bim^{+/-}$ embryos. Severely affected medial elements such as nasal cartilage and palatine (PL) process, premaxilla (PMX), maxilla (MX) and palatal shelves (PS) showed partial rescue and a by 2-fold reduction in midline separation reduction in $Fgfr1^{cKO/cKO}; Fgfr2^{cKO/+}; Bim^{+/-}$ littermate embryos.

(H) Frontal views of control $Fgfr1^{cKO/+}; Fgfr2^{cKO/+}; Bim^{+/+}$, $Fgfr1^{cKO/cKO}; Fgfr2^{cKO/cKO}; Bim^{+/+}$, and $Fgfr1^{cKO/cKO}; Fgfr2^{cKO/cKO}; Bim^{+/-}$ embryos at E17.5 showing partial rescue by reduction in *Bim* levels.

Figure 3: Allelic series of *Fgfr2* signaling mutations.

(A) Schematic representation of allelic series of *Fgfr2* signaling mutations created for the study. Critical effectors that bind to FGFR2 are listed on the left of the $Fgfr2^{WT}$ allele (WT). Corresponding residues critical for this binding are annotated on the right. Amino acid substitutions for each allele is provided to the right of all mutant alleles generated, namely F, C, PG, CPG, FCPG, KD for $Fgfr2^{F}$, $Fgfr2^{C}$, $Fgfr2^{PG}$, $Fgfr2^{CPG}$, $Fgfr2^{FCPG}$ and $Fgfr2^{KD}$, respectively.

(B) Coimmunoprecipitations of signaling proteins Frs2, CrkL and PLCγ with the indicated allele of *Fgfr2-Flag3x* in 3T3 cells. Cells were transfected with triple-Flag-tag cDNA corresponding to c-isoform of $Fgfr2^{WT}$ and signaling mutant constructs $Fgfr2^{PG}$, $Fgfr2^{CPG}$, $Fgfr2^{F}$ and $Fgfr2^{FCPG}$. Following serum starvation, cells were stimulated with FGF1 (50 ng/ml) and heparin (5 μg/ml) for 15 minutes. Co-immunoprecipitation experiments confirmed ability of F, C and PG mutations to disrupt FRS2, CRKL and PLCγ binding to FGFR2, respectively. (IP) Immunoprecipitation; (IB) immunoblot. Coimmunoprecipitation data show that FRS2, CRKL and PLCγ physically interact with $FGFR2^{WT}$.

(C) Representation of WT locus, targeting vectors and the corresponding targeted loci for C allele, PG allele and F allele, and *Fgfr2* locus after FCPG targeting, and the KD allele. Targeting vectors C, PG and F introduced mutations Y466F, Y769F/Y779F and L434A/R426A sequentially at the *Fgfr2* locus, respectively. Targeting vector for KD allele introduced the K517A mutation. ES cells were targeted first with C targeting vector generating $Fgfr2^{+/C}$ mutant cells. $Fgfr2^{+/C}$ ES cells were targeted with PG targeting vector generating either $Fgfr2^{C/PG}$ or $Fgfr2^{+/CPG}$ mutant cells. Finally, $Fgfr2^{+/CPG}$ were targeted with F targeting vector resulting in $Fgfr2^{F/CPG}$ or $Fgfr2^{+/FCPG}$ mutant

ES cells. Multiple LoxP sites were introduced at the *Fgfr2* locus during successive rounds of targeting, and the neo cassette was removed in vivo or in culture prior to generating signaling mouse mutants. Abbreviation: L, loxP site; F, FRT site; DTA, Diptheria toxin A cassette; Neo, Neomycin resistance cassette.

(D) Southern blot confirmation for proper targeting of F, C, PG and KD mutations at the *Fgfr2* locus. 5' probes used for each targeting events are indicated. BamHI restriction enzyme generated 5kb and 2.6kb band for WT and F targeted loci, respectively. SphI digestion generated 10kb and 8.4 kb fragment for WT and C targeted loci, respectively. KpnI digestion generated a 5.6kb band for WT locus and 7.6kb band for PG targeted locus. EcoRI and EcoRV restriction digestion generated 7.7kb WT fragment and 9.7kb KD-mutant fragment.

(E) Western blot from cells harvested from wild-type and $Fgfr2^{KD/KD}$ embryos show full length $FGFR2^{KD}$ protein expression.

Figure 4: Coordinate *Fgfr1* and *Fgfr2* signaling mutant phenotypes in development.

(A) Sagittal view of skeletal preparations from control $Fgfr1^{cKO/+}$; $Fgfr2^{cKO/cKO}$ compared to signaling mutant $Fgfr1^{F/cKO}$; $Fgfr2^{cKO/cKO}$ and $Fgfr1^{FCPG/cKO}$; $Fgfr2^{cKO/cKO}$ embryos at E16.5 (upper row). In $Fgfr1^{F/cKO}$; $Fgfr2^{cKO/cKO}$ embryo, the frontal bone, nasal cartilage (NC), squamosal bone (SQ), tympanic bulla (T), maxilla (MX) and mandible (MD) were affected. $Fgfr1^{FCPG/cKO}$; $Fgfr2^{cKO/cKO}$ mutants at E16.5 showed a more severe defect. The nasal cartilage, maxilla and squamosal bones were more severely affected in $Fgfr1^{FCPG}$ than $Fgfr1^{F}$, as was the mandible (red arrow). Sagittal views comparing skeletal defects in $Fgfr1^{cKO/cKO}$; $Fgfr2^{F/cKO}$ with control $Fgfr1^{cKO/cKO}$; $Fgfr2^{cKO/+}$ mutants (lower row). Compared to the control, $Fgfr2^{F}$ signaling mutant showed a further reduction of the mandible along with reduced ossification of the premaxilla (PMX) and maxilla and loss of the squamosal bone and tympanic bulla.

(B) DAPI stained frontal view of the face for $Fgfr1^{F}$ and $Fgfr2^{F}$ mutant embryos at E15.5. $Fgfr1^{F/F}$; $Fgfr2^{+/F}$ embryos showed a severe facial cleft compared to other genotypes.

(C) CDX2 and EOMES wholemount immunofluorescence in $Fgfr1^{FCPG}$ and $Fgfr2^{FCPG}$ compound signaling mutants at E7.5. In contrast to $Fgfr1^{-/-}$; $Fgfr2^{-/-}$ which fail to implant on the 129S4 co-isogenic background, we could recover $Fgfr1^{FCPG/FCPG}$; $Fgfr2^{FCPG/FCPG}$ compound mutants at E7.5 but not at E10.5. $Fgfr1^{FCPG/FCPG}$; $Fgfr2^{FCPG/FCPG}$ mutants were growth retarded but express mesodermal EOMES and trophectoderm marker, CDX2.

Figure 5: FGFR2 signaling outputs upon FGF1 stimulation.

(A) iFNP cells derived from the indicated genotypes, *Fgfr2*$^{wt/wt}$ (*R2*$^{wt/w}$), *Fgfr2*$^{F/F}$ (*R2*$^{F/F}$), *Fgfr2*$^{CPG/CPG}$ (*R2*$^{CPG/CPG}$) and *Fgfr2*$^{FCPG/FCPG}$ (*R2*$^{FCPG/FCPG}$), were serum starved overnight and stimulated with 50 ng/mL FGF1 and 5 µg/mL heparin for the indicated times (0-60 mins). Phospho-blots were stripped and reblotted with GAPDH for loading controls (shown here as an example just for the pERK1/2, pP38 and pPLCγ blot). Activation of pERK1/2, pAKT, pP38, pPLCγ, pJNK and pSTAT3 was investigated.

(B-G) Quantification of pathway activation for (B) pERK1/2, (C) pAKT, (D) pP38, (E) pPLCγ, (F) pJNK and (G) pSTAT3 normalized to the loading control GAPDH, is reported as mean ± standard deviation with a minimum of three independent biological replicates.

Figure 6: A kinase dead mutation in *Fgfr2* recapitulates multiple aspects of the *Fgfr2*$^{-}$ phenotype.

(A) Morphological examination of *Fgfr2* kinase dead phenotype at E10.5. *Fgfr2*$^{KD/+}$ heterozygotes showed no obvious morphological defects in lateral, medial nasal, maxillary or mandibular prominences at E10.5 and resembled *Fgfr2*$^{+/+}$ and *Fgfr2*$^{+/-}$ control embryos. In contrast, obvious defects were observed in *Fgfr2*$^{KD/-}$ and *Fgfr2*$^{KD/KD}$ mutants. These mutants exhibited absence of limb buds (red arrow), and defects in the allantois which was loosely or incompletely held by the chorion to the ectoplacental cone, along with a dilated pericardium similar to *Fgfr2*$^{-/-}$ mutants. Both *Fgfr2*$^{KD/-}$ and *Fgfr2*$^{KD/KD}$ mutants displayed severe posterior truncations and *Fgfr2*$^{KD/KD}$ mutants showed a more severe phenotype. *Fgfr2*$^{KD/KD}$ mutants also displayed craniofacial defects with poorly developed medial and lateral nasal prominences compared to *Fgfr2*$^{KD/-}$ mutants.

(B) Wholemount mRNA *in situ* hybridization for *Msx1* at E10.5. *Msx1* was expressed in the facial prominences (LNP, MNP and mandibular prominences) in *Fgfr2*$^{-/-}$ embryos at similar levels compared to control *Fgfr2*$^{+/-}$ embryo. *Msx1* expression was also observed in *Fgfr2*$^{KD/-}$ mutants. However, reduced expression was observed in *Fgfr2*$^{KD/KD}$ mutants.

(C) Wholemount mRNA in situ hybridization for *Nkx2.1*. *Nkx2.1* was expressed in the midline floor plate of *Fgfr2*$^{-/-}$ mutants. Expression of *Nkx2.1* was not detected in *Fgfr2*$^{KD/-}$ and *Fgfr2*$^{KD/KD}$ mutants.

(D) *Meox1* mRNA expression was observed in somites of E10.5 *Fgfr2*$^{-/-}$ mutants comparable to control *Fgfr2*$^{+/-}$ embryos. Severe reduction in level of expression in the anterior somites was observed in both *Fgfr2*$^{KD/-}$ and *Fgfr2*$^{KD/KD}$ mutants (black arrows) along with defects in axis elongation and posterior somite formation (red arrow).

Figure 7: FGF regulated cell adhesion properties are retained in *Fgfr2* signaling mutants.

(A) Transwell cell-migration assay upon FGF stimulation for control (*Fgfr1*$^{cKO/+}$*; Fgfr2*$^{cKO/+}$), *Fgfr1*$^{FCPG/cKO}$*; Fgfr2*$^{cKO/cKO}$, and *Fgfr1*$^{cKO/cKO}$*; Fgfr2*$^{cKO/cKO}$ double mutant cells. Control cells and *Fgfr1*$^{FCPG/cKO}$*; Fgfr2*$^{cKO/cKO}$ showed active migration in serum treated conditions as well as when cells were treated with either FGF1 (50ng/mL) and PDGFA (30ng/mL). *Fgfr1*$^{cKO/cKO}$*; Fgfr2*$^{cKO/cKO}$ double mutant cells showed reduced migration upon FGF stimulation but not PDGF treatment.

(B) Scratch/wound healing assay of control (*Fgfr1*$^{cKO/+}$*; Fgfr2*$^{cKO/+}$), *Fgfr1*$^{FCPG/cKO}$*; Fgfr2*$^{cKO/cKO}$, and *Fgfr1*$^{cKO/cKO}$*; Fgfr2*$^{cKO/cKO}$ double mutant cells. Control cells and *Fgfr1*$^{FCPG/cKO}$*; Fgfr2*$^{cKO/cKO}$ cells showed active spreading in serum treated conditions as well as when cells were treated with either FGF1 (50ng/mL) and PDGFA (30ng/mL) compared to serum starved conditions. Spreading of *Fgfr1*$^{cKO/cKO}$*; Fgfr2*$^{cKO/cKO}$ double mutant cells was very limited upon FGF stimulation but extensive in both PDGF or serum treated conditions.

(C) Focal-adhesion complex formation, as assayed by Paxillin immunostaining, in GFP^{+} *Fgfr1*$^{cKO/cKO}$*; Fgfr2*$^{cKO/cKO}$*; ROSA26*$^{mT/mG}$ double mutant FNP cells. In the top panels, *Fgfr1*$^{cKO/+}$*; Fgfr2*$^{cKO/+}$*; ROSA26*$^{mT/mG}$ control, *Fgfr1*$^{FCPG/cKO}$*; Fgfr2*$^{cKO/+}$*; ROSA26*$^{mT/mG}$, and *Fgfr1*$^{cKO/cKO}$*; Fgfr2*$^{cKO/cKO}$*; ROSA26*$^{mT/mG}$ double mutant primary FNP cells were initially starved and treated with 50ng/mL FGF1, 30ng/mL PDGFA or 15% fetal calf serum for 3 hours before analyzing for Paxillin localization at the focal adhesion points. In control cells and *Fgfr1*$^{FCPG/cKO}$*; Fgfr2*$^{cKO/+}$, we detected multiple Paxillin^{+} foci upon serum stimulation or treatment with either FGF1, PDGFA, or serum. *Fgfr1*$^{cKO/cKO}$*; Fgfr2*$^{cKO/cKO}$*; ROSA26*$^{mT/mG}$ double mutant FNP cells failed to show paxillin accumulation at the focal adhesions in response to FGF, but not in response to PDGF or serum. In the lower panels, cell spreading properties were analyzed for *Fgfr2*$^{WT/WT}$ (*Fgfr1*$^{CRISPR\text{-}KO}$ *Fgfr2*$^{WT/WT}$), *Fgfr2*$^{FCPG/FCPG}$ (*Fgfr1*$^{CRISPR\text{-}KO}$ *Fgfr2*$^{FCPG/FCPG}$), and *Fgfr2*$^{-/-}$ (*Fgfr1*$^{CRISPR\text{-}KO}$ *Fgfr2* $^{CRISPR\text{-}KO}$) -iFNP cells in which *Fgfr1* was inactivated. Addition of either serum, PDGF or FGF resulted in robust cell spreading and formation of Paxillin^{+} focal adhesion in *Fgfr1*$^{CRISPR\text{-}KO}$ *Fgfr2*$^{FCPG/FCPG}$ and *Fgfr1*$^{CRISPR\text{-}KO}$ *Fgfr2*$^{+/+}$ -iFNP cells. *Fgfr2*$^{-/-}$ -iFNP cells (*Fgfr1*$^{CRISPR\text{-}KO}$ *Fgfr2* $^{CRISPR\text{-}KO}$) showed severe defects in focal adhesion formation.

(D) Freshly harvested and subsequently cultured primary GFP^{+} FNP cells from control *Fgfr1*$^{cKO/+}$*; Fgfr2*$^{cKO/+}$*; ROSA26*$^{mT/mG}$ and *Fgfr1*$^{FCPG/cKO}$*; Fgfr2*$^{cKO/cKO}$*; ROSA26*$^{mT/mG}$ embryos were compared with *Fgfr1*$^{cKO/cKO}$*; Fgfr2*$^{cKO/cKO}$*; ROSA26*$^{mT/mG}$ double null mutant cells in terms of their ability to form cell-cell contacts. We observed that both control and *Fgfr1*$^{FCPG/-}$*; Fgfr2*$^{-/-}$ mutant cells formed extensive cell-cell contacts, in contrast to *Fgfr1*$^{cKO/cKO}$*; Fgfr2*$^{cKO/cKO}$*; ROSA26*$^{mT/mG}$ double null mutant cells.

(E) β-catenin accumulated along the cell contact boundaries between GFP$^+$ FNP cells from control *Fgfr1*$^{cKO/+}$*; Fgfr2*$^{cKO/+}$*; ROSA26*$^{mT/mG}$ and *Fgfr1*$^{FCPG/cKO}$*; Fgfr2*$^{cKO/cKO}$*; ROSA26*$^{mT/mG}$ embryos in contrast to GFP$^+$ FNP cells from *Fgfr1*$^{cKO/cKO}$*; Fgfr2*$^{cKO/cKO}$*; ROSA26*$^{mT/mG}$ double *null* mutants.

(F) Cell-cell contacts were analyzed *in vivo* in control *Fgfr1*$^{cKO/+}$*; Fgfr2*$^{cKO/+}$*; ROSA26*$^{mT/mG}$ and *Fgfr1*$^{FCPG/cKO}$*; Fgfr2*$^{cKO/cKO}$*; ROSA26*$^{mT/mG}$ and were compared with *Fgfr1*$^{cKO/cKO}$*; Fgfr2*$^{cKO/cKO}$*; ROSA26*$^{mT/mG}$ double null mutants at E11.5. GFP$^+$ cells in *Fgfr1*$^{cKO/+}$*; Fgfr2*$^{cKO/+}$*; ROSA26*$^{mT/mG}$ and *Fgfr1*$^{FCPG/cKO}$*; Fgfr2*$^{cKO/cKO}$*; ROSA26*$^{mT/mG}$ FNP cells formed clusters in both developing LNP and MNP at this stage. In contrast, GFP$^+$ cells remained sparsely populated in the LNP of *Fgfr1/2* double null mutants and did not form clusters.

(G) Model of FGF-mediated cell signaling pathways. In wild-type (WT) cells, activation by FGFs engages a classical RTK signal transduction pathway, leaving to the activation of ERK1/2, PI3K/AKT, PLCγ, and additional pathways. In addition, FGFs activate both cell-matrix as well as cell-cell adhesion, in a kinase-dependent manner, possibly facilitated through interactions of the FGF receptors through their extracellular domain with cell adhesion receptors. *Fgfr1*^{FCPG} or *Fgfr2*^{FCPG} mutant cells fail to activate a classical RTK signal transduction pathway (light grey) but can still promote cell adhesion (black), as their kinase activity has not been disrupted. In null mutant cells, neither FGF-induced cell signaling or cell adhesion are observed (light grey), since the receptors are not expressed.

Supplementary Figure S1

(A) Spatial domain of FGFR1 and FGFR2 expression in craniofacial skeleton at E17.5. GFP and mCherry immunohistochemistry was used to detect expression from *Fgfr1-GFP* and *Fgfr2-mCherry* reporter alleles. Co-expression of both FGFR1-GFP and FGFR2-mCherry was observed on the cartilage and the perichondrium (yellow arrow).

(B) Quantification of skull length, intercanthal distance, length of frontal and nasal bone for different genotypes measured in millimeters (mm).

(C) Sagittal view of alcian blue/ alizarin red stained mouse skull at E16.5 for different genotypes. Frontal and nasal bone, mandible, premaxilla, maxilla and the squamous bone was severely affected in *Fgfr1*$^{cKO/cKO}$*; Fgfr2*$^{cKO/cKO}$ conditional double mutants. In *Fgfr1*$^{cKO/cKO}$*; Fgfr2*$^{cKO/+}$ mutants also showed partial mandibular defect where proximal condylar (CDP), coronoid (CRP) and angular process (AGP) of the mandible was affected.

(D) Histological examination at E15.5 showed defective organogenesis in multiple organs, including the palate, tongue, and skeleton. In the double mutants several skeletal structures such as palate (P), nasopharyngeal lumen (N) and pre-sphenoid (PS) were affected compared to the

controls. Non-neural crest derived tissues such as tongue was also affected. SMA immunofluorescence showed organized muscle fiber differentiation in controls. In the *Fgfr1/2* mutants, muscle fiber differentiation appeared random and disorganized.

(E) Differentiation of craniofacial skeleton was assessed by studying expression of cartilage differentiation marker, *Col2a1,* on sections. mRNA *in situ* hybridization analysis at E14.5 showed *Col2a1* expression in the chondrocranium (skull base) and mandible in the control. In the double mutants however, expression was restricted to a narrow band of cells in the skull base. Expression of *Col2a1* and of *Col10a1* and Runx2 (mature cartilage markers) was assessed at E17.5 on sections. *Col2a1* mRNA expression was restricted to the skull base, mandible and frontal bone in controls. Similar expression was also observed in conditional double mutants. At E17.5, *Col10a1* mRNA expression was much broader in the controls. In conditional double mutants *Col10a1* expression was undetectable suggesting a block in terminal chondrogenic differentiation. We detected expression of mature cartilage and late osteoblast marker, RUNX2, in both controls and the conditional double mutants.

(F) Increased cell-death observed in conditional double mutants was partially rescued in $Fgfr1^{cKO/cKO}$; $Fgfr2^{cKO/cKO}$; $Bim^{+/-}$ mutants at E10.5. More $TUNEL^{+}$ cells were observed in the LNP in $Fgfr1^{cKO/cKO}$; $Fgfr2^{cKO/cKO}$ and $Fgfr1^{cKO/cKO}$; $Fgfr2^{cKO/+}$ mutants compared to corresponding $Fgfr1^{cKO/cKO}$; $Fgfr2^{cKO/cKO}$; $Bim^{+/-}$ and $Fgfr1^{cKO/cKO}$; $Fgfr2^{cKO/+}$; $Bim^{+/-}$ counterparts. Quantification of TUNEL positive foci in $Fgfr1^{cKO/cKO}$; $Fgfr2^{cKO/cKO}$; $Bim^{+/-}$ showed a 1.4 times reduction in cell death.

Supplementary Figure S2

(A) Growth rate (in terms of weight gain) of homozygous $Fgfr2^{F/F}$, $Fgfr2^{C/C}$, $Fgfr2^{PG/PG}$, $Fgfr2^{CPG/CPG}$, and $Fgfr2^{FCPG/FCPG}$ female versus control until 6 weeks shown as mean ± SEM. * indicate p value <0.05. We noted a decrease in growth rate for $Fgfr2^{F/F}$, $Fgfr2^{PG/PG}$, and $Fgfr2^{FCPG/FCPG}$ mutant mice compared to control was noted.

(B) $Fgfr2^{PG/PG}$ and $Fgfr2^{CPG/CPG}$ skeletal preparation at P0 showed fusion of the caudal vertebrae, resulting in kinked tail phenotype and in the most extreme case in a curly tail phenotype (black arrow). Hemizygote $Fgfr2^{C/-}$, $Fgfr2^{PG/-}$ and $Fgfr2^{CPG/-}$ mice were weighed at 6 weeks. $Fgfr2^{PG/-}$ appeared smaller than their control littermate.

(C) Whole mount immunohistochemistry for neurofilament staining revealed trigeminal nerve defects at E10.5 in $Fgfr2^{FCPG/-}$ embryo but not in $Fgfr2^{F/-}$. In $Fgfr2^{F/+}$, $Fgfr2^{FCPG/+}$ and $Fgfr2^{F/-}$ embryos, trigeminal nerve migrated to anterior domain of the PA1 (red arrow) at E10.5. Trigeminal nerves fail to migrate into the pharyngeal arch of $Fgfr2^{FCPG/-}$ mutants.

(D) Sagittal view of left eye at P21 for the mentioned genotypes. Both *Fgfr2*$^{F/F}$ and *Fgfr2*$^{FCPG/FCPG}$ mice showed fully penetrant defects with onset at P15 which included laceration around the eye. We observed similar defects in *Fgfr2*$^{KD/+}$ mutants.

(E) Lacrimal gland from signaling mutants were dissected at P5 and stained with acetocarmine. Representative images are shown here for *Fgfr2*$^{F/F}$, *Fgfr2*$^{FCPG/FCPG}$ and *Fgfr2*$^{KD/+}$ compared to littermate *Fgfr2*$^{F/+}$, *Fgfr2*$^{FCPG/+}$ and *Fgfr2*$^{+/+}$ controls.

(F) Acetocarmine stained preparation of exorbital lacrimal glands at P5 from *Fgfr2*$^{F/F}$, *Fgfr2*$^{FCPG/FCPG}$ and *Fgfr2*$^{KD/+}$ mice showed reduced branching and reduced overall size of the gland. *Fgfr2*$^{F/F}$, *Fgfr2*$^{FCPG/FCPG}$ and *Fgfr2*$^{KD/+}$ compared to littermate *Fgfr2*$^{F/+}$, *Fgfr2*$^{FCPG/+}$ and *Fgfr2*$^{+/+}$ controls show reduced branching and a reduction in size of the gland.

(G) Schematic representation of IRS2 protein domains with phosphorylated tyrosine residues in response to FGFR2 activation as shown by mass spectrometry (Francavilla et al., 2013). For each indicated IRS2 tyrosine, we show prospective binding partners identified by mass spectrometry.

(H) Constitutive binding of IRS2 to FGFR2^{WT} and FGFR2^{FCPG} was observed. Primary MEFs cells were obtained from E14.5 *Fgfr2*$^{+/+}$ and *Fgfr2*$^{FCPG/FCPG}$ embryos. After serum starvation overnight, cells were stimulated with FGF1 (50ng/ml) and heparin (5 μg/ml) for 5 min. IRS2 binding to FGFR2 was documented by co-immunoprecipitation experiments. No ab: No antibody against FGFR2 was added to the samples before addition of protein A-Sepharose.

Supplementary Figure S3

(A) Micro-CT analysis of control *Fgfr1*$^{cKO/+}$*; Fgfr2*$^{cKO/+}$ embryos at E18.5 compared to *Fgfr1*$^{F/cKO}$*; Fgfr2*$^{cKO/+}$ and *Fgfr1*$^{FCPG/cKO}$*; Fgfr2*$^{cKO/+}$ embryos at similar stages. The mandible (red arrow) was more severely affected in *Fgfr1*$^{FCPG/cKO}$*; Fgfr2*$^{cKO/+}$ than in *Fgfr1*$^{F/cKO}$*; Fgfr2*$^{cKO/+}$ embryos.

(B) Frontal facial view of DAPI-stained E10.5 *Fgfr1*$^{F/cKO}$*; Fgfr2*$^{cKO/+}$ embryos compared to control *Fgfr1*$^{cKO/+}$*; Fgfr2*$^{cKO/+}$ embryos. Midline separation (yellow asterix) was observed and facial prominences were hypoplastic (yellow arrow), however no defect in the mandible (red arrow) was observed.

(C) Frontal facial view of DAPI-stained E10.5 *Fgfr1*$^{FCPG/cKO}$*; Fgfr2*$^{cKO/+}$ embryos compared to control *Fgfr1*$^{cKO/+}$*; Fgfr2*$^{cKO/+}$ embryos. In the mutants, midline separation (yellow asterix) and facial prominence (yellow arrow) defects were more severe than *Fgfr1*$^{F/cKO}$*; Fgfr2*$^{cKO/+}$ embryos. A defect in the mandible (red arrow) was also more severe than *Fgfr1*$^{F/cKO}$*; Fgfr2*$^{cKO/+}$ embryos.

(D-E) Cell-death analysis by TUNEL staining in the facial prominences of (D) *Fgfr1*$^{F/cKO}$*; Fgfr2*$^{cKO/+}$ and (E) *Fgfr1*$^{FCPG/cKO}$*; Fgfr2*$^{cKO/+}$ embryos at E10.5. Compared to the *Fgfr1*$^{cKO/+}$*; Fgfr2*$^{cKO/+}$ controls, multiple dying cells were detected in both the MNP and the LNP.

(F) Frontal facial view of DAPI-stained *Fgfr1*^{F} and *Fgfr2*^{F} compound mutant embryos at E10.5. *Fgfr1*$^{F/F}$*; Fgfr2*$^{+/F}$ embryos had defect in development of facial prominences, as opposed to *Fgfr1*$^{F/+}$*; Fgfr2*$^{F/+}$ controls. Mandibular prominences were hypoplastic, however the maxillary prominences, FNP and MNP were more severely affected. *Fgfr1*$^{F/F}$*; Fgfr2*$^{+/+}$ mutants, *Fgfr1*$^{+/+}$*; Fgfr2*$^{F/F}$ mutants, and *Fgfr1*$^{F/+}$*; Fgfr2*$^{F/F}$ mutants did not show obvious defects at this stage. *Fgfr1*$^{F/F}$*; Fgfr2*$^{+/F}$ mutant embryos were also developmentally retarded. We did not recover *Fgfr1*$^{F/F}$*; Fgfr2*$^{F/F}$ mutant embryos by E9.5.

(G) Craniofacial phenotype at E10.5 of DAPI-stained *Fgfr1*^{FCPG} and *Fgfr2*^{FCPG} compound mutant embryos. We observed the posterior truncation for *Fgfr1*$^{FCPG/FCPG}$ mutant embryos. Introduction of one copy of *Fgfr2*^{FCPG} allele on a *Fgfr1*$^{FCPG/FCPG}$ background resulted in severe growth retardation of the facial prominences compared to control *Fgfr1*$^{+/FCPG}$*; Fgfr2*$^{FCPG/FCPG}$ embryos. *Fgfr2*$^{FCPG/FCPG}$ and *Fgfr1*$^{+/FCPG}$*; Fgfr2*$^{FCPG/FCPG}$ embryos did not exhibit abnormal phenotypes and were comparable to WT embryos.

Supplementary Figure S4

(A) *WT*-iFNP cells were serum starved overnight and stimulated with either 50 ng/mL FGF1 or 50 ng/mL FGF8-b and 5 µg/mL heparin for the indicated times (0-60 mins). Robust ERK1/2 activation was observed with FGF1 treatment compared to FGF8-b treatment. FGF8-b signaling output showed a small biphasic response in peak activity (first between 2 and 5 mins and then at 30 mins) which was not observed with FGF1 stimulation.

(B) We quantified *Alx4, Dlx1, Dlx5, FoxD1, Twist1* and *Lhx8* expression by quantitative real-time PCR (qRT-PCR) and found they were all expressed at similar levels in both immortalized FNP (iFNP) cells and primary FNP cells derived from wild-type embryos. Only *Msx1* expression was 1.8-fold higher in wild-type primary FNP cells compared to iFNP cell lines. These results identify iFNP cells as a suitable cell type to interrogate FGF signaling functions in craniofacial development.

(C) *Fgfr1, Fgfr3, Fgfr4* and *Fgfr2*^{WT} mRNA expression *in Fgfr2*^{F}*, Fgfr2*^{CPG} and *Fgfr2*^{FCPG} iFNP cells before and after *Fgfr1*-CRISPR, as determined by RT-qPCR.

(D-E) *Fgfr2* null *Fgfr1*^{FCPG} iFNP cells generated using CRISPR/Cas9. Upon FGF1 stimulation, we observed peak activation of pERK1/2 (D) after 2 mins in *Fgfr1*$^{FCPG/FCPG}$ iFNP cells. We did not

observe robust activation in *Fgfr2*$^{CRISPR\text{-}KO}$*; Fgfr1*^{FCPG} iFNP cells. The activation of ERK1/2 was lower than what was observed for *Fgfr1*$^{FCPG/FCPG}$ iFNP. (E) pAKT activation was undetectable in both *Fgfr2*$^{CRISPR\text{-}KO}$*; Fgfr1*^{FCPG} and *Fgfr2*$^{+/+}$*; Fgfr1*^{FCPG} iFNP cells.

Supplementary Figure S5

(A) Forward scatter plot obtained from flow sorting cells from *Fgfr1*$^{cKO/+}$*; Fgfr2*$^{cKO/+}$*; ROSA26*$^{mT/mG}$ control FNP, *Fgfr1*$^{FCPG/cKO}$*; Fgfr2*$^{cKO/+}$*; ROSA26*$^{mT/mG}$ and *Fgfr1*$^{cKO/cKO}$*; Fgfr2*$^{cKO/cKO}$*; ROSA26*$^{mT/mG}$ double mutant FNP showed relatively no differences in cell-size across different genotypes.

(B) Quantification of relative fluorescence intensity from Paxillin immunostaining in *Fgfr1*$^{cKO/+}$*; Fgfr2*$^{cKO/+}$*; ROSA26*$^{mT/mG}$ control FNP cells and *Fgfr1*$^{FCPG/cKO}$*; Fgfr2*$^{cKO/+}$*; ROSA26*$^{mT/mG}$ and *Fgfr1*$^{cKO/cKO}$*; Fgfr2*$^{cKO/cKO}$*; ROSA26*$^{mT/mG}$ double mutant FNP cells upon serum starvation and growth factor treatments shown in Figure 7C. Relative fluorescence intensity in starvation media showed a baseline level of fluorescence from paxillin accumulation. Upon serum stimulation or PDGF treatment cells from all genotypes showed robust increase in fluorescence from paxillin accumulation at the focal adhesions. Upon FGF treatment, *Fgfr1*$^{FCPG/cKO}$*; Fgfr2*$^{cKO/+}$*; ROSA26*$^{mT/mG}$ FNP cells show robust paxillin accumulation comparable to control cells, whereas *Fgfr1*$^{cKO/cKO}$*; Fgfr2*$^{cKO/cKO}$*; ROSA26*$^{mT/mG}$ double mutant FNP cells showed poor response.

(C) Western Blot analysis of freshly harvested cells from *Fgfr1*$^{cKO/+}$*; Fgfr2*$^{cKO/+}$*; ROSA26*$^{mT/mG}$ control FNP cells and *Fgfr1*$^{FCPG/cKO}$*; Fgfr2*$^{cKO/+}$*; ROSA26*$^{mT/mG}$ and *Fgfr1*$^{cKO/cKO}$*; Fgfr2*$^{cKO/cKO}$*; ROSA26*$^{mT/mG}$ double mutant FNP cells for pFAK, total FAK, β-catenin and Paxillin. GAPDH was used as a loading control. Total FAK and β-catenin levels remained constant across all genotypes. Although similar levels of pFAK and Paxillin was observed in *Fgfr1*$^{cKO/+}$*; Fgfr2*$^{cKO/+}$*; ROSA26*$^{mT/mG}$ control and *Fgfr1*$^{FCPG/cKO}$*; Fgfr2*$^{cKO/+}$*; ROSA26*$^{mT/mG}$ FNP cells, a severe reduction was observed in *Fgfr1*$^{cKO/cKO}$*; Fgfr2*$^{cKO/cKO}$*; ROSA26*$^{mT/mG}$ double mutant FNP cells.

(D) Relative expression of pFAK, Total FAK and Paxillin. Reduced levels of pFAK and paxillin was observed in *Fgfr1*$^{cKO/cKO}$*; Fgfr2*$^{cKO/cKO}$*; ROSA26*$^{mT/mG}$ double mutant FNP cells. *Fgfr1*$^{cKO/+}$*; Fgfr2*$^{cKO/+}$*; ROSA26*$^{mT/mG}$ control FNP cells and *Fgfr1*$^{FCPG/cKO}$*; Fgfr2*$^{cKO/+}$*; ROSA26*$^{mT/mG}$ cells expressed similar levels of pFAK, total FAK and paxillin.

(E) Western blot analysis was used to check if FAK activation require FGF stimulation in *Fgfr1*$^{FCPG/cKO}$*; Fgfr2*$^{cKO/+}$*; ROSA26*$^{mT/mG}$ mutant FNP cells. Freshly harvested *Fgfr1*$^{cKO/+}$*; Fgfr2*$^{cKO/+}$*; ROSA26*$^{mT/mG}$ control, *Fgfr1*$^{FCPG/cKO}$*; Fgfr2*$^{cKO/+}$*; ROSA26*$^{mT/mG}$, and *Fgfr1*$^{cKO/cKO}$*; Fgfr2*$^{cKO/cKO}$*; ROSA26*$^{mT/mG}$ double mutant FNP cells were either treated with serum or FGF1 for 15 mins before assessing levels of pFAK by western blot. *Fgfr1*$^{cKO/+}$*; Fgfr2*$^{cKO/+}$*; ROSA26*$^{mT/mG}$ control and

Fgfr1$^{FCPG/cKO}$*; Fgfr2*$^{cKO/+}$*; ROSA26*$^{mT/mG}$ FNP cells showed a comparable increase in FAK activation upon FGF stimulation. In contrast *Fgfr1*$^{cKO/cKO}$*; Fgfr2*$^{cKO/cKO}$*; ROSA26*$^{mT/mG}$ double mutant FNP cells failed to activate FAK in both serum-stimulated and FGF treated conditions.

(F) Quantification of relative fluorescence from Paxillin immunostaining in *Fgfr2*$^{WT/WT}$ (*Fgfr1*$^{CRISPR\text{-}KO}$ *Fgfr2*$^{WT/WT}$), *Fgfr2*$^{FCPG/FCPG}$ (*Fgfr1*$^{CRISPR\text{-}KO}$ *Fgfr2*$^{FCPG/FCPG}$), and *Fgfr2*$^{-/-}$ (*Fgfr1*$^{CRISPR\text{-}KO}$ *Fgfr2*$^{CRISPR\text{-}KO}$) -iFNP cells upon serum starvation and growth factor treatments shown in Figure 7C. Relative fluorescence intensity in starvation media showed a baseline level of fluorescence from paxillin accumulation. Upon serum stimulation or PDGF treatment, cells from all genotypes showed a robust increase in fluorescence from paxillin accumulation at the focal adhesions. Upon FGF treatment, *Fgfr1*$^{CRISPR\text{-}KO}$ *Fgfr2*$^{CRISPR\text{-}KO}$ double mutant iFNP cells showed poor response. In contrast, *Fgfr1*$^{CRISPR\text{-}KO}$ *Fgfr2*$^{FCPG/FCPG}$ iFNP cells showed robust paxillin accumulation comparable to control cells under these conditions.

(G) Quantification of percentage of cells that form cell boundaries in *Fgfr1*$^{cKO/+}$*; Fgfr2*$^{cKO/+}$*; ROSA26*$^{mT/mG}$ control, *Fgfr1*$^{FCPG/cKO}$*; Fgfr2*$^{cKO/+}$*; ROSA26*$^{mT/mG}$, and *Fgfr1*$^{cKO/cKO}$*; Fgfr2*$^{cKO/cKO}$*; ROSA26*$^{mT/mG}$ double mutant FNP cells. Freshly harvested *Fgfr1*$^{cKO/+}$*; Fgfr2*$^{cKO/+}$*; ROSA26*$^{mT/mG}$ control FNP cells and *Fgfr1*$^{FCPG/cKO}$*; Fgfr2*$^{cKO/+}$*; ROSA26*$^{mT/mG}$ cells were cultured in serum stimulated conditions for 3 hrs during which 60% control cells formed stable cell-cell contacts as observed by membrane GFP expression (Figure 7D). In contrast, fewer than 30% of *Fgfr1*$^{cKO/cKO}$*; Fgfr2*$^{cKO/cKO}$*; ROSA26*$^{mT/mG}$ double mutant FNP cells formed such contacts.

Tables

Table 1: Recovery of *Fgfr2* signaling mutants

Fgfr2 signaling mutant heterozygotes (*Fgfr2*$^{F/+}$, *Fgfr2*$^{C/+}$, *Fgfr2*$^{PG/+}$, *Fgfr2*$^{CPG/+}$, *Fgfr2*$^{FCPG/+}$ and *Fgfr2*$^{KD/+}$) were intercrossed. Embryos were analyzed either at E18.5 or postnatally between P4 and P10.

P4-P10	+/+	+/*	*/*
R2^{F}	110	191	85 (22%)
R2^{C}	129	245	131 (26%)
R2^{PG}	132	265	78 (16%)
R2^{CPG}	101	225	70 (18%)
R2^{FCPG}	187	357	102 (16%)
R2^{KD}	12	26	0
E18.5	+/+	+/*	*/*
R2^{F}	24	51	22 (23%)
R2^{C}	12	27	14 (26%)
R2^{PG}	16	34	14 (22%)
R2^{CPG}	8	24	10 (24%)
R2^{FCPG}	21	44	22 (25%)
R2^{KD}	18	27	0

Table 2: Recovery of *Fgfr2* hemizygous signaling mutants

To analyze *in vivo* phenotypes associated with *Fgfr2* signaling mutations, *Fgfr2* signaling mutant heterozygotes were crossed with $Fgfr2^{+/-}$ null heterozygotes. $Fgfr2^{C/-}$, $Fgfr2^{PG/-}$ and $Fgfr2^{CPG/-}$ embryos were analyzed at E18.5 and postnatally at P0 and between P4 and P10. Hemizygous $Fgfr2^{F/-}$ and $Fgfr2^{FCPG/-}$ mutant mice were recovered at expected Mendelian ratios at E18.5, but died postnatally.

P4-P10	Total	Observed	Expected
F/-	19	0	9.75
C/-	26	10	13
PG/-	23	13	11.5
CPG/-	26	12	13
FCPG/-	28	1	7
P0-P1	Total	Observed	Expected
F/-	33	4	8.75
FCPG/-	25	2	6.25
E18.5	Total	Observed	Expected
F/-	33	5	8.25
FCPG/-	31	10	7.75

Table 3: Craniofacial structures differentially affected in conditional signaling mutants, *Fgfr1*^{F} mutation versus *Fgfr1*^{FCPG}, as analyzed using Micro-CT.

Micro-CT examination of *Fgfr1*$^{F/cKO}$*; Fgfr2*$^{cKO/cKO}$ and *Fgfr1*$^{FCPG/cKO}$*; Fgfr2*$^{cKO/cKO}$ mutant mice skull were to *Fgfr1*$^{cKO/cKO}$*; Fgfr2*$^{cKO/cKO}$ mutants at E18.5. *Fgfr1*$^{FCPG/cKO}$*; Fgfr2*$^{cKO/cKO}$ mutant skull show a more severe defect than *Fgfr1*$^{F/cKO}$*; Fgfr2*$^{cKO/cKO}$ mutants. Several structures are differentially affected in *Fgfr1*$^{F/cKO}$*; Fgfr2*$^{cKO/cKO}$ and *Fgfr1*$^{FCPG/cKO}$*; Fgfr2*$^{cKO/cKO}$ mutants. Most severe defects are observed in *Fgfr1*$^{cKO/cKO}$*; Fgfr2*$^{cKO/cKO}$ mutants.

C/CPG<F<FCPG	***C/CPG<F=FCPG***
Nasal Cartilage	
Mandible	
Squamosal	
Maxilla	
	Premaxilla
	Frontal bone
	Zygomatic bone
	Tympanic bulla
	Basisphenoid
	Internal pterygoid process

STAR Methods

Detailed methods are provided in the online version of this paper and include the following:

- Key resource table
- Contact for reagent and resource sharing
- Method details
    - Generation of knock-in mice
    - Mouse strains
    - Generation of Fgfr2-Flag3x expression vector and stable 3T3 expression lines
    - Coimmunoprecipitation and Western blotting
    - Cell derivation and culture conditions
    - Skeletal preparations
    - Acetocarmine and hematoxylin and eosin staining
    - *Scratch assays*
    - *Transwell assays*
    - *Immunofluorescence and Antibodies*
    - *In situ hybridization*
    - *Micro-CT imaging*
    - *Cell proliferation assay*
    - *TUNEL assay*
    - *RT-qPCR*
- Quantification and statistical analysis

Key resource table

Reagent and resource	Source	Identifier
Antibodies		
FGFR2	Abcam	#ab109372
CRKL	Santa Cruz Biotechnology	#sc-319
FRS2	Santa Cruz Biotechnology	#sc-8318
FLAG2-M2	Sigma	#F1804
phospho-p44/42 MAPK Thr202/Tyr204	Cell Signaling Technology	#9101
p44/42 MAPK	Cell Signaling Technology	#9102
GAPDH	ProteinTech	#60004-1-Ig
phospho-AKT Ser473	Cell Signaling Technology	#4060
AKT	Cell Signaling Technology	#9272
phospho-p38	Cell signaling Technology	#4511
p38	Cell signaling Technology	#9212
phospho-PLCγ1 (Y783)	Cell Signaling Technology	#2821
PLCγ1	Cell Signaling Technology	#2822
phospho-JNK	Cell Signaling Technology	#4671
STAT3α	Cell signaling Technology	#8768
phospho-STAT3 (Y705)	Cell Signaling Technology	#9145
phospho-FAK	Cell Signaling Technology	#3283
FAK	Cell Signaling Technology	#3285
Paxillin	Abcam	#ab32084
IRS2	Cell Signaling Technology	#3089
β-catenin	Cell Signaling Technology	#8480
Neurofilament antibody	DSHB	#Clone 2H3
EOMES	Abcam	#ab23345
CDX2	Biogenex	#MU392A-UC
GFP	AvesLab	#GFP-1020
SMA	Cell Signaling Technology	#19245
Peroxidase AffiniPure Goat Anti-Mouse IgG (H+L)	Jackson ImmunoResearch Laboratories	#115-035-003

Peroxidase AffiniPure Goat Anti-Rabbit IgG (H+L)	Jackson ImmunoResearch Laboratories	#111-035-003
Donkey anti-Rabbit IgG (H+L), Alexa Fluor 488	ThermoFisher Scientific	#A-21206
Donkey anti-Rabbit IgG (H+L), Alexa Fluor 546	ThermoFisher Scientific	#A-10040
Donkey anti-Rabbit IgG (H+L), Alexa Fluor 647	ThermoFisher Scientific	#A-31573
Donkey anti-Mouse IgG (H+L), Alexa Fluor 488	ThermoFisher Scientific	#A-21202
Donkey anti- Mouse IgG (H+L), Alexa Fluor 546	ThermoFisher Scientific	#A-10036
Donkey anti- Mouse IgG (H+L), Alexa Fluor 647	ThermoFisher Scientific	#A-31571
Alexa Fluor® 488 AffiniPure Donkey Anti-Chicken IgY (IgG) (H+L)	Jackson ImmunoResearch Laboratories	#703-545-155
Recombinant proteins and chemicals		
Phalloidin-Alexa647	Invitrogen	#A22287
FGF1	Peprotech	#450-33A
FGF8b	Peprotech	#100-25 B
PDGFAA	R&D Systems	#1055-AA-050
Human Fibronectin	Millipore Sigma	#FC010
G418	Fischer Scientific	#BP6735
Puromycin	Sigma	#P8833
Heparin	Sigma	#H3149-100KU
cOmplete, EDTA-free Protease Inhibitor Cocktail	Sigma	#11836153001
DAPI	Sigma	#D9542
DMEM	Sigma (Gibco)	#D5796

Trypsin	ThermoFisher	# 25200-072
Bovine calf serum	HyClone	#SH30072.03
Fetal bovine serum	HyClone	#SH30396.03
Penicillin-streptomycin	Sigma (Gibco)	#P0781
Gelatin solution	Sigma	#G1393
Carmine stain	Sigma	#C1022
Harris Hematoxylin	Sigma	#HHS16
Eosin Y	Sigma	#17372-87-1
Paraformaldehyde (PFA)	Sigma	#818715
Pierce™ ECL Western Blotting Substrate	ThermoFisher	#32106
Immobilon Western Chemiluminescent HRP Substrate	Sigma	#WBKLS0500
Commercial Assays and Kits		
Phusion Polymerase	NEB	#M0530
ImmPACTDAB kit	VectorLabs	#SK-4105
Anti-FLAG M2 magnetic beads	Sigma	#M8823
Click-iT EdU Cell Proliferation Kit for Imaging, Alexa Fluor 647 dye	ThermoFisher Scientific	#C10340
In Situ Cell Death Detection Kit, TMR red	Roche	#12156792910
RNeasy Mini Kit	Qiagen	#74106
SuperScript IV reverse transcriptase	Thermo fisher	#18090050
PerfeCTa SYBR Green FastMix	VWR	#101414-264

Experimental models: Mice		
Fgfr2^{F}	Bred in house	This manuscript
Fgfr2^{C}	Bred in house	This manuscript
Fgfr2^{PG}	Bred in house	This manuscript
Fgfr2^{FCPG}	Bred in house	This manuscript
Fgfr2^{KD}	Bred in house	This manuscript
Meox2-Cre	Bred in house	*Gt(ROSA)26Sor$^{tm2(FLP*)Sor}$*
ROSA26^{Flpo}	Bred in house	*Meox2$^{tm1(Cre)Sor}$*
Fgfr1$^{cKO/cKO}$	Bred in house	*Fgfr1$^{tm5.1Sor}$*
Fgfr2$^{cKO/cKO}$	Bred in house	*Fgfr2$^{tm1.1Sor}$*
Fgfr1-GFP	Bred in house	*Fgfr1$^{tm12.1Sor}$*
Fgfr2-mCherry	Bred in house	*Fgfr2$^{tm2.1Sor}$*
Fgfr1^{C}	Bred in house	*Fgfr1$^{tm7.1Sor}$*
Fgfr1^{F}	Bred in house	*Fgfr1$^{tm9.1Sor}$*
Fgfr1^{CPG}	Bred in house	*Fgfr1$^{tm8.1Sor}$*
Fgfr1^{FCPG}	Bred in house	*Fgfr1$^{tm10.1Sor}$*
Wnt1-Cre	Bred in house	*Tg(Wnt1-cre)11Rth*
Wnt1-Cre2	Bred in house	*Tg(Wnt1-cre)2Sor*
Ink	Bred in house	*Cdkn2a$^{+/tm1Rdp}$*
ROSA26$^{mT/mG}$	Bred in house	*Gt(ROSA)26Sor$^{tm4(ACTB-tdTomato,-EGFP)Luo}$*
Bim	Bred in house	*Bcl2l11$^{tm1.1Ast}$*
Oligonucleotides		
Refer to TableS3 for oligonucleotides used in this study	This manuscript	NA
Software and Algorithms		
Prism6	GraphPad	https://www.graphpad.com/scientific-software/prism/
CHOPCHOP		http://chopchop.cbu.uib.no/
Excel	Microsoft	NA

Contact for reagent and resource sharing

Further information and requests for resources and reagents should be directed to the corresponding author, Philippe Soriano (philippe.soriano@mssm.edu).

Method details

Generation of knock-in mice. Four distinct targeting vectors carrying the *Fgfr2*^{F}, *Fgfr2*^{C}, *Fgfr2*^{PG}, and *Fgfr2*^{KD} mutations were generated. The *Fgfr2*^{F} targeting vector was generated by cloning a short homology arm (1.7kb region between exon 9-10) and a long homology arm (5.1kb, spanning exon10) into PGKneolox2DTA.2 (Hoch and Soriano, 2006). To allow recombineering into SW105 bacteria, the neo cassette was subsequently replaced by PGKEm7neo flanked by FRT sites, which contains both a eukaryotic and a prokaryotic promoter. Similarly, for the *Fgfr2*^{C} targeting vector, we cloned a long homology arm (5.3kb region spanning exon11) and a short homology arm (1.7kb region between exon 11-12) into PGKneolox2DTA.2 and used a PGKEm7neo flanked by both FRT and LoxP sites for recombineering. For the *Fgfr2*^{PG} targeting vector, we cloned a short homology arm (1.9kb region 5' of exon19) and a long homology arm (5.4kb spanning exon19 and 3'-UTR) into PGKneolox2DTA.2 and used a PGKEm7neo flanked by FRT sites for recombineering. For *Fgfr2*^{KD} targeting vector, we cloned short homology arm (1.9kb SmaI to MfeI, spanning exon 12) and a 3.7kb long homology arm (MfeI to BclI, spanning exon 13) into PGKneolox2DTA.2 (Hoch and Soriano, 2006). Details of regions corresponding to homology arms are provided in Table S1.

For all four alleles, site-directed mutagenesis (SDM) was performed using Phusion polymerase. Nucleotide substitutions introduced by SDM in exon10 for *Fgfr2*^{F} allele (introduces an XmaI site), exon11 for *Fgfr2*^{C} allele (introduces a SacI site), exon 19 for *Fgfr2*^{PG} allele (introduces an EcoRI site) and in exon12 for *Fgfr2*^{KD} allele (introduces an AluI site) are provided below. All introduced mutations were verified by sequencing. Details of nucleotide substitutions in *Fgfr2* signaling mutations are provided in Table S2.

The targeting vectors for *Fgfr2*^{F} (linearized with NotI), *Fgfr2*^{C} (linearized with XhoI), *Fgfr2*^{PG} (linearized with NotI) and *Fgfr2*^{KD} (linearized with NotI) were electroporated into 129S4 AK7 ES cells. For generating the allelic series of signaling mutations, ES cells were targeted first with the C targeting vector generating *Fgfr2*$^{+/C}$ mutant cells. After verifying for correct targeting events, the neo cassette was removed by transient transfection with PGKCrebpA, leaving a single LoxP site behind (Figure 3C). *Fgfr2*$^{+/C}$ ES cells were then targeted using the PG targeting vector generating either *Fgfr2*$^{+/PG}$ or *Fgfr2*$^{+/CPG}$ mutant cells, as determined by breeding of the chimeras to

ROSA26^{Flpo} mice (Raymond and Soriano, 2010). After verifying for correct targeting events, the neo cassette was removed by transient transfection with PGKFlpobpA (Raymond and Soriano, 2007), leaving both an FRT site and a LoxP site behind (Figure 3C). *Fgfr2*$^{+/CPG}$ neo^{-} ES cells were finally targeted with the F targeting vector, resulting in *Fgfr2*$^{+/F}$ or *Fgfr2*$^{+/FCPG}$ mutant ES cells, as determined by breeding. After verifying for correct targeting events, the neo cassette was removed by transient transfection with Flpe, which is less efficient than Flpo in ES cells (Raymond and Soriano, 2007), in order to not recombine sequences between exons 10-18 due to the retention of the FRT site during the generation of the *Fgfr2*^{PG} allele. We screened targeting events initially by PCR coupled with restriction digestion to identify incorporation of nucleotide substitutions. Proper targeting was confirmed by Southern blotting using 5′ external and 3′ external probes amplified using the following primer pairs and then an internal probe against Neo. Primers used to generate probes for confirming targeted clones using Southern blots are described in Table S3.

ES cell chimeras were bred to *Meox2-Cre* or *ROSA26Flpo* deleter mice (Raymond and Soriano, 2010; Tallquist and Soriano, 2000) maintained on a 129S4 genetic background to remove the neomycin selection cassette and the deleter alleles were subsequently crossed out. Two independent mouse lines were generated from independent ES cell clones for each allele, and phenotypes were confirmed in both lines. The *Fgfr2*^{C}, *Fgfr2*^{PG}, *Fgfr2*^{F}, *Fgfr2*^{FCPG} and *Fgfr2*^{KD} alleles were maintained on the 129S4 genetic background. *Fgfr2*^{C}, *Fgfr2*^{PG}, *Fgfr2*^{F} and *Fgfr2*^{KD} mice were genotyped using oligonucleotides listed in Table S3, with the F, C or PG primers all being able to genotype *Fgfr2*^{FCPG} mice.

Mouse strains. All animal experimentation was conducted according to protocols approved by the Institutional Animal Care and Use Committee of the Icahn School of Medicine at Mount Sinai. *Fgfr1*$^{cKO/cKO}$, *Fgfr2*$^{cKO/cKO}$, *Fgfr1-GFP* and *Fgfr2-mCherry* were previously described (Hoch and Soriano, 2006; Molotkov et al., 2017). *Fgfr1* signaling mutations (Brewer et al., 2015) are referred to as *Fgfr1*^{C}, *Fgfr1*^{F}, *Fgfr1*^{CPG} and *Fgfr1*^{FCPG}. *Tg(Wnt1-cre)11Rth*, *Tg(Wnt1-cre)2Sor*, *Cdkn2a*$^{+/tm1Rdp}$, *Gt(ROSA)26Sor*$^{tm4(ACTB-tdTomato,-EGFP)Luo}$, and *Bcl2l11*$^{tm1.1Ast}$ are referred to in the text as *Wnt1-Cre*, *Wnt1-Cre2*, *Ink, ROSA26*$^{mT/mG}$, and *Bim* respectively (Bouillet et al., 1999; Danielian et al., 1998; Lewis et al., 2013; Muzumdar et al., 2007; Serrano et al., 1996). All lines were maintained on a 129S4 co-isogenic background, except for *Bim* which was crossed into the *Fgfr1/2* deficient backgrounds after only six generations of backcrossing to 129S4.

***Generation of Fgfr2$^{-Flag3x}$ expression vector* and stable 3T3 expression lines.** An *Fgfr2* isoform "c" cDNA isoform was PCR amplified from primary MEFs derived from *Fgfr2*$^{+/+}$, *Fgfr2*$^{PG/PG}$, *Fgfr2*$^{CPG/CPG}$, *Fgfr2*$^{F/F}$ and *Fgfr2*^{FCPGFCPG} and subsequently digested with HindIII and XhoI. The fragments were cloned in the pcDNA expression vector and sequence verified. Linearized pcDNA-FGFR2 plasmids were transfected in 3T3 cells cultured in DMEM supplemented with 10% calf serum (HyClone Laboratories) with 50 U/mL each penicillin and streptomycin. Stable clones were selected in 500 μg/mL G418. 10 clones from each construct (FGFR2^{wt}-, FGFR2^{PG}-, FGFR2^{CPG}-, FGFR2^{F}-, or FGFR2^{FCPG}-Flag3x) were expanded and assessed for FLAG expression by western blot. Clones expressing high FGFR2-FLAG levels were selected for further analysis.

Coimmunoprecipitation and Western blotting. Stable 3T3 cells expressing FGFR2^{WT}, FGFR2^{PG}, FGFR2^{CPG}, FGFR2^{F}, or FGFR2^{FCPG} -Flag3x were serum-starved (0.1% calf serum supplemented DMEM) overnight, stimulated for 15 mins with 50 ng/mL FGF1 (PeproTech, 450-33A) or FGF8b (PeproTech 100-25B) and 5 μg/mL heparin, and lysed in ice-cold NP-40 lysis buffer (20 mM Tris HCL at pH 8, 137 mM NaCl, 10% glycerol, 1% Nonidet [NP-40], 2 mM EDTA, 25 mM β glycerol phosphate, 1 mM Na_3VO_4, 10 mM NaF, 1× cOmplete, EDTA-free Protease Inhibitor Cocktail. 800 μg cell lysates were subsequently used for immunoprecipitation with Anti-FLAG M2 magnetic beads using the manufacturer's protocol. We incubated lysates with anti-FLAG M2 magnetic beads overnight at 4°C followed by five washes with lysis buffer, and precipitated proteins were eluted in Laemmli buffer (10% glycerol, 2% SDS, 0.002% bromophenol blue, 0.062M Tris-HCl, pH 6.8) containing 10% β-mercaptoethanol, heated for 5 min at 95°C, separated by SDS-PAGE and analyzed by western blots.

Western blot analysis was performed according to standard protocols using horseradish peroxidase-conjugated secondary antibodies (1:10,000 dilution) developed by chemiluminescent HRP substrate. Primary antibodies were used at the following dilutions for Western blotting: FGFR2 (1:500 dilution), CRKL (1:500 dilution), FRS2 (1:500 dilution), Flag2 M2 (1:500 dilution), phospho-p44/42 MAPK (1:1,000 dilution), p44/42 MAPK (1:1,000 dilution), GAPDH (1:1000 dilution), phospho-AKT (1:1,000 dilution), AKT (1:1,000 dilution), phospho-p38 (1:500 dilution), p38 (1:500 dilution), phospho-PLCγ1 (Y783) (1:200 dilution), PLCγ1 (1:1000 dilution), pJNK (1:500 dilution), STAT3α (1:1000 dilution), phospho-FAK (1:1000 dilution), FAK (1:1000 dilution), β-catenin (1:1000 dilution), Paxillin (1:1000 dilution), and IRS2 (Cell Signaling Technology, 3089).

Cell derivation and culture conditions. Primary iFNPs were generated by dissecting the maxillary and nasal prominences of E11.5 *Fgfr2*$^{+/+}$*; Ink*$^{-/-}$, *Fgfr2*$^{F/F}$*; Ink*$^{-/-}$, *Fgfr2*$^{CPG/CPG}$*; Ink*$^{-/-}$, and

E9.5 or E11.5 *Fgfr2*$^{FCPG/FCPG}$*; Ink*$^{-/-}$ embryos in PBS. The tissue was disassociated with 0.125% Trypsin-EDTA and cultured in DMEM supplemented with 20% FBS, 50 U/mL each penicillin and streptomycin on fibronectin coated plates (0.5μg/cm^2). Cells were subsequently split 1:5 through for at least 5 passages before immortalized cell lines were obtained. Cells were allowed to grow until sub-confluent. All experiments were performed between passage 15 and 25. We used PX459 V2.0 vector (Addgene plasmid # 62988) to CRISPR out either *Fgfr1* or *Fgfr2* and create *Fgfr1* null, *Fgfr2* null, or *Fgfr1*: *Fgfr2* double null cells. gRNA sequences for *Fgfr1* and *Fgfr2* were selected using CHOPCHOP gRNA design web tool and were cloned using the oligonucleotides (Table S3), as previously described (Ran et al., 2013). Plasmids were transfected in respective iFNP cells cultured in DMEM supplemented with 10% calf serum with 50 U/mL each penicillin and streptomycin. Stable clones were selected in 5 μg/mL Puromycin. Clones were verified (homozygous deletion of exon6 for *Fgfr1* and deletion exon5 for *Fgfr2* which also introduces a frameshift mutation) using PCR (Table S3). Primary MEFs were derived from E12.5 wild type mice embryos. Embryos were eviscerated and after removing the head, remaining tissue was chopped into 1 cm pieces and incubated in 1 mL trypsin-EDTA (0.25%) for 30 mins with intermittent shaking. 10 mL DMEM 10% calf serum was added and the mixture was allowed to pass through a cell-strainer. Cells collected from each embryo was plated in 0.2% gelatin coated 15cm plate.

Skeletal preparations. Embryos at E14.5, E16.5 or E18.5 embryos were skinned, eviscerated, fixed in 95% ethanol overnight, and stained (0.015% Alcian blue, 0.005% Alizarin red, 5% glacial acetic acid, in 70% ethanol) overnight at 37°C. Skeletons were then cleared in 1% KOH and transferred to decreasing concentrations of KOH in increasing concentrations of glycerol until clear.

Acetocarmine and hematoxylin and eosin staining. Freshly harvested tissue was fixed in 4% PFA at 4°C overnight followed by dehydration in 70% ethanol. For acetocarmine staining, tissues were incubated in 0.5% aceto-carmine (0.5 g carmine stain dissolved in 100 ml boiling 45% acetic acid for 15 minutes), followed by de-staining in 70% ethanol for 1 minute and 1% acid alcohol (1% HCl in 70% ethanol) for 2 minutes and 5% acid alcohol (5% HCl in 70% ethanol) for 1 minute. For hematoxylin and eosin staining, freshly harvested tissues were dissected in PBS, and fixed in 4% PFA followed by dehydration through a graded ethanol series, and embedded in paraffin. 5μm sections were cut. After deparaffinization and rehydration, sections were stained with Harris modified hematoxylin followed by a 10 second wash in acid-alcohol (1% v/v HCl in 70% EtOH),

followed by counterstaining with 1% eosinY. Tissues were washed and mounted with Permount (Thermo Fisher Scientific).

Scratch assays. Cells were seeded onto glass coverslips coated with 5 µg/mL human plasma fibronectin purified protein. At ~90–100% confluency, cells were scratched with a P1000 pipet tip, washed with PBS and incubated in fresh medium containing either 0.1% FBS, 10% FBS, 50 ng/mL FGF1 and 5 µg/mL heparin or 10 ng/mL PDGF-AA supplemented DMEM for 12 hrs.

Transwell assays. All cells were serum-starved for 24 hrs in 0.1% FBS supplemented DMEM prior to migration. Cell culture inserts compatible for 24-well plates containing polyethylene terephthalate membranes with 8 µm pores (Corning Inc., Corning, NY, USA) were coated with 5 µg/mL human plasma fibronectin purified protein. 100,000 cells were loaded in each insert in 250 µL medium containing 0.1% FBS and inserts were immersed in 500 µL medium containing either 10% FBS, 50 ng/mL FGF1 and 5 µg/mL heparin or 10 ng/mL PDGF-AA for 10 hr. Migrated cells were subsequently fixed in 4% PFA in PBS for 10 min and stained in 0.1% crystal violet in 10% ethanol for 10 min. Dried inserts were photographed using an Axiocam 105 color camera fitted onto a Stemi 508 stereo microscope (Carl Zeiss Microscopy, LLC). Five fields of cells from each of three independent trials were photographed and quantified.

Immunofluorescence and Antibodies. For immunostaining whole mount embryos were fixed in 4% paraformaldehyde solution (PFA) in PBS overnight and washed with PBS five times, permeabilized with 0.5% Triton X100 in PBS for 30 min and blocked in 2% donkey serum for 2h at room temperature. Primary anti-neurofilament antibody (Clone 2H3, DSHB) was used at a 1:20 dilution in 1% donkey serum in PBST; embryos were incubated overnight at 4°C. The next day, embryos were washed 4 times in PBST and incubated with anti-mouse HRP-conjugated secondary antibodies at a 1:1000 dilution for 4hrs at room temperature followed by washing in PBST 4 times and signal was developed using ImmPACTDAB kit. For whole-mount immunofluorescence at E7.5, embryos were fixed overnight in 4:1 methanol:DMSO. Primary antibodies for Eomes (1:100 dilution) and Cdx2 (1:100 dilution) were used. For immunostaining cells, cells were fixed for 10 mins in 4% PFA in PBS at room temperature. Cells/ tissues were subsequently processed for immunofluorescence analysis as detailed above using anti-paxillin primary antibody (1:250 dilution) with Alexa647 conjugated phalloidin (1:40 dilution). For immunofluorescence on sections, antibodies for GFP (1:100 dilution), mCherry (1:100 dilution) and SMA (1:100 dilution) was used. Embryos were stained with DAPI following fixation as previously described (Sandell et al., 2012). Cells / tissues were photographed using an Olympus

DP71 digital camera fitted onto an Olympus BX51 fluorescence microscope, Leica SP5 confocal or a Hamamatsu C11440 camera fitted to a Zeiss Observer Z1 microscope. Epifluorescence was imaged in Zeiss Axioplan fitted to ProgRes CT3 camera.

In situ hybridization. Labeled antisense-RNA probes were synthesized for *Alx3, Msx1, Six3, Nkx2.1, Fgf8, Shh, Col2a1, Col10a1* and *Meox1*. Digoxigenin-labeled anti-sense probes were generated as described, and mRNA in situ hybridization on paraffin sections for chromogenic detection was performed using standard protocols.

***Micro-CT imaging*.** Micro-CT imaging of the skulls were performed using a SkyScan 1172 scanner (Bruker, Kontich, Belgium). The mouse heads were dissected and fixed in 10% neutral buffered formalin and washed and stored in PBS at 4 °C. The skull bones were scanned with settings of 50 kV, 500 µA, 10 µm pixel resolution, 0.3° rotation steps, and 4 frames average imaging with a 0.5-mm Al filter at Micro-CT Core, School of Dentistry, NYU, New York. The acquired X-ray projections were reconstructed using the Imirus software (Oxford Instruments).

***Cell proliferation assay*.** For EdU labeling in mice, pregnant females were injected intraperitoneally with 100 mg/kg body weight of EdU. EdU detection was carried out as per manufacturer's instruction for Click-iT EdU Cell Proliferation Kit.

TUNEL assay. Sections were deparaffinized and were rehydrated in PBS, followed by post-fixation in 4% PFA. In Situ Cell Death Detection Kit, TMR red user protocol was used to detect cell death.

***RT-qPCR*.** Cells were lysed, and mRNA was extracted according to Qiagen RNeasy kit standard protocol. cDNA was synthesized using a 2:1 ratio of random primers to Oligo(dT) with SuperScript IV RT (Invitrogen). qPCR was performed with PerfeCTa SYBR Green FastMix for iQ (Quanta Biosciences) with Bio-Rad iQ5 multicolor real-time PCR detection system and analyzed with Bio-Rad iQ5 optical system software (version 2.0). Cycling conditions were as follows: step 1, 3 min at 95°C; step 2, 10 sec at 95°C; step 3, 30 sec at 60°C; and repeat steps 2 and 3 for 40 cycles. Proper amplification was confirmed using a melting curve and by running samples on a gel to ensure that the correct size band was obtained. Graphs were made using Microsoft Excel and Prism. Primer sequence for respective genes used for RT-qPCR analysis is listed below.

Quantification and statistical analysis. Statistical analysis was performed using GraphPad Prism6.0 and Microsoft Excel. Values are presented as mean ± s.e.m.

.

Table S1: Homology arms used in targeting vectors

	Short homology arm (corresponding primer binding region)	Notes	Long homology arm (corresponding primer binding region)	Notes
Fgfr2^{F}	GCTCTTTCTCTCTATGGGTT and ATTCGACTGTAATGGGGGAC	1.7kb region between exon 9-10	TGGTATCAGCTGCTCACTGG and GCCCACCCTGAATAACCATG	5.1kb spanning exon10
Fgfr2^{C}	CTTTCTGCATCAAAGACACA and GGTTACATCGATTGCCCAGT	1.7kb region between exon 11-12	GGCCACAATTCAGAGGGAAG and AGCCCATTTTTCCACCTTCT	5.1kb spanning exon11
Fgfr2^{PG}	TCTTGGCTGTGGCTTGTACTGG and AGGACCTCGGTGACCCACTA	1.9kb region between exon 18-19	GTAGCAGAGTGGGCAAGCTC and AGGAACTGCAAGAGGACCAA	5.4kb spanning exon19 and 3'-UTR
Fgfr2^{KD}	GGTACCCAAGTGTGGAAAAT and GTTTGCTCCTTTTTGGCTTC	SmaI to MfeI, 1.9kb spanning exon12	GAACTGATGCAGAATCCCAG and CCATTVTAAGTCCCTTGAGC	MfeI to BclI 3.7kb spanning exon13

Table S2: Nucleotide substitution in signaling mutations for *Fgfr2*

Mutation	Nucleotide substitution	Amino acid substitution	Notes
F	CTG to GCC AGA to GCA	L424A R426A	Introduces an XmaI site
C	TAT to TTT TTG to CTC	Y466F L468L	Introduces a SacI site
PG	TAC to TTC TAT to TTT	Y769F Y779F	Introduces an EcoRI site
KD	GAAG to AGCT	K517A	Introduces an AluI site

Table S3: List of oligonucleotides used in this study

Gene	Forward	Purpose
Fgfr2^{F} 5' probe F	ACACTGGAGGATGGTGAAGG	Probes for Southern blot
Fgfr2^{F} 5' probe R	GACATGCATGCAATTGAACA	Probes for Southern blot
Fgfr2^{F} 3' probe F	GTCCCAGCTCAGCAATAAGC	Probes for Southern blot
Fgfr2^{F} 3' probe R	AGTGGTCACCTTCGGAGAGA	Probes for Southern blot
Fgfr2^{C} 5' probe F	GTGGGACAGCCTGGTAGGTA	Probes for Southern blot
Fgfr2^{C} 5' probe R	CGGGTAGGCTATGCACTCAT	Probes for Southern blot
Fgfr2^{C} 3' probe F	ATACTTGACCTGGCGGTTGA	Probes for Southern blot
Fgfr2^{C} 3' probe R	GGCATTTATAGCGTGGCATT	Probes for Southern blot
Fgfr2^{PG} 5' probe F	GTGTGAATGCTGCTTGTGCT	Probes for Southern blot
Fgfr2^{PG} 5' probe R	GCGGAAGCCTTGTTTTATGA	Probes for Southern blot
Fgfr2^{PG} 3' probe F	GGCCACGGAGTAGTTCAGAG	Probes for Southern blot
Fgfr2^{PG} 3' probe R	GCAAGCACATTTGTTTACCTG	Probes for Southern blot
Fgfr2^{KD} 5' probe F	TGGGTATGGCCAGCTCTAGT	Probes for Southern blot
Fgfr2^{KD} 5' probe R	TGCACACGAACCCAGCTATT	Probes for Southern blot
Fgfr2^{KD} 3' probe F	ATCCGTGCCTTTCTGAGTGG	Probes for Southern blot
Fgfr2^{KD} 3' probe R	TGCCAGCCATTTACCTCAGG	Probes for Southern blot
Fgfr2^{C}Forward-Genotyping	GTAAGTACTCTCCCTCTGGG	Genotyping
Fgfr2^{C}Reverse-Genotyping	AGCTGGCCATACCCAGACTTG	Genotyping
Fgfr2^{PG}Forward-Genotyping	CTGTTGCTTACTCTGGAGCT	Genotyping
Fgfr2^{PG}Reverse-Genotyping	GATACCCCAACTCCATTCAC	Genotyping
Fgfr2^{F}Forward-Genotyping	GGACCATATGAAGGGACTTG	Genotyping
Fgfr2^{F}Reverse-Genotyping	CTCGGTTTATCACTACAGCC	Genotyping
Fgfr2^{KD}Forward-Genotyping	ATAGCCTGCGTGTGTATCGG	Genotyping*
Fgfr2^{KD}Reverse-Genotyping	CGTCCCTGCAGAGTTCACAT	Genotyping*
Alx4-forward	ACACATGGGCAGCCTGTTTG	RT-PCR
Alx4-reverse	TGCTTGAGGTCTTGCGGTCT	RT-PCR
Gapdh-forward	AGGTCGGTGTGAACGGATTTG	RT-PCR
Gapdh-reverse	TGTAGACCATGTAGTTGAGGTCA	RT-PCR
Dlx5-forward	CAGAAGAGTCCCAAGCATCC	RT-PCR

Dlx5-reverse	GGTGACTGTGGCGAGTTA	RT-PCR
Lhx8-forward	ATGTATTGGAAGAGCGATCAG	RT-PCR
Lhx8-reverse	TCATTGGATGGGGTAACAAGGGC	RT-PCR
FoxD1-forward	TGAGCACTGAGATGTCCGATG	RT-PCR
FoxD1-reverse	CACCACGTCGATGTCTGTTTC	RT-PCR
Twist2-forward	AGCGCCCAGAGCTTCGAGGA	RT-PCR
Twist2-reverse	CGGCGAAGGCCTCGTTCAGG	RT-PCR
Msx1-forward	TCTCGGCCATTTCTCAGTCG	RT-PCR
Msx1-reverse	AGAGCATCTTCTGGCAGCTTG	RT-PCR
Sox9-forward	AGGAAGTCGGTGAAGAACGG	RT-PCR
Sox9-reverse	TGGAAGGTGAATTTCTCTGGG	RT-PCR
Dlx1-forward	TGGAATCCGAACTCCTCATC	RT-PCR
Dlx1-reverse	TGCTGCATAGCTTCTTGGTG	RT-PCR
Fgfr1-forward	CACATCGAGGTGAACGGGAGTAAG	RT-PCR
Fgfr1-reverse	CGCATCCTCAAAGGAGACATTCC	RT-PCR
Fgfr2-forward	GATGTGGAGTTTGTCTGCAAGGTTT	RT-PCR
Fgfr2-reverse	GACTGGTTGGCCTGCCCTATATAAT	RT-PCR
Fgfr3-forward	TGCGGTGCCTTCACAGA	RT-PCR
Fgfr3-reverse	ACTTGGACCTCTCCGTG	RT-PCR
Fgfr4-forward	GTACCCTCGGACCGCGGCACATAC	RT-PCR
Fgfr4-reverse	GCCGAAGCTGCTGCCGTTGATG	RT-PCR
Fgfr1-Ex6 -Crispr	CACCGCTGTTAGCCACACAAAGCAC	CRISPR Fgfr1
Fgfr1-Ex6 -Crispr	AAACGTGCTTTGTGTGGCTAACAGc	CRISPR Fgfr1
Fgfr1-Ex6 -Crispr	CACCGAAGAAGGAAGAAGGGGGAGG	CRISPR Fgfr1
Fgfr1-Ex6 -Crispr	AAACCCTCCCCCTTCTTCCTTCTTc	CRISPR Fgfr1
Fgfr2-Ex5 -Crispr	CACCGCTTCCTGGGCATTTGAACCC	CRISPR Fgfr2
Fgfr2-Ex5 -Crispr	AAACGGGTTCAAATGCCCAGGAAGc	CRISPR Fgfr2
Fgfr2-Ex5 -Crispr	CACCGCCATAAGATGTCATCTGAGA	CRISPR Fgfr2
Fgfr2-Ex5 -Crispr	AAACTCTCAGATGACATCTTATGGc	CRISPR Fgfr2
Fgfr1-CRISPR-Screen	TGCAGGAAGGATTCTGAGTGT	Screening Fgfr1 CRISPR clones
Fgfr1-CRISPR-Screen	GCTGTCTGGGCTAAAGTCTG	Screening Fgfr1 CRISPR clones

Fgfr2-CRISPR-Screen	CCCAAGCCCATAAAACCTGG	Screening Fgfr2 CRISPR clones
Fgfr2-CRISPR-Screen	CAAGGACACACGTTCACAGG	Screening Fgfr2 CRISPR clones

* Note: Genotyping *Fgfr2*^{KD} is followed by AluI digestion after PCR (Table S4)

Table S4: Details of genotyping reactions to identify *Fgfr2* signaling mutations

	WT	Mutant
Fgfr2^{C}	553 bp	655 bp
Fgfr2^{PG}	377 bp	611 bp
Fgfr2^{F}	379 bp	614 bp
Fgfr2^{KD}	350 bp After AluI digest	300 bp After AluI digest

References

Bellot, F., Crumley, G., Kaplow, J.M., Schlessinger, J., Jaye, M., and Dionne, C.A. (1991). Ligand-induced transphosphorylation between different FGF receptors. EMBO J *10*, 2849-2854.

Bouillet, P., Metcalf, D., Huang, D.C., Tarlinton, D.M., Kay, T.W., Kontgen, F., Adams, J.M., and Strasser, A. (1999). Proapoptotic Bcl-2 relative Bim required for certain apoptotic responses, leukocyte homeostasis, and to preclude autoimmunity. Science *286*, 1735-1738.

Brewer, J.R., Mazot, P., and Soriano, P. (2016). Genetic insights into the mechanisms of Fgf signaling. Genes Dev *30*, 751-771.

Brewer, J.R., Molotkov, A., Mazot, P., Hoch, R.V., and Soriano, P. (2015). Fgfr1 regulates development through the combinatorial use of signaling proteins. Genes Dev *29*, 1863-1874.

Bronner, M.E., and LeDouarin, N.M. (2012). Development and evolution of the neural crest: an overview. Dev Biol *366*, 2-9.

Browaeys-Poly, E., Blanquart, C., Perdereau, D., Antoine, A.F., Goenaga, D., Luzy, J.P., Chen, H., Garbay, C., Issad, T., Cailliau, K*., et al.* (2010). Grb14 inhibits FGF receptor signaling through the regulation of PLCgamma recruitment and activation. FEBS Lett *584*, 4383-4388.

Ceridono, M., Belleudi, F., Ceccarelli, S., and Torrisi, M.R. (2005). Tyrosine 769 of the keratinocyte growth factor receptor is required for receptor signaling but not endocytosis. Biochem Biophys Res Commun *327*, 523-532.

Chen, Z., Oh, D., Dubey, A.K., Yao, M., Yang, B., Groves, J.T., and Sheetz, M. (2018). EGFR family and Src family kinase interactions: mechanics matters? Curr Opin Cell Biol *51*, 97-102.

Chipuk, J.E., and Green, D.R. (2008). How do BCL-2 proteins induce mitochondrial outer membrane permeabilization? Trends Cell Biol *18*, 157-164.

Ciruna, B., and Rossant, J. (2001). FGF signaling regulates mesoderm cell fate specification and morphogenetic movement at the primitive streak. Dev Cell *1*, 37-49.

Ciruna, B.G., Schwartz, L., Harpal, K., Yamaguchi, T.P., and Rossant, J. (1997). Chimeric analysis of fibroblast growth factor receptor-1 (Fgfr1) function: a role for FGFR1 in morphogenetic movement through the primitive streak. Development *124*, 2829-2841.

Clybouw, C., Merino, D., Nebl, T., Masson, F., Robati, M., O'Reilly, L., Hubner, A., Davis, R.J., Strasser, A., and Bouillet, P. (2012). Alternative splicing of Bim and Erk-mediated Bim(EL) phosphorylation are dispensable for hematopoietic homeostasis in vivo. Cell Death Differ *19*, 1060-1068.

Corson, L.B., Yamanaka, Y., Lai, K.M., and Rossant, J. (2003). Spatial and temporal patterns of ERK signaling during mouse embryogenesis. Development *130*, 4527-4537.

Czabotar, P.E., Lessene, G., Strasser, A., and Adams, J.M. (2014). Control of apoptosis by the BCL-2 protein family: implications for physiology and therapy. Nat Rev Mol Cell Biol *15*, 49-63.

Danielian, P.S., Muccino, D., Rowitch, D.H., Michael, S.K., and McMahon, A.P. (1998). Modification of gene activity in mouse embryos in utero by a tamoxifen-inducible form of Cre recombinase. Curr Biol *8*, 1323-1326.

De Moerlooze, L., Spencer-Dene, B., Revest, J.M., Hajihosseini, M., Rosewell, I., and Dickson, C. (2000). An important role for the IIIb isoform of fibroblast growth factor receptor 2 (FGFR2) in mesenchymal-epithelial signalling during mouse organogenesis. Development *127*, 483-492.

Deng, C.X., Wynshaw-Boris, A., Shen, M.M., Daugherty, C., Ornitz, D.M., and Leder, P. (1994). Murine FGFR-1 is required for early postimplantation growth and axial organization. Genes Dev *8*, 3045-3057.

Dudka, A.A., Sweet, S.M., and Heath, J.K. (2010). Signal transducers and activators of transcription-3 binding to the fibroblast growth factor receptor is activated by receptor amplification. Cancer Res *70*, 3391-3401.

Endo, Y., Ishiwata-Endo, H., and Yamada, K.M. (2012). Extracellular matrix protein anosmin promotes neural crest formation and regulates FGF, BMP, and WNT activities. Dev Cell *23*, 305-316.

Eswarakumar, V.P., Ozcan, F., Lew, E.D., Bae, J.H., Tome, F., Booth, C.J., Adams, D.J., Lax, I., and Schlessinger, J. (2006). Attenuation of signaling pathways stimulated by pathologically activated FGF-receptor 2 mutants prevents craniosynostosis. Proc Natl Acad Sci U S A *103*, 18603-18608.

Fantauzzo, K.A., and Soriano, P. (2016). PDGFRbeta regulates craniofacial development through homodimers and functional heterodimers with PDGFRalpha. Genes Dev *30*, 2443-2458.

Fantauzzo, K.A., and Soriano , P. (2017). Generation of an Immortalized Mouse Embryonic Palatal Mesenchyme Cell Line. PLoS ONE *12*, e0179078.

Francavilla, C., Rigbolt, K.T., Emdal, K.B., Carraro, G., Vernet, E., Bekker-Jensen, D.B., Streicher, W., Wikstrom, M., Sundstrom, M., Bellusci, S*., et al.* (2013). Functional proteomics defines the molecular switch underlying FGF receptor trafficking and cellular outputs. Mol Cell *51*, 707-722.

Frisch, S.M., and Francis, H. (1994). Disruption of epithelial cell-matrix interactions induces apoptosis. J Cell Biol *124*, 619-626.

Garg, A., Bansal, M., Gotoh, N., Feng, G.S., Zhong, J., Wang, F., Kariminejad, A., Brooks, S., and Zhang, X. (2017). Alx4 relays sequential FGF signaling to induce lacrimal gland morphogenesis. PLoS Genet *13*, e1007047.

Geiger, B., and Yamada, K.M. (2011). Molecular architecture and function of matrix adhesions. Cold Spring Harb Perspect Biol *3*.

Gotoh, N., Ito, M., Yamamoto, S., Yoshino, I., Song, N., Wang, Y., Lax, I., Schlessinger, J., Shibuya, M., and Lang, R.A. (2004). Tyrosine phosphorylation sites on FRS2alpha responsible for Shp2 recruitment are critical for induction of lens and retina. Proc Natl Acad Sci U S A *101*, 17144-17149.

Grabow, S., Kueh, A.J., Ke, F., Vanyai, H.K., Sheikh, B.N., Dengler, M.A., Chiang, W., Eccles, S., Smyth, I.M., Jones, L.K*., et al.* (2018). Subtle Changes in the Levels of BCL-2 Proteins Cause Severe Craniofacial Abnormalities. Cell Rep *24*, 3285-3295 e3284.

Griffin, J.N., Compagnucci, C., Hu, D., Fish, J., Klein, O., Marcucio, R., and Depew, M.J. (2013). Fgf8 dosage determines midfacial integration and polarity within the nasal and optic capsules. Dev Biol *374*, 185-197.

Hadari, Y.R., Gotoh, N., Kouhara, H., Lax, I., and Schlessinger, J. (2001). Critical role for the docking-protein FRS2 alpha in FGF receptor-mediated signal transduction pathways. Proc Natl Acad Sci U S A *98*, 8578-8583.

Hanks, S.K., Quinn, A.M., and Hunter, T. (1988). The protein kinase family: conserved features and deduced phylogeny of the catalytic domains. Science *241*, 42-52.

Hoch, R.V., and Soriano, P. (2006). Context-specific requirements for Fgfr1 signaling through Frs2 and Frs3 during mouse development. Development *133*, 663-673.

Hosokawa, R., Deng, X., Takamori, K., Xu, X., Urata, M., Bringas, P., Jr., and Chai, Y. (2009). Epithelial-specific requirement of FGFR2 signaling during tooth and palate development. J Exp Zool B Mol Dev Evol *312B*, 343-350.

Inaba, T., Tanaka, Y., Tamaki, S., Ito, T., Ntambi, J.M., and Tsubota, K. (2018). Compensatory increases in tear volume and mucin levels associated with meibomian gland dysfunction caused by stearoyl-CoA desaturase-1 deficiency. Sci Rep *8*, 3358.

Kang, M., Garg, V., and Hadjantonakis, A.K. (2017). Lineage Establishment and Progression within the Inner Cell Mass of the Mouse Blastocyst Requires FGFR1 and FGFR2. Dev Cell *41*, 496-510 e495.

Karuppaiah, K., Yu, K., Lim, J., Chen, J., Smith, C., Long, F., and Ornitz, D.M. (2016). FGF signaling in the osteoprogenitor lineage non-autonomously regulates postnatal chondrocyte proliferation and skeletal growth. Development *143*, 1811-1822.

Klinghoffer, R.A., Sachsenmaier, C., Cooper, J.A., and Soriano, P. (1999). Src family kinases are required for integrin but not PDGFR signal transduction. EMBO J *18*, 2459-2471.

Kon, E., Calvo-Jimenez, E., Cossard, A., Na, Y., Cooper, J.A., and Jossin, Y. (2019). N-cadherin-regulated FGFR ubiquitination and degradation control mammalian neocortical projection neuron migration. Elife *8*.

Kouhara, H., Hadari, Y.R., Spivak-Kroizman, T., Schilling, J., Bar-Sagi, D., Lax, I., and Schlessinger, J. (1997). A lipid-anchored Grb2-binding protein that links FGF-receptor activation to the Ras/MAPK signaling pathway. Cell *89*, 693-702.

Kurowski, A., Molotkov, A., and Soriano, P. (2019). FGFR1 regulates trophectoderm development and facilitates blastocyst implantation. Dev Biol *446*, 94-101.

Lanner, F., and Rossant, J. (2010). The role of FGF/Erk signaling in pluripotent cells. Development *137*, 3351-3360.

Larsson, H., Klint, P., Landgren, E., and Claesson-Welsh, L. (1999). Fibroblast growth factor receptor-1-mediated endothelial cell proliferation is dependent on the Src homology (SH) 2/SH3 domain-containing adaptor protein Crk. J Biol Chem *274*, 25726-25734.

Lei, K., and Davis, R.J. (2003). JNK phosphorylation of Bim-related members of the Bcl2 family induces Bax-dependent apoptosis. Proc Natl Acad Sci U S A *100*, 2432-2437.

Lemmon, M.A., and Schlessinger, J. (2010). Cell signaling by receptor tyrosine kinases. Cell *141*, 1117-1134.

Lewis, A.E., Vasudevan, H.N., O'Neill, A.K., Soriano, P., and Bush, J.O. (2013). The widely used Wnt1-Cre transgene causes developmental phenotypes by ectopic activation of Wnt signaling. Dev Biol *379*, 229-234.

Li, P., and Elowitz, M.B. (2019). Communication codes in developmental signaling pathways. Development *146*.

Mailleux, A.A., Overholtzer, M., Schmelzle, T., Bouillet, P., Strasser, A., and Brugge, J.S. (2007). BIM regulates apoptosis during mammary ductal morphogenesis, and its absence reveals alternative cell death mechanisms. Dev Cell *12*, 221-234.

McQuade, K.J., Beauvais, D.M., Burbach, B.J., and Rapraeger, A.C. (2006). Syndecan-1 regulates alphavbeta5 integrin activity in B82L fibroblasts. J Cell Sci *119*, 2445-2456.

Meyer, M., Muller, A.K., Yang, J., Moik, D., Ponzio, G., Ornitz, D.M., Grose, R., and Werner, S. (2012). FGF receptors 1 and 2 are key regulators of keratinocyte migration in vitro and in wounded skin. J Cell Sci *125*, 5690-5701.

Mohammadi, M., Dionne, C.A., Li, W., Li, N., Spivak, T., Honegger, A.M., Jaye, M., and Schlessinger, J. (1992). Point mutation in FGF receptor eliminates phosphatidylinositol hydrolysis without affecting mitogenesis. Nature *358*, 681-684.

Mohammadi, M., Honegger, A.M., Rotin, D., Fischer, R., Bellot, F., Li, W., Dionne, C.A., Jaye, M., Rubinstein, M., and Schlessinger, J. (1991). A tyrosine-phosphorylated carboxy-terminal peptide of the fibroblast growth factor receptor (Flg) is a binding site for the SH2 domain of phospholipase C-gamma 1. Mol Cell Biol *11*, 5068-5078.

Molotkov, A., Mazot, P., Brewer, J.R., Cinalli, R.M., and Soriano, P. (2017). Distinct Requirements for Fgfr1 and Fgfr2 in Primitive Endoderm Development and Exit from Pluripotency. Developmental Cell *41*, 511-526.

Moon, A.M., Guris, D.L., Seo, J.H., Li, L., Hammond, J., Talbot, A., and Imamoto, A. (2006). Crkl deficiency disrupts Fgf8 signaling in a mouse model of 22q11 deletion syndromes. Dev Cell *10*, 71-80.

Moser, M., Legate, K.R., Zent, R., and Fassler, R. (2009). The tail of integrins, talin, and kindlins. Science *324*, 895-899.

Muzumdar, M.D., Tasic, B., Miyamichi, K., Li, L., and Luo, L. (2007). A global double-fluorescent Cre reporter mouse. Genesis *45*, 593-605.

Nakagawa, S., and Takeichi, M. (1995). Neural crest cell-cell adhesion controlled by sequential and subpopulation-specific expression of novel cadherins. Development *121*, 1321-1332.

Nieto, M.A., Huang, R.Y., Jackson, R.A., and Thiery, J.P. (2016). Emt: 2016. Cell *166*, 21-45.

Ong, S.H., Guy, G.R., Hadari, Y.R., Laks, S., Gotoh, N., Schlessinger, J., and Lax, I. (2000). FRS2 proteins recruit intracellular signaling pathways by binding to diverse targets on fibroblast growth factor and nerve growth factor receptors. Mol Cell Biol *20*, 979-989.

Ong, S.H., Hadari, Y.R., Gotoh, N., Guy, G.R., Schlessinger, J., and Lax, I. (2001). Stimulation of phosphatidylinositol 3-kinase by fibroblast growth factor receptors is mediated by coordinated recruitment of multiple docking proteins. P Natl Acad Sci USA *98*, 6074-6079.

Ornitz, D.M., and Itoh, N. (2015). The Fibroblast Growth Factor signaling pathway. Wiley Interdiscip Rev Dev Biol *4*, 215-266.

Park, E.J., Watanabe, Y., Smyth, G., Miyagawa-Tomita, S., Meyers, E., Klingensmith, J., Camenisch, T., Buckingham, M., and Moon, A.M. (2008). An FGF autocrine loop initiated in second heart field mesoderm regulates morphogenesis at the arterial pole of the heart. Development *135*, 3599-3610.

Partanen, J., Schwartz, L., and Rossant, J. (1998). Opposite phenotypes of hypomorphic and Y766 phosphorylation site mutations reveal a function for Fgfr1 in anteroposterior patterning of mouse embryos. Genes Dev *12*, 2332-2344.

Perez, T.D., Tamada, M., Sheetz, M.P., and Nelson, W.J. (2008). Immediate-early signaling induced by E-cadherin engagement and adhesion. J Biol Chem *283*, 5014-5022.

Ran, F.A., Hsu, P.D., Wright, J., Agarwala, V., Scott, D.A., and Zhang, F. (2013). Genome engineering using the CRISPR-Cas9 system. Nat Protoc *8*, 2281-2308.

Rapraeger, A.C., Krufka, A., and Olwin, B.B. (1991). Requirement of heparan sulfate for bFGF-mediated fibroblast growth and myoblast differentiation. Science *252*, 1705-1708.

Rasouli, S.J., El-Brolosy, M., Tsedeke, A.T., Bensimon-Brito, A., Ghanbari, P., Maischein, H.M., Kuenne, C., and Stainier, D.Y. (2018). The flow responsive transcription factor Klf2 is required for myocardial wall integrity by modulating Fgf signaling. Elife *7*.

Raymond, C.S., and Soriano, P. (2007). High-efficiency FLP and PhiC31 site-specific recombination in mammalian cells. PLoS One *2*, e162.
Raymond, C.S., and Soriano, P. (2010). ROSA26Flpo deleter mice promote efficient inversion of conditional gene traps in vivo. Genesis *48*, 603-606.
Reilly, J.F., Mickey, G., and Maher, P.A. (2000). Association of fibroblast growth factor receptor 1 with the adaptor protein Grb14. Characterization of a new receptor binding partner. J Biol Chem *275*, 7771-7778.
Rice, R., Spencer-Dene, B., Connor, E.C., Gritli-Linde, A., McMahon, A.P., Dickson, C., Thesleff, I., and Rice, D.P. (2004). Disruption of Fgf10/Fgfr2b-coordinated epithelial-mesenchymal interactions causes cleft palate. J Clin Invest *113*, 1692-1700.
Sandell, L.L., Kurosaka, H., and Trainor, P.A. (2012). Whole mount nuclear fluorescent imaging: convenient documentation of embryo morphology. Genesis *50*, 844-850.
Scarpa, E., Szabo, A., Bibonne, A., Theveneau, E., Parsons, M., and Mayor, R. (2015). Cadherin Switch during EMT in Neural Crest Cells Leads to Contact Inhibition of Locomotion via Repolarization of Forces. Dev Cell *34*, 421-434.
Schuller, A.C., Ahmed, Z., Levitt, J.A., Suen, K.M., Suhling, K., and Ladbury, J.E. (2008). Indirect recruitment of the signalling adaptor Shc to the fibroblast growth factor receptor 2 (FGFR2). Biochem J *416*, 189-199.
Seo, J.H., Suenaga, A., Hatakeyama, M., Taiji, M., and Imamoto, A. (2009). Structural and functional basis of a role for CRKL in a fibroblast growth factor 8-induced feed-forward loop. Mol Cell Biol *29*, 3076-3087.
Serrano, M., Lee, H., Chin, L., Cordon-Cardo, C., Beach, D., and DePinho, R.A. (1996). Role of the INK4a locus in tumor suppression and cell mortality. Cell *85*, 27-37.
Shigetani, Y., Nobusada, Y., and Kuratani, S. (2000). Ectodermally derived FGF8 defines the maxillomandibular region in the early chick embryo: epithelial-mesenchymal interactions in the specification of the craniofacial ectomesenchyme. Dev Biol *228*, 73-85.
Sims-Lucas, S., Cullen-McEwen, L., Eswarakumar, V.P., Hains, D., Kish, K., Becknell, B., Zhang, J., Bertram, J.F., Wang, F., and Bates, C.M. (2009). Deletion of Frs2alpha from the ureteric epithelium causes renal hypoplasia. Am J Physiol Renal Physiol *297*, F1208-1219.
Sorokin, A., Mohammadi, M., Huang, J., and Schlessinger, J. (1994). Internalization of fibroblast growth factor receptor is inhibited by a point mutation at tyrosine 766. J Biol Chem *269*, 17056-17061.
Steinberg, Z., Myers, C., Heim, V.M., Lathrop, C.A., Rebustini, I.T., Stewart, J.S., Larsen, M., and Hoffman, M.P. (2005). FGFR2b signaling regulates ex vivo submandibular gland epithelial cell proliferation and branching morphogenesis. Development *132*, 1223-1234.
Sun, J., and Stathopoulos, A. (2018). FGF controls epithelial-mesenchymal transitions during gastrulation by regulating cell division and apicobasal polarity. Development *145*.
Sun, X., Meyers, E.N., Lewandoski, M., and Martin, G.R. (1999). Targeted disruption of Fgf8 causes failure of cell migration in the gastrulating mouse embryo. Genes Dev *13*, 1834-1846.
Szabo, A., and Mayor, R. (2018). Mechanisms of Neural Crest Migration. Annu Rev Genet *52*, 43-63.
Tallquist, M.D., and Soriano, P. (2000). Epiblast-restricted Cre expression in MORE mice: a tool to distinguish embryonic vs. extra-embryonic gene function. Genesis *26*, 113-115.

Trumpp, A., Depew, M.J., Rubenstein, J.L., Bishop, J.M., and Martin, G.R. (1999). Cre-mediated gene inactivation demonstrates that FGF8 is required for cell survival and patterning of the first branchial arch. Genes Dev *13*, 3136-3148.

Ueno, H., Gunn, M., Dell, K., Tseng, A., Jr., and Williams, L. (1992). A truncated form of fibroblast growth factor receptor 1 inhibits signal transduction by multiple types of fibroblast growth factor receptor. J Biol Chem *267*, 1470-1476.

Vasioukhin, V., Bauer, C., Yin, M., and Fuchs, E. (2000). Directed actin polymerization is the driving force for epithelial cell-cell adhesion. Cell *100*, 209-219.

Vasudevan, H.N., Mazot, P., He, F., and Soriano, P. (2015). Receptor tyrosine kinases modulate distinct transcriptional programs by differential usage of intracellular pathways. Elife *4*.

Wang, C., Chang, J.Y., Yang, C., Huang, Y., Liu, J., You, P., McKeehan, W.L., Wang, F., and Li, X. (2013). Type 1 fibroblast growth factor receptor in cranial neural crest cell-derived mesenchyme is required for palatogenesis. J Biol Chem *288*, 22174-22183.

Wheelock, M.J., and Johnson, K.R. (2003). Cadherins as modulators of cellular phenotype. Annu Rev Cell Dev Biol *19*, 207-235.

Xu, H., Lee, K.W., and Goldfarb, M. (1998a). Novel recognition motif on fibroblast growth factor receptor mediates direct association and activation of SNT adapter proteins. J Biol Chem *273*, 17987-17990.

Xu, X., Weinstein, M., Li, C., Naski, M., Cohen, R.I., Ornitz, D.M., Leder, P., and Deng, C. (1998b). Fibroblast growth factor receptor 2 (FGFR2)-mediated reciprocal regulation loop between FGF8 and FGF10 is essential for limb induction. Development *125*, 753-765.

Yamaguchi, T.P., Harpal, K., Henkemeyer, M., and Rossant, J. (1994). fgfr-1 is required for embryonic growth and mesodermal patterning during mouse gastrulation. Genes Dev *8*, 3032-3044.

Yayon, A., Klagsbrun, M., Esko, J.D., Leder, P., and Ornitz, D.M. (1991). Cell surface, heparin-like molecules are required for binding of basic fibroblast growth factor to its high affinity receptor. Cell *64*, 841-848.

Youle, R.J., and Strasser, A. (2008). The BCL-2 protein family: opposing activities that mediate cell death. Nat Rev Mol Cell Biol *9*, 47-59.

Yu, K., Xu, J., Liu, Z., Sosic, D., Shao, J., Olson, E.N., Towler, D.A., and Ornitz, D.M. (2003). Conditional inactivation of FGF receptor 2 reveals an essential role for FGF signaling in the regulation of osteoblast function and bone growth. Development *130*, 3063-3074.

Zinkle, A., and Mohammadi, M. (2018). A threshold model for receptor tyrosine kinase signaling specificity and cell fate determination. F1000Res *7*.

Figure 1

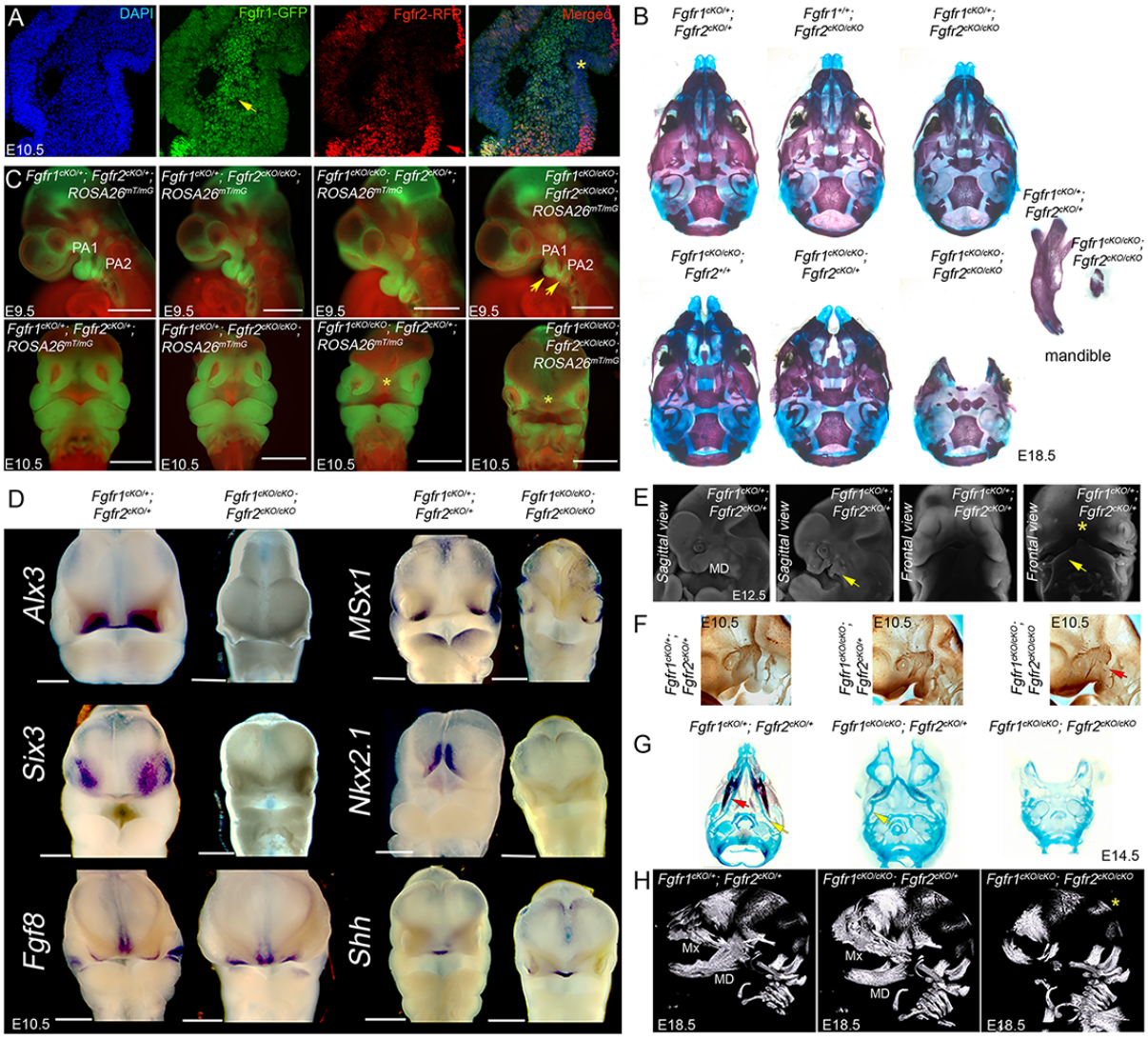

Figure 2

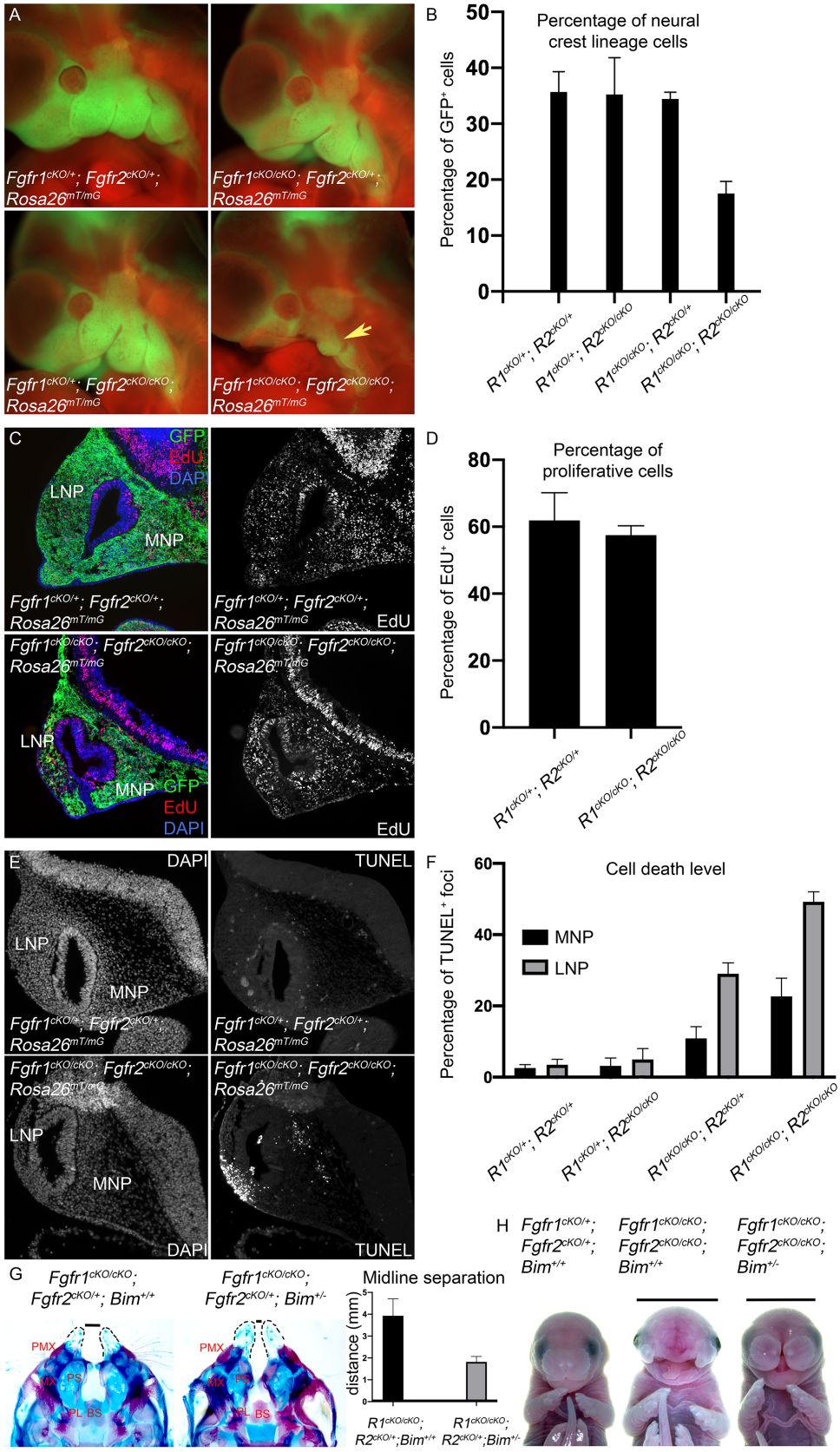

Figure 3

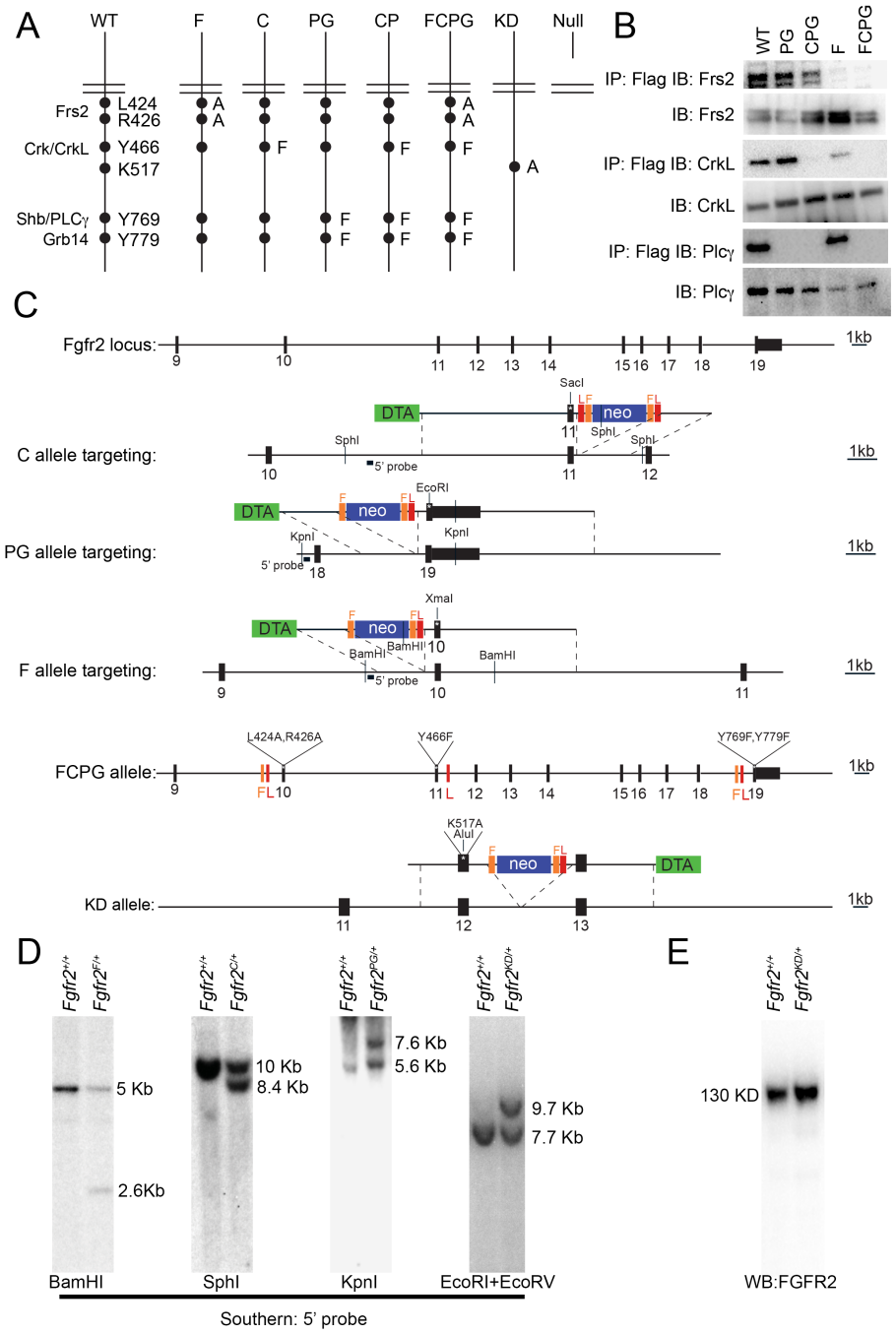

Figure 4

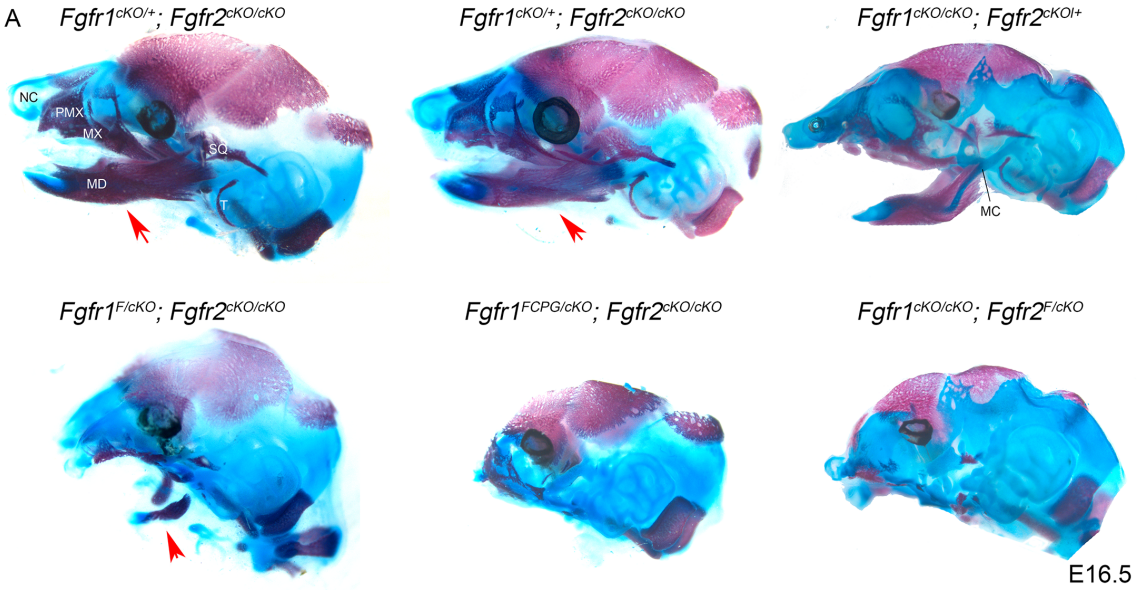

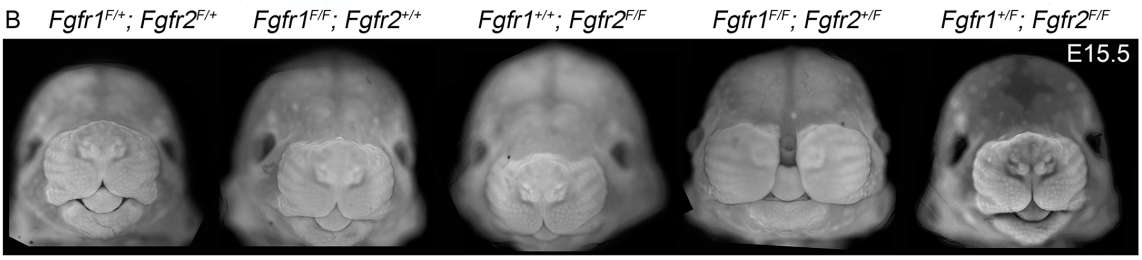

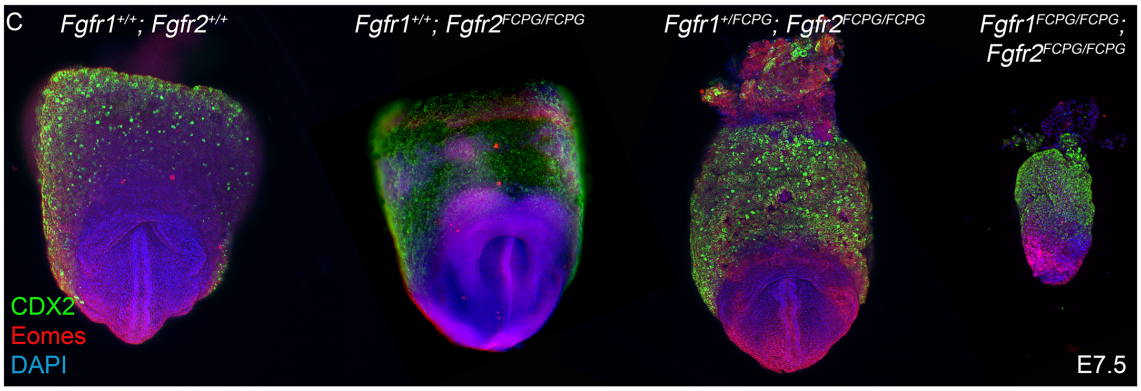

Figure 5

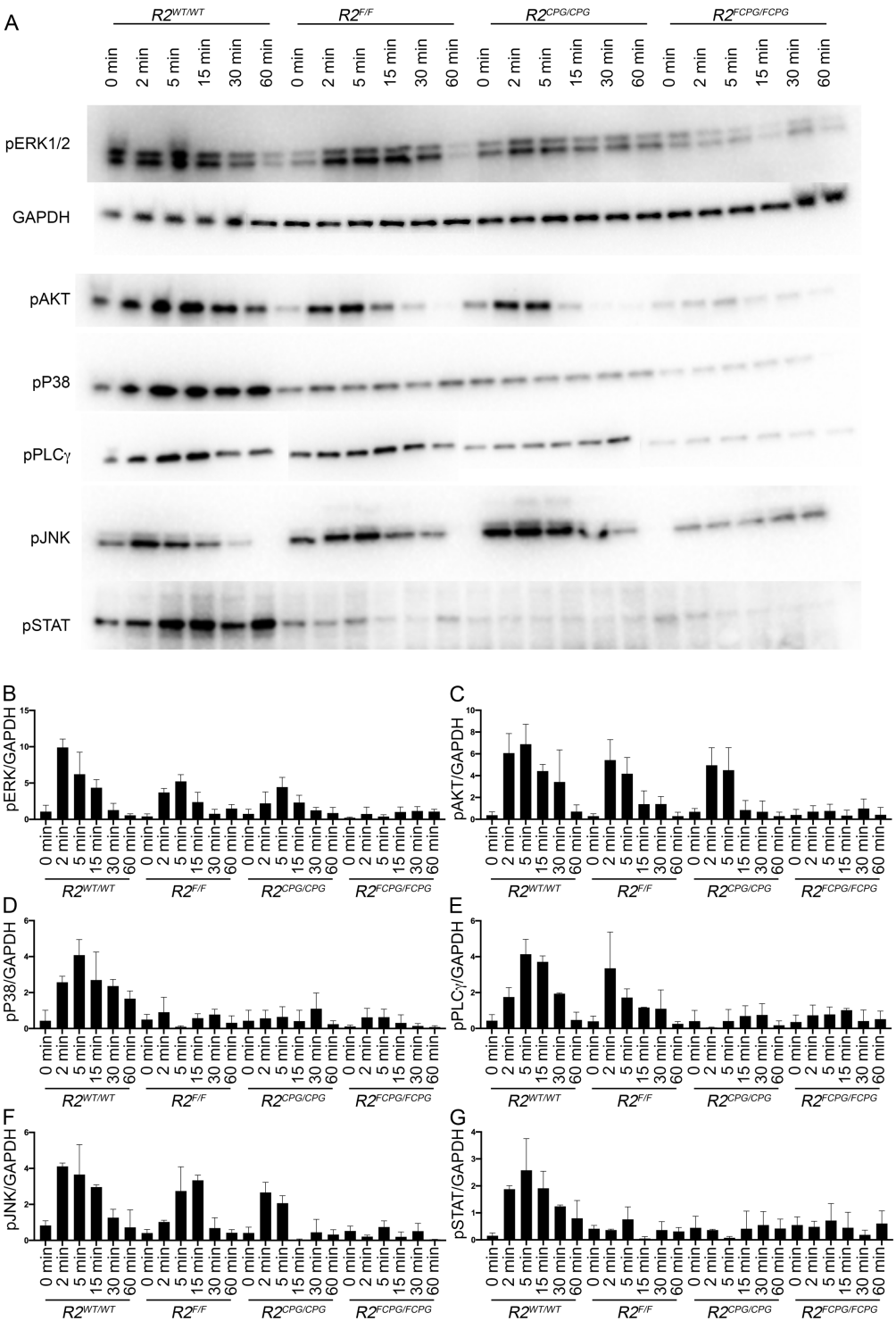

Figure 6

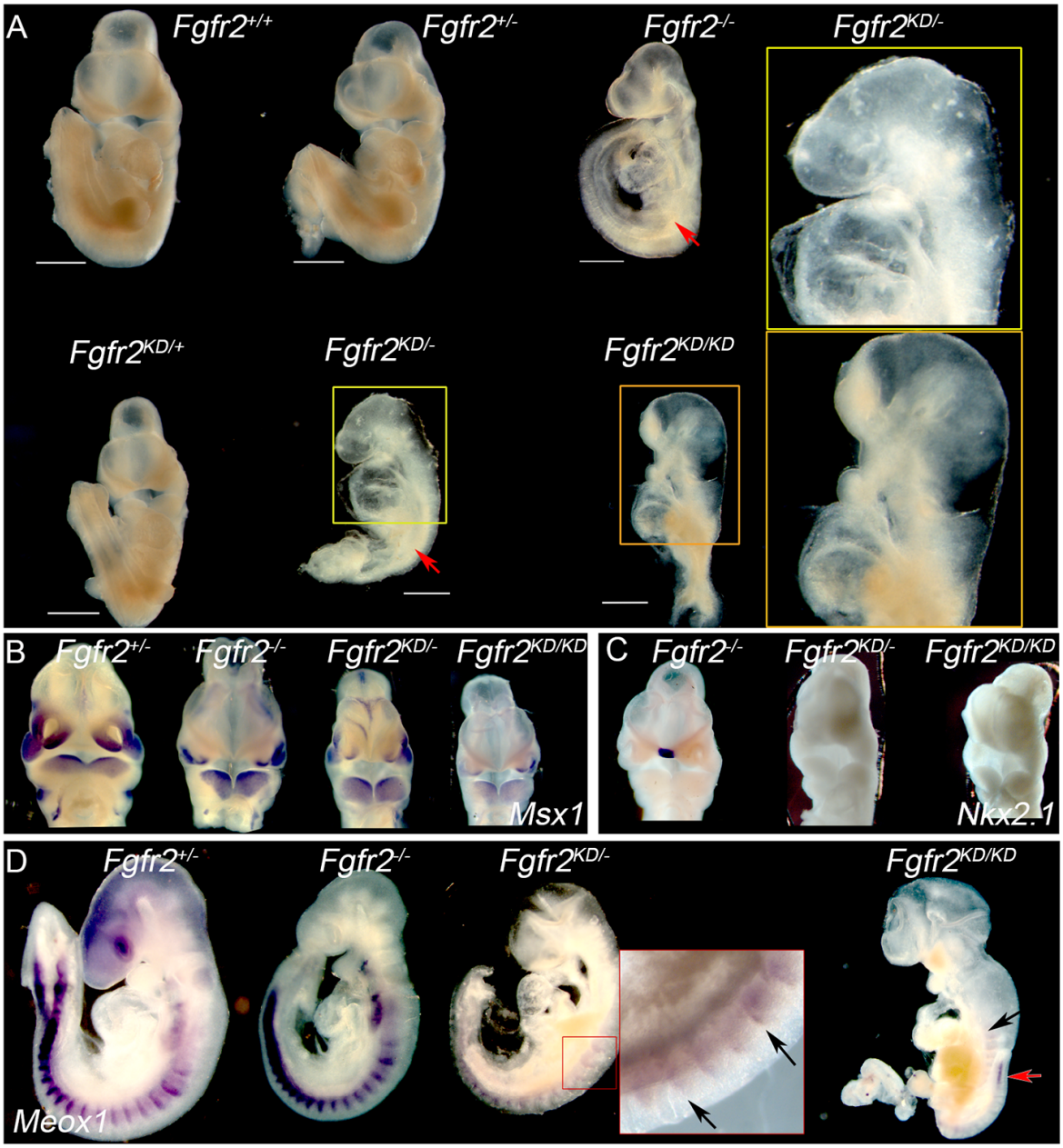

Figure 7

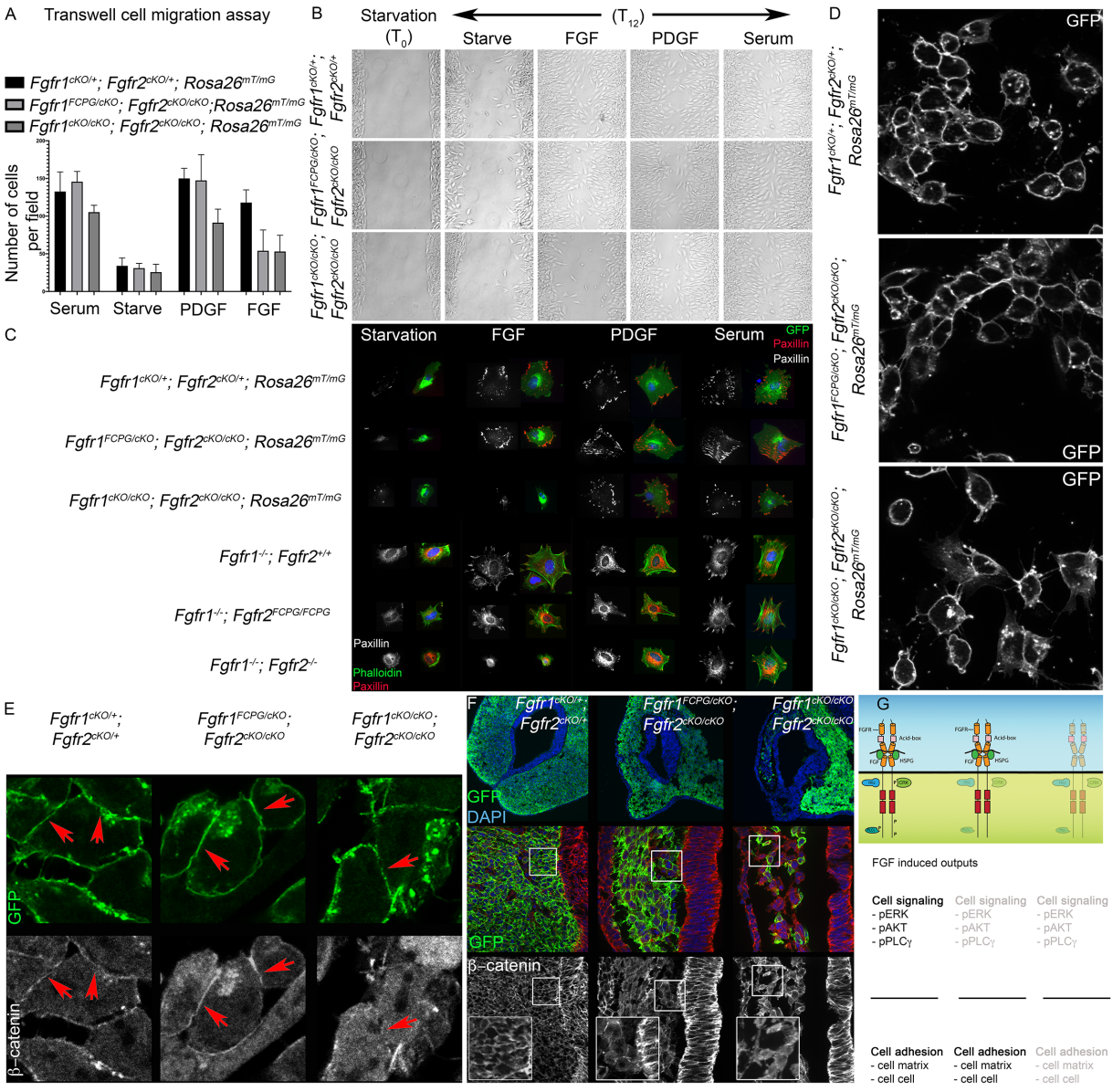

Supplementary Figure S1

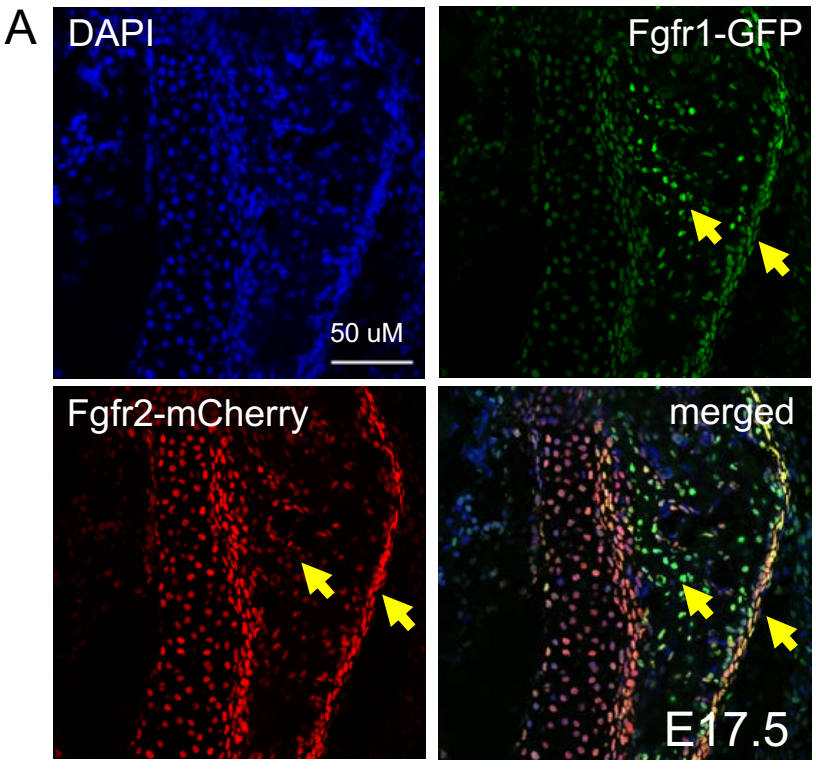

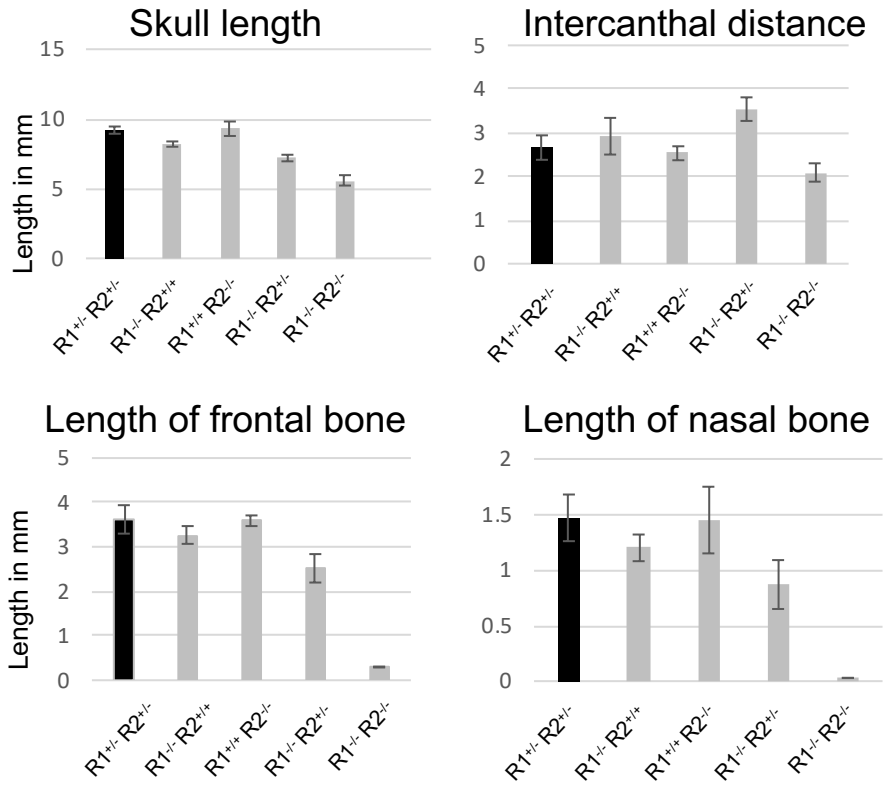

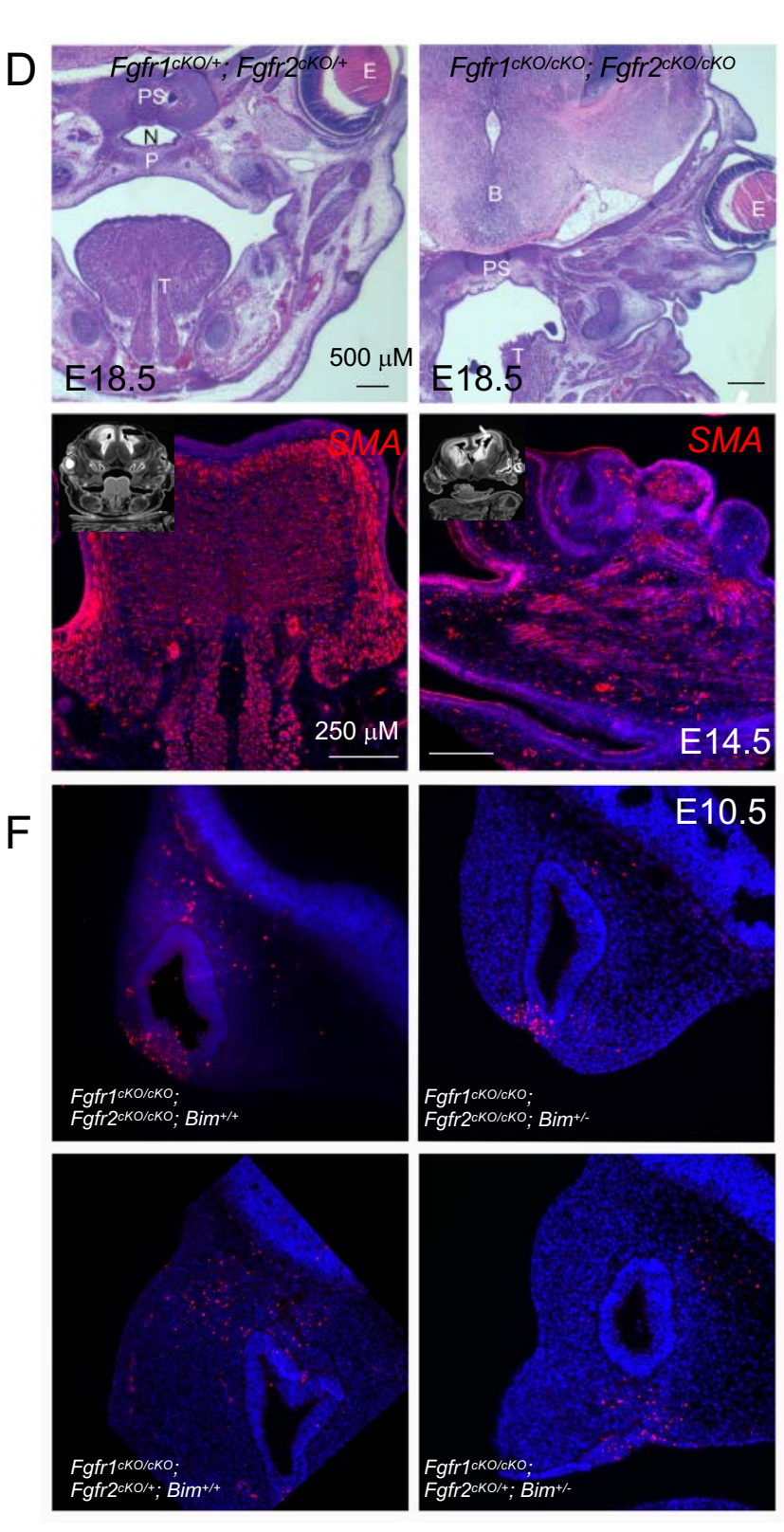

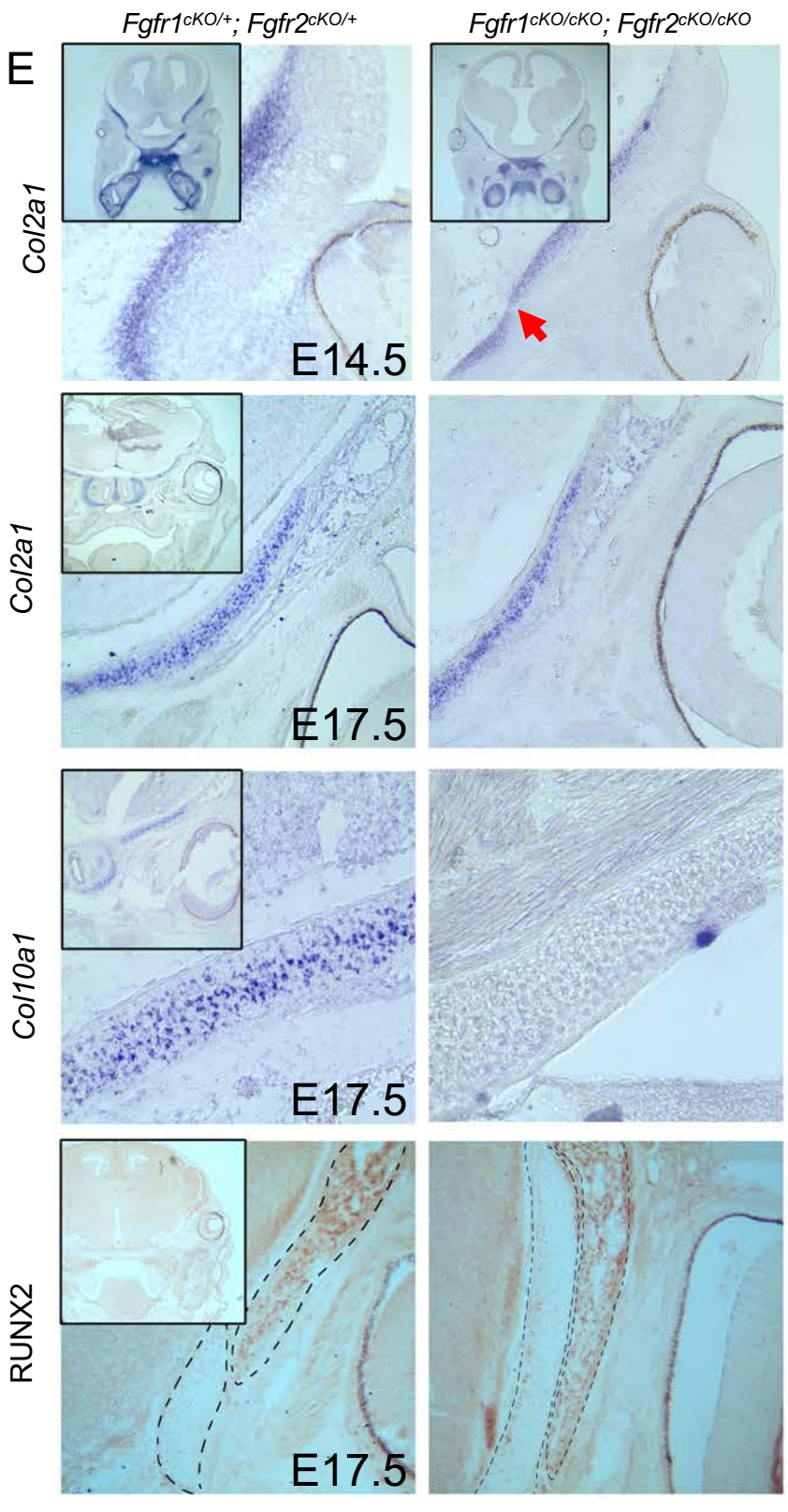

Supplementary Figure S2

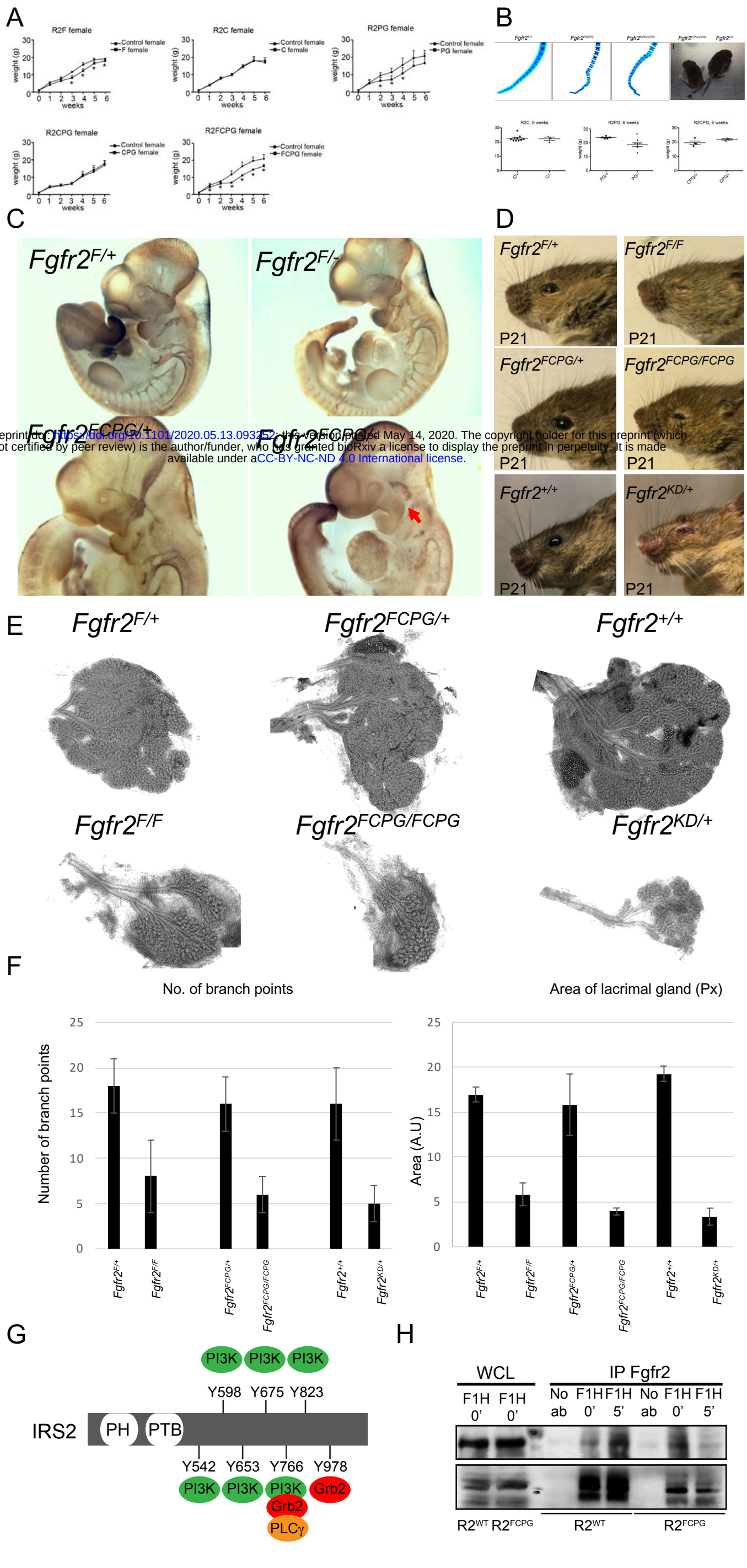

Supplementary Figure S3

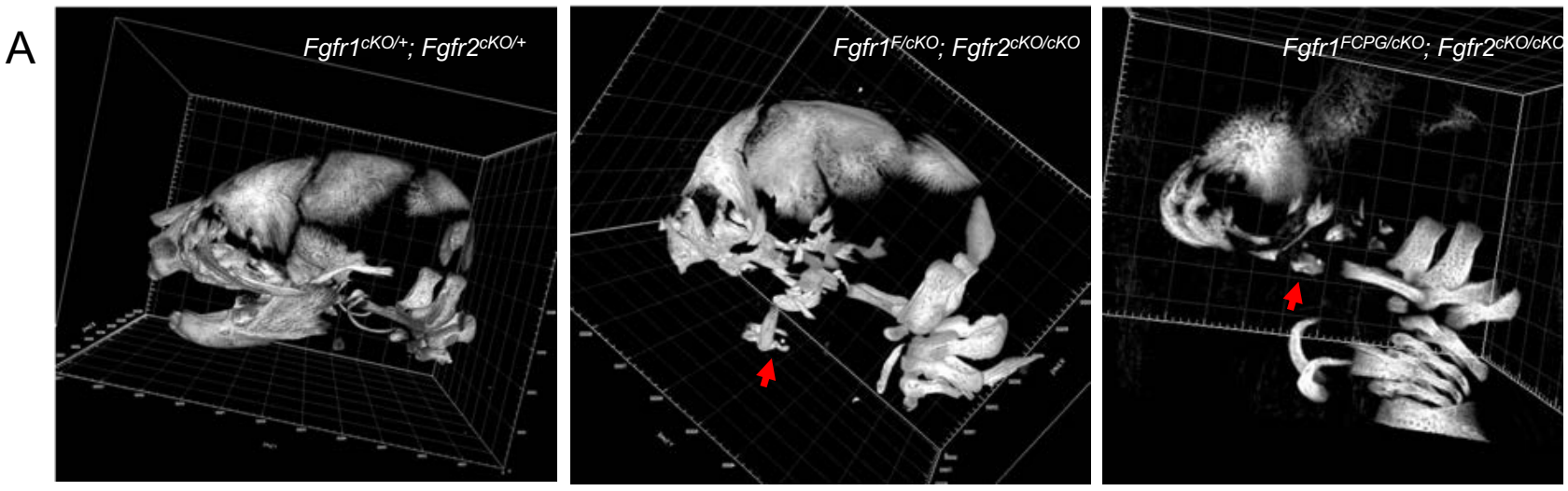

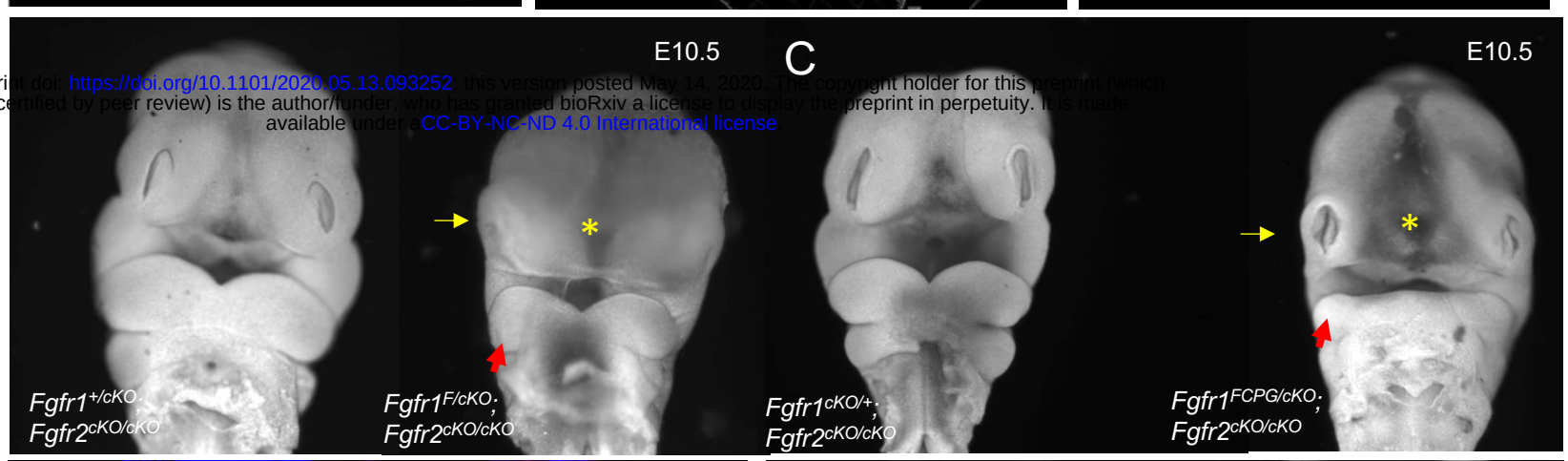

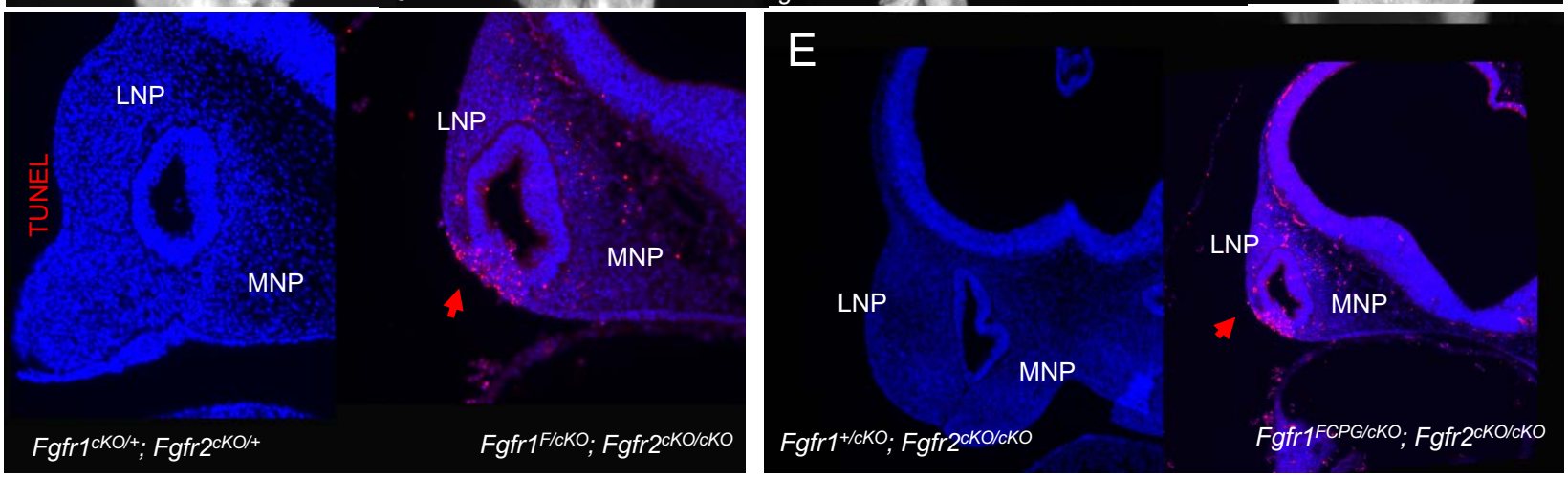

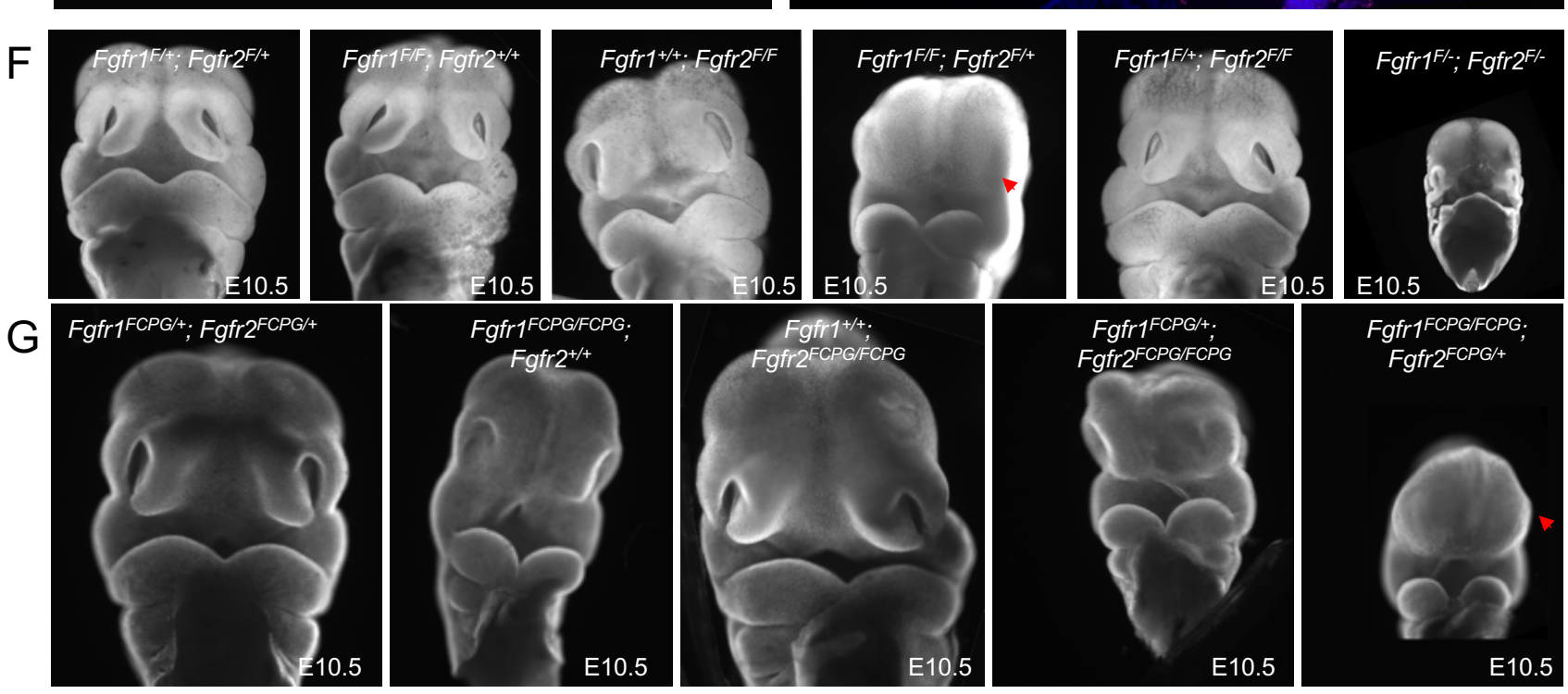

Supplementary Figure S4

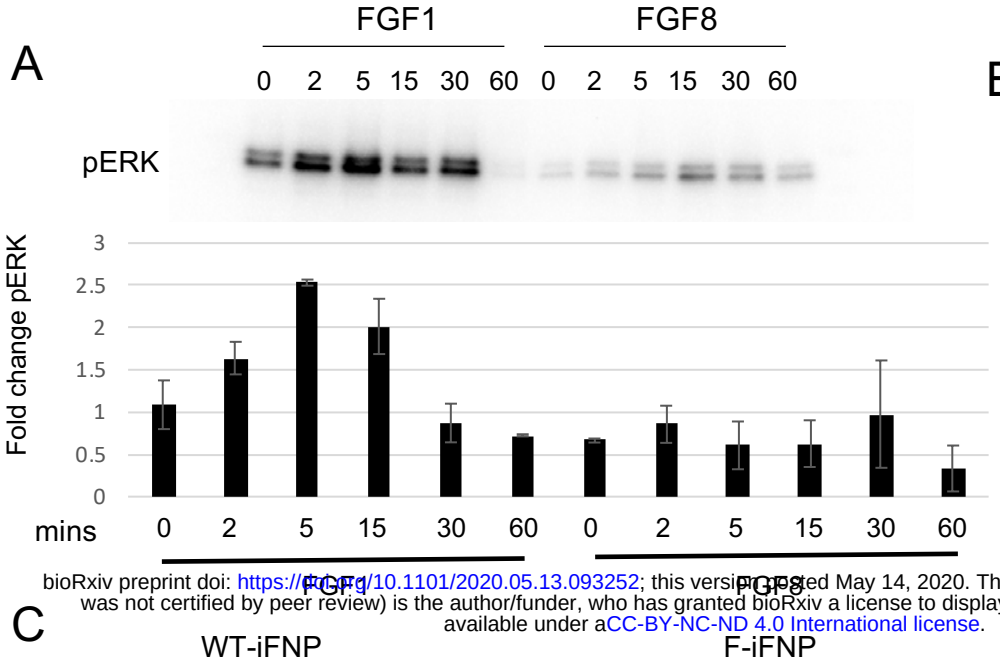

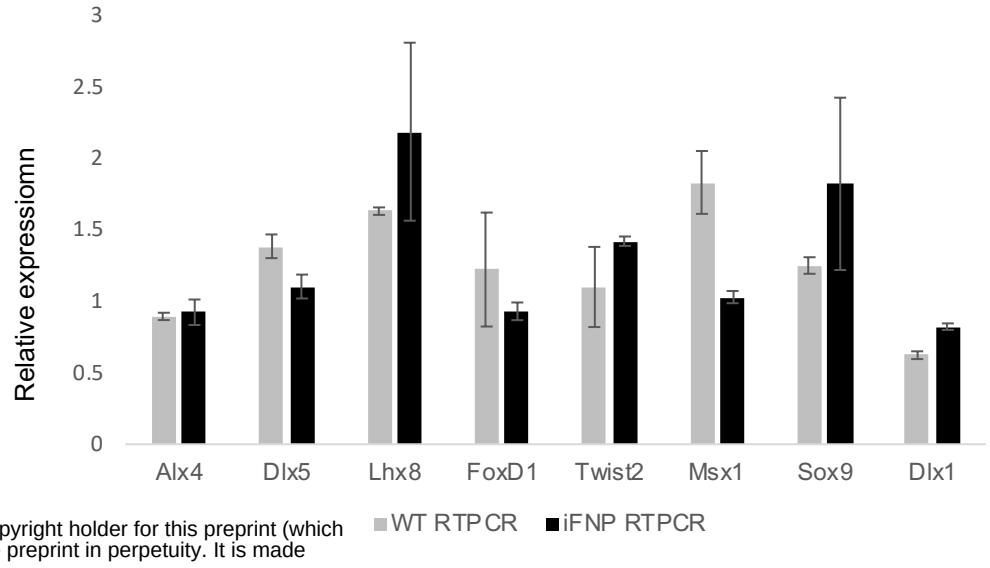

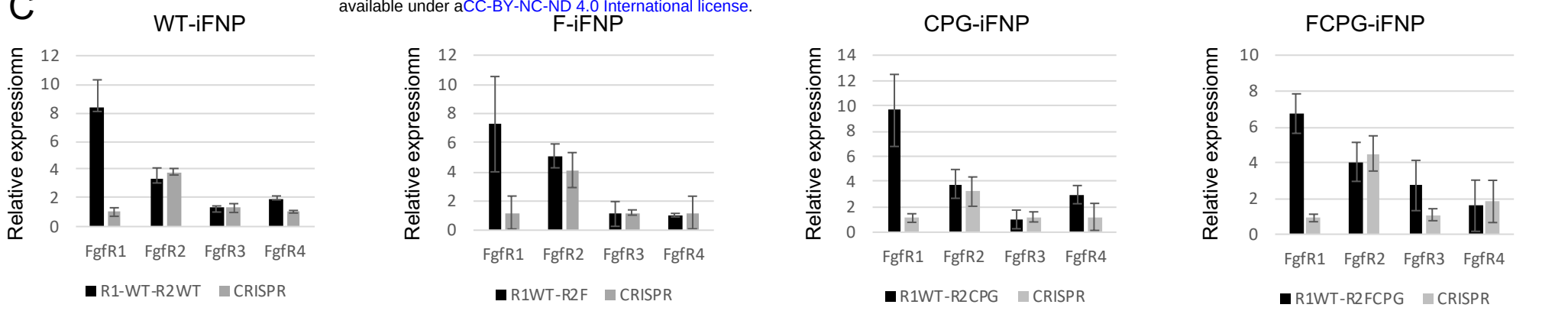

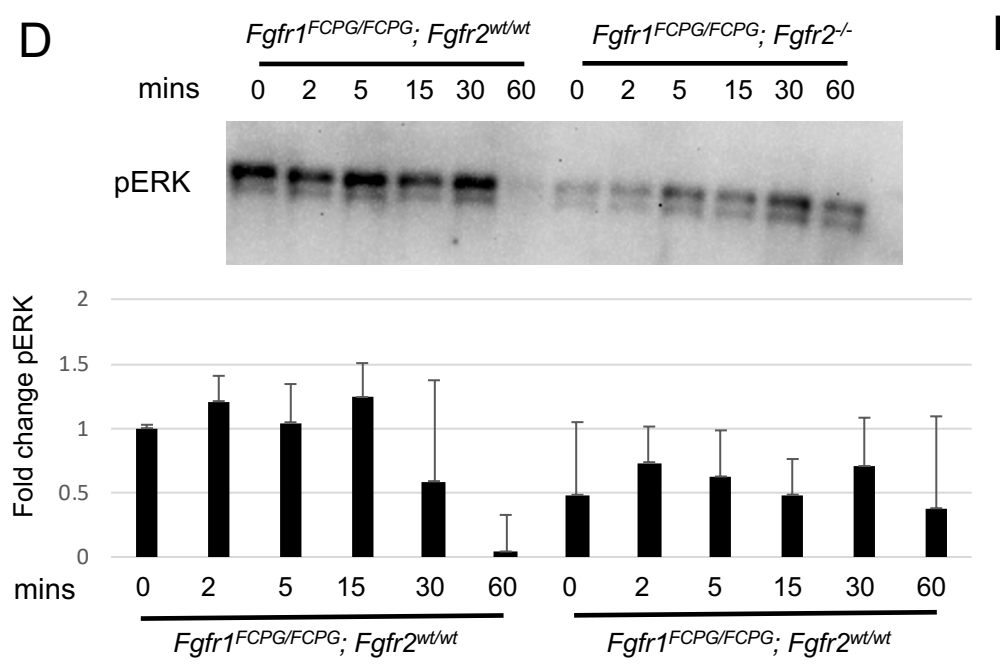

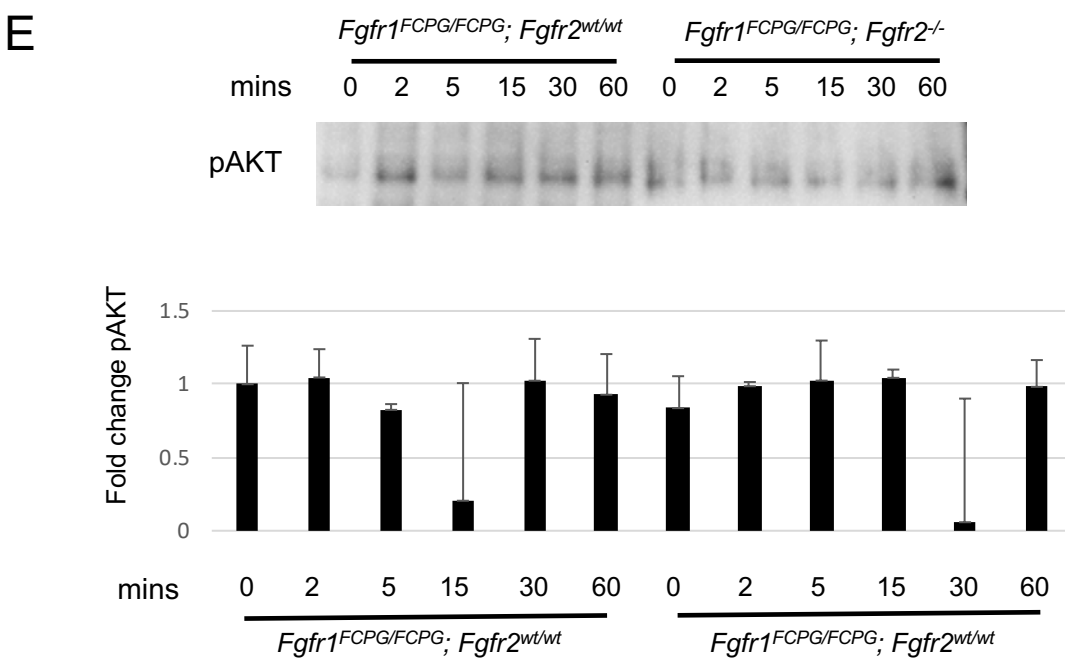

Supplementary Figure S5